

Design of Effective Traveling Wave Sloshing Absorbers for Structural Control

Adam Patrick Marsh

A thesis submitted to Victoria University
for the Doctor of Philosophy Degree (Mechanical Engineering)

2009

ACKNOWLEDGEMENTS

I would like to thank the supervisors of this thesis, Dr. Eren Semercigil, Dr. Özden Turan and Dr. Mahesh Prakash. I thank them for their professional and personal advice, friendship and encouragement.

During my candidature I was a recipient of a Faculty of Engineering and Science Postgraduate Research Scholarship from Victoria University, along with a top-up Research Scholarship from CSIRO. The financial support from these of two scholarships was greatly appreciated.

The experimental setup used in Chapters 2 and 4 has the same design as the one Professor Neil Popplewell had in the Dynamics and Vibrations Laboratory of the Mechanical Engineering Department at the University of Manitoba in Winnipeg, Manitoba, Canada. Following the 1999 sabbatical leave of the first two thesis supervisors with Professor Popplewell, it had been hoped that he would be a co-supervisor of my thesis project and the one prior to mine. I still hope to have an opportunity to discuss my work with him, having heard so much about him and his laboratory.

To the postgraduate students I shared an office with, it was a great pleasure working with you all. Finally, to my family and friends, I sincerely thank you all for your support.

Adam Patrick Marsh

ABSTRACT

A liquid sloshing absorber is a container partially filled with liquid. The primary objective of this thesis is to contribute to the understanding of rigid liquid sloshing absorbers with shallow depths, in structural control applications. An effective means of using intentionally induced liquid sloshing to control low frequency, transient structural oscillations is presented, establishing the sloshing absorber as an effective structural control mechanism.

Smoothed Particle Hydrodynamics (SPH) is used as a numerical modeling tool to predict fluid behaviour within the sloshing absorber, and the fluid-structure interaction forces produced when coupled to a structure. Close correspondence is seen between SPH predictions and experimental observations, identifying the method as a valuable tool for sloshing absorber design.

SPH is used for the design optimisation of the conventionally used rectangular geometry based on energy dissipation performance. Appropriate selection of water depth and container width is found to optimise energy dissipation within this shape. Further improvement in control performance is achieved by modifying the shape of the rectangular sloshing absorber. Superior energy transfer and dissipation characteristics are produced. The novel concept of using the geometry of a hen's egg as a sloshing absorber is then introduced. When uncooked, the hen's egg possesses the properties of high mechanical damping. The possible employment of the hen's egg as a sloshing absorber is investigated. Great potential is seen in this naturally occurring geometry.

TABLE OF CONTENTS

	Page
ACKNOWLEDGEMENTS	ii
ABSTRACT	iii
LIST OF TABLES	vi
LIST OF FIGURE CAPTIONS	vii
Chapter 1	1
INTRODUCTION	
Chapter 2	7
EXPERIMENTAL OBSERVATIONS AND NUMERICAL PREDICTIONS OF A SHALLOW DEPTH SLOSHING ABSORBER FOR STRUCTURAL CONTROL	
2.1 INTRODUCTION	7
2.2 EXPERIMENTAL PROCEDURE	9
2.3 NUMERICAL PROCEDURE	11
2.4 EXPERIMENTAL OBSERVATIONS	12
2.5 NUMERICAL PREDICTIONS	15
2.5.1 Liquid depth of 5.5 mm	15
2.5.2 Liquid depth of 22 mm	18
2.6 CONCLUSIONS	21
Chapter 3	31
A NUMERICAL INVESTIGATION OF ENERGY DISSIPATION WITH A SHALLOW DEPTH SLOSHING ABSORBER	
3.1 INTRODUCTION	31
3.2 NUMERICAL MODEL AND PROCEDURE	33
3.3 OBSERVATIONS	34
3.3.1 Kinetic energy dissipation	35
3.3.2 Probability density	37
3.3.3 Settling times	38
3.3.4 Kinetic energy transfer from the base	39
3.3.5 Flow visualisation	40
3.3.6 Tuning	44
3.4 CONCLUSION	46
Chapter 4	61
PREDICTING THE DYNAMIC STRUCTURAL RESPONSE CONTROLLED BY A SLOSHING ABSORBER USING SPH	
4.1 INTRODUCTION	61
4.2 EXPERIMENTAL PROCEDURE	62
4.3 NUMERICAL MODEL	64
4.4 LIQUID SLOSHING AND STRUCTURAL RESPONSE	65
4.4.1 Displacement History	65
4.4.2 Settling Times	67
4.4.3 Free Surface Comparison	68
4.4.4 Correcting ζ_{eq}	71
4.4.5 Summary results for computational smoothing length	74
4.4.6 Flow visualisation results for computational smoothing length	75
4.5 CONCLUSIONS	77

	Page
Chapter 5	90
A STUDY OF SLOSHING ABSORBER GEOMETRY FOR STRUCTURAL CONTROL WITH SPH	
5.1 INTRODUCTION	90
5.2 NUMERICAL MODEL	91
5.3 RECTANGULAR GEOMETRY	92
5.4 EFFECT OF CONTAINER SHAPE	97
5.5 TUNING TRAPEZOIDAL CONTAINERS	100
5.6 EFFECT OF VARYING EXCITATION MAGNITUDE	102
5.7 CONCLUSIONS	103
Chapter 6	119
A STUDY OF THE DYNAMICS OF A NATURAL SLOSHING ABSORBER : THE HEN'S EGG	
6.1 INTRODUCTION	119
6.2 NUMERICAL MODEL AND PROCEDURE	121
6.3 SPH PREDICTIONS	123
6.3.1 Natural egg	123
6.3.2 A structural modification of the egg	125
6.3.3 Geometric scaling	126
6.4 EXPERIMENTS	127
6.5 CONCLUSIONS	129
Chapter 7	139
CONCLUSION	
REFERENCES	143
Appendix 1	150
SMOOTHED PARTICLE HYDRODYNAMICS	
APPENDIX 2	159
RESOLUTION STUDY	
APPENDIX 3	165
KINEMATIC FREE SURFACE COMPARISONS	
APPENDIX 4	168
KINETIC ENERGY DISSIPATION HISTORIES	
APPENDIX 5	171
DYNAMIC FREE SURFACE COMPARISONS	
APPENDIX 6	176
OSCILLATORY HISTORIES OF MODIFIED EGG PROFILE	

LIST OF TABLES

Table 2.1. Experimental set-up parameters. Mass and length are reported with an estimated accuracy of 0.010 kg and 0.001m, respectively.

Table 2.2. Rotary inertia and mass ratios of fluid to those of the structure for different liquid depths.

LIST OF FIGURE CAPTIONS

- Figure 1.1. Tuned liquid damper, attached to a mechanical oscillator of mass m , stiffness k and viscous damping coefficient of c .
- Figure 2.1. Sloshing absorber, attached to a mechanical oscillator of mass m , stiffness k and viscous damping coefficient of c . Repeated from Figure 1.1 for easy reference.
- Figure 2.2. (a) Showing the structure and the tuned absorber. Dimensions are in millimetres (mm).
(b) Photo of experimental setup.
- Figure 2.3. Angular oscillation histories of (a) uncontrolled, (b) 2.75 mm, (c) 5.5 mm, (d) 8.25 mm, (e) 11 mm and (f) 22 mm deep cases.
- Figure 2.4. Variation of settling time with different water depths.
- Figure 2.5. Free surface comparisons of 5.5 mm liquid depth; left column has the experimental observations, right column has the numerical predictions.
- Figure 2.6. Same as in Figure 5, but for 22 mm liquid depth.
- Figure 3.1. Showing (a) numerical model and (b) history of base excitation.

Figure 3.2. Comparison of kinetic energy histories, for 20 mm depth in a 400 mm wide container. Particle size of 0.5 mm x 0.5 mm (—) and 0.8 mm x 0.8 mm (—).

Figure 3.3. Kinetic energy dissipation histories for different water depths of (a) 5 mm, (b) 10 mm, (c) 15mm, (d) 20 mm, (e) 40 mm, (f) 60 mm, (g) 80 mm and (h) 100 mm. Constant container width of 400 mm. Note y-axes values vary significantly.

Figure 3.4. Probability densities of kinetic energy shown in Figure 3.3.

Figure 3.5. A summary of settling times for different water depths with a constant container width of 200 mm. The legend is for the level of residual energy as a percentage of the maximum.

Figure 3.6. A summary of settling times for different water depths. Constant container width of 400 mm. The legend is for the level of residual energy as a percentage of the maximum.

Figure 3.7. A summary of settling times for different water depths. Constant container width of 600 mm. The legend is for the level of residual energy as a percentage of the maximum.

Figure 3.8. Maximum energy transferred from base excitation to the working fluid per unit mass of fluid for container widths of 200 mm (\diamond), 400 mm (\square) and 600 mm (Δ), implementing liquid depths of 5 mm, 10 mm, 15 mm, 20 mm, 40 mm, 60 mm, 80 mm and 100 mm.

Figure 3.9. Still frames at instants of interest for 20 mm liquid depth and 400 mm wide container. The fixed velocity scale is from 0 to 1.1 metres per second.

Figure 3.10. Still frames at instants of interest for 100 mm liquid depth and 400 mm wide container. The fixed velocity scale is from 0 to 2.1 metres per second.

Figure 3.11. Kinetic energy dissipation histories for different container widths of (a) 25 mm, (b) 50 mm, (c) 75 mm, (d) 100 mm, (e) 125 mm, (f) 150 mm, (g) 200 mm and (h) 400 mm. Constant water depth of 20 mm. The amplitude values of the y-axis vary significantly.

Figure 3.12. Probability densities of the kinetic energy shown in Figure 3.11.

Figure 3.13. A summary of settling times for different container widths with a constant liquid depth of 20 mm. Legend indicates the level of residual energy as a percentage of the maximum.

- Figure 3.14. Maximum kinetic energy transferred for different container widths. Constant water depth of 20 mm.
- Figure 4.1. Showing the structure and the sloshing absorber at rest (vertical) and at initially displaced positions.
- Figure 4.2. History of angular displacement of experimental observations (•) and SPH predictions (—) for (a) uncontrolled, (b) 2.75 mm, (c) 5.5 mm, (d) 8.25 mm, (e) 11 mm and (f) 22 mm deep cases. Lennard Jones boundary treatment. Smoothing length (h) of 1.2.
- Figure 4.3. (a) Variation of experimentally observed settling time with liquid depths and residual displacement comparisons for (b) 2.75 mm, (c) 5.5 mm, (d) 8.25 mm, (e) 11 mm and (f) 22 mm liquid depths between experiments (—) and predictions (---).
- Figure 4.4. Free surface comparisons of 2.75 mm liquid depth at different marked instances. The left column has the experimental observations, and the right column has the numerical predictions.
- Figure 4.5. Same as in Figure 3, but for a gradient of kernel boundary approximation. (a) uncontrolled, (b) 2.75 mm, (c) 5.5 mm, (d) 8.25 mm, (e) 11 mm and (f) 22 mm deep cases. Smoothing length of 1.2.

- Figure 4.6. History of angular displacement of experimental observations (•) and SPH predictions (—) for 8.25 mm depth. Smoothing lengths of (a) 1.2, (b) 2.4, (c) 3.6 and (d) 4.8.
- Figure 4.7. Same as in Figure 4.6, but for 11 mm depth.
- Figure 4.8. Same as in Figure 4.7, but for 22 mm depth.
- Figure 4.9. Free surface comparison between the experimental snapshot in (a), and SPH predictions obtained using a Lennard-Jones boundary treatment with a smoothing length of 1.2 in (b), and a gradient of kernel approximation with smoothing lengths of (c) 1.2, (d) 2.4, (e) 3.6 and (f) 4.8.
- Figure 4.10. Same as in Figure 4.9, but for 11 mm depth.
- Figure 4.11. Same as in Figure 4.10, but for 22 mm depth.
- Figure 5.1. Tuned rectangular liquid damper coupled to a single degree of freedom structure. Repeat of Figure 1.1 for easy reference.
- Figure 5.2. (a) Structural displacement history (---) uncontrolled and (—) controlled with a tuned rectangular liquid sloshing absorber. (b) First 10 seconds of the controlled structural displacement (---) and the corresponding fluid power (—).

Figure 5.3. Still frames at instants of interest within the tuned rectangular absorber. Colour scale in the left column represents fluid velocity (m/s); whereas the scale in the right column represents rate of shear energy dissipation (W).

Figure 5.4. Series of shapes investigated. h is the liquid depth used, f_1 is the free surface length. The same fluid volume was used in all shapes to keep added fluid mass constant at 10%.

Figure 5.5. Structural displacement histories corresponding to shapes in Figure 5.4.

Figure 5.6. First 10 seconds of displacement (---) and fluid power (—) histories of the (a) tuned rectangular absorber, (b) cylindrical absorber, (c) trapezoidal damper with converging walls at an angle of 30 degrees and 0.2 m free surface and (d) trapezoidal damper with diverging walls at an angle of 30 degrees and 0.2 m free surface.

Figure 5.7. Displacement histories with a trapezoidal absorber of 30 degree diverging walls and free surface length of (a) 160 mm, (b) 180 mm, (c) 200 mm, (d) 220 mm and (e) 240 mm.

Figure 5.8. Displacement histories with a trapezoidal absorber of 30 degree converging walls and free surface length of (a) 160 mm, (b) 180 mm, (c) 200 mm, (d) 220 mm and (e) 240 mm.

- Figure 5.9. Variation of the settling time with free surface length for 30 degree converging walls. Residual levels of structural displacement as a percentage of the maximum are indicated as 1% (T), 2% (\circ), 5% (\square), 10% (\square) and 25% (+).
- Figure 5.10. First 10 seconds of displacement and fluid power histories of the trapezoidal damper with converging walls at an angle of 30 degrees and 0.22 m free surface length.
- Figure 5.11. Still frames at instances of interest within the tuned rectangular absorber in the left hand column and the tuned converging trapezoid in the right hand column. Fixed colour scale represents fluid velocity (m/s).
- Figure 5.12. Effect of varying the excitation magnitude on the tuned rectangular absorber (left column) and the tuned converging trapezoid (right column). Initial velocity magnitudes of (a) and (b) 0.25 m/s, (c) and (d) 0.5 m/s and (e) and (f) 1.0 m/s. Y-axis scale changes down the page.
- Figure 6.1. Angular displacement history of an egg after release when raw (—) and boiled (---). Results from So and Semercigil, 2004.
- Figure 6.2. Schematic of hen's egg physiology, from Avian Sciences Net, 2009.

- Figure 6.3. Schematic of the egg geometry from The Magic Egg, 2009. For an aspect ratio of 1.3, $r_1 = 44.5$ mm, $r_2 = 26$ mm and $r_3 = 89$ mm.
- Figure 6.4. SPH prediction of the egg-shaped cylinder's motion when filled with water to volume fractions of (a) 0.2, (b) 0.4, (c) 0.6, (d) 0.8 and (e) 1.0. 1:1 scale to the hen's egg.
- Figure 6.5. Snapshots of SPH predictions of instants of interest within the egg-shaped cylinder. (a) to (d) for volume fraction of 0.2 and (e) to (f) for volume fraction of 1.0. 1:1 scale to the hen's egg.
- Figure 6.6. Showing (a) schematic of the fin geometries with the natural egg (1), and fin height fractions of 0.2 (2), 0.4 (3) and 0.6 (4); and (b) variation of settling time with volume fraction. Natural egg (\diamond), and fin height fraction of 0.2 (\square), 0.4 (Δ) and 0.6 (\times).
- Figure 6.7. Oscillation histories for scales of 1:1 ($\cdots\Delta\cdots$), 2:1 (---) and 3:1 ($\cdots\text{---}$) to that of the hen's egg. Angular displacement is normalised with initial displacement (θ_{max}), and time is normalised with natural period (t_p).
- Figure 6.8. Graphical representation of (a) initial and (b) final rest positions.
- Figure 6.9. Displacement histories of experiments (o) and SPH predictions (---) of the 2:1 scale egg cylinder. Experimental data is accurate to within ± 0.04 s and ± 1 degree.

Figure 6.10. Showing (a) the schematic of the fin height ratio of 0.2, and displacement histories with a volume fraction of (b) 0.2, (c) 0.4, (d) 0.6, (e) 0.8 and (f) 1.0.

Figure 6.11. Same as in Figure 6.10, but with a fin height of 0.4.

Figure 6.12. Same as in Figure 6.10, but with a fin height of 0.6.

Figure A2.1. Free surface comparisons between experimental observations, and numerical predictions obtained with particle sizes of 0.0625 mm², 0.25 mm² and 1.00 mm². Particle size is marked at bottom right corner of frames. Fixed colour scale represents fluid velocity in m/s.

Figure A3.1. Kinematic free surface comparison for 8.25 mm depth.

Figure A3.2. Kinematic free surface comparison for 11 mm depth.

Figure A4.1 Kinetic energy dissipation histories for different water depths of (a) 5 mm, (b) 10 mm, (c) 15 mm, (d) 20 mm, (e) 40 mm, (f) 60 mm, (g) 80 mm and (h) 100 mm. Constant container width of 200 mm. The y-axis amplitude values vary significantly.

Figure A4.2 Kinetic energy dissipation histories for different water depths of (a) 5 mm, (b) 10 mm, (c) 15 mm, (d) 20 mm, (e) 40 mm, (f) 60 mm, (g) 80 mm and (h) 100 mm. Constant container width of 600 mm. The y-axis amplitude values vary significantly.

Figure A5.1. Dynamic free surface comparison for 5.5 mm liquid depth.

Figure A5.2. Dynamic free surface comparison for 8.25 mm liquid depth.

Figure A5.3. Dynamic free surface comparison for 11 mm liquid depth.

Figure A5.4. Dynamic free surface comparison for 22 mm liquid depth.

Figure A6.1. Showing (a) the schematic of the fin height ratio of 0.2, and displacement histories with a volume fraction of (b) 0.2, (c) 0.4, (d) 0.6, (e) 0.8 and (f) 1.0.

Figure A6.2. Same as in Figure A6.1., but with a fin height ratio of 0.4.

Figure A6.3. Same as in Figure A6.1., but with a fin height ratio of 0.6.

Chapter 1

INTRODUCTION

In this thesis, passive structural control is investigated with a sloshing absorber to enhance comfort and safety. Excessive levels of vibration can put flexible structures at risk of failure and/or bring discomfort of occupants, resulting in expense and, possibly, loss of life. Examples of such structures are tall buildings, transmission and communication towers, long-span suspension bridges and generally, any member of a machine or a building structure of appreciable free span. Therefore, need exists to effectively suppress the level of vibration of such structures, subject to wind, earthquake and shock type loading. One way of such suppression is through intentionally inducing liquid sloshing in a partially full container, which is attached to the structure, to absorb and dissipate the structure's energy (V.J. Modi at al., 1996; V.J. Modi and S.R. Munshi, 1998; Y. Tamura at al., 1996).

A sloshing absorber consists of a container, partially filled with liquid to expose a free surface. A simple configuration is suggested in Figure 1.1 where a single degree-of-freedom structure is equipped with a liquid container possessing a free surface. The sloshing absorber is a passive device, relying on the structure's motion to excite the liquid. Consequently, sloshing waves are produced at the free surface, possessing energy dissipative qualities. There is a number of practical advantages of using this device, such as simple design, low manufacturing cost and minimal maintenance requirements. It may even be possible to design water storage facilities in tall buildings to perform double duty as vibration absorbers. A sloshing absorber can be retrofitted to existing structures, as well as incorporated into new construction.

Generally, deep liquid levels in sloshing absorbers produce standing waves, and possess inherently poor energy dissipation qualities, relative to those of travelling waves generated in shallow depths (V.J. Modi et al., 1996; V.J. Modi and S.R. Munshi, 1998; B. Guzel et al., 2005; A. Marsh et al., 2007). The primary objective of this thesis is to contribute to the understanding of liquid sloshing absorbers with shallow depths, in structural control applications. The secondary objective is to demonstrate the capabilities of a numerical modelling tool (Smoothed Particle Hydrodynamics – SPH) to predict fluid-structure interactions in such problems. To present the specific objectives, a brief description of the content of each chapter is given next. Each chapter is self contained, starting with its own introduction and literature review, followed by discussion and conclusions. All tables and figures are given at the end of each chapter.

An effective means of using intentionally induced liquid sloshing for structural control is investigated in Chapter 2. Simple experiments are presented, establishing the rectangular sloshing absorber as an effective controller of a light structure, undergoing resonant response. The experimentally observed motion of the container is imposed on the numerical model, and the resulting free surface motion is predicted using SPH. Free surface predictions are then compared with the experimental observations to establish the limitations of SPH. For shallow depths, acceptable free surface predictions are presented. The accuracy of predictions improve with liquid depth. The significance of Chapter 2 is in establishing the ability of SPH to approximate the characteristics of such flows. Such a tool is valuable for sloshing absorber design^{1,2}.

Efforts in design are then made in Chapter 3, to optimise the dissipation performance of the rectangular sloshing absorber without a structure. The container is disturbed with an imposed transient base motion, and then, the liquid is allowed to respond freely. This is a purely numerical investigation into the transfer of energy from the container, and its dissipation through sloshing. The effects of varying liquid depth and the container's width are reported. For a given excitation, the range of liquid depths at which travelling surface waves evolve into standing waves is identified. The energy dissipation characteristics of the fluid change significantly as a result of this change from a travelling to a standing wave. The contribution to knowledge from this chapter, includes the identification of specific behaviour and events occurring within the container, responsible for effective energy dissipation patterns. Suggestions are made to promote this behaviour, through appropriate selection of liquid depth and container width^{3,4}.

In practical applications, a sloshing absorber moves dynamically with the structure being controlled. This type of motion causes the fluid to 'interact' with the structure, exerting pressure forces on the container walls, and shear forces on the bottom. These interaction forces generate the required control of excessive structural oscillations. In Chapter 4, SPH is used to predict fluid-structure interaction forces, between a single degree of freedom structure and a rectangular sloshing absorber. The SPH predictions of structural motion and the liquid free surface shapes are compared to those observed experimentally. In addition to the kinematic comparisons presented earlier in Chapter 2, SPH is now shown to provide a sound prediction of the dynamics^{5,6}. To the author's knowledge, such predictions have not been available in the literature before.

Prior to the work in Chapter 5, a comparative study on the effect of different absorber shapes has not been reported in the literature, either. The objective of this chapter is to explore potential enhancements, with some simple, common shapes, different than a rectangle. As expected, the controlled structure's behaviour is found to be highly dependent on the absorber's shape. A simple shape modification to that of a rectangle is proposed, to produce superior energy transfer and dissipation patterns, across a broad range of excitation magnitudes^{7,8}.

The highly non-linear nature of liquid sloshing makes the identification of non-dimensional performance parameters difficult. As a result, the search for 'ideal' geometry must be conducted by means of experimental and/or numerical case studies, such as that in Chapter 5. This process makes progression in improving sloshing absorber geometry slow and extensive work. It is for this reason that the efforts in Chapter 6 are focused on exploiting the geometry of the hen's egg, a naturally occurring sloshing absorber, to control structural oscillations.

The hen's egg has evolved for the purpose of dissipating vibration energy quickly to protect its contents, the embryo. Dynamic motion of the egg-shell and its contents is predicted numerically with SPH, to demonstrate the effectiveness of the sloshing within. The physical events occurring within the egg that are responsible for effective energy dissipation are identified, explaining earlier experimental observations in So and Semercigil (2004). The possibility of modifying the egg's internal profile to further improve energy dissipation is then briefly explored. The significance of Chapter 6 is in the novel concept of using the geometry of the hen's egg as a sloshing absorber⁹.

In Chapter 7, the conclusions of the thesis are summarised. In addition, six short appendices are included in this thesis. A description of the SPH method is given in Appendix 1, to give the reader a basic understanding of the modelling technique. A resolution study is presented in Appendix 2, providing justification for the resolution used in the work of Chapters 2 and 4. To complement the work in these chapters, additional free surface comparisons are presented in Appendices 3 and 5, respectively. In addition to the work in Chapter 3, further kinetic energy histories are presented in Appendix 4 for completeness. In Appendix 6, oscillatory histories of the structurally modified egg-shell are presented, to complement the work in Chapter 6. Water is considered as the working fluid throughout the work in this thesis.

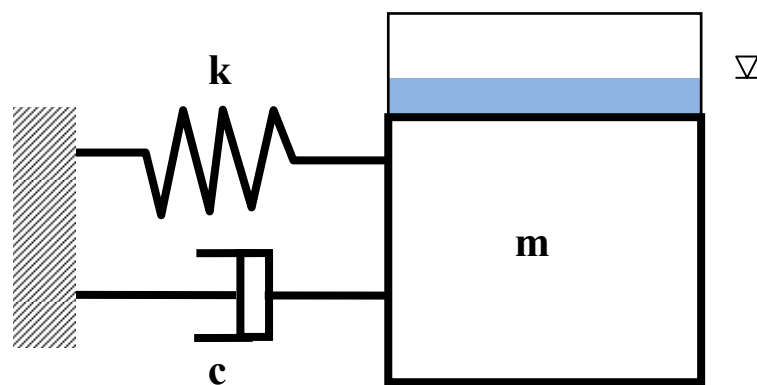


Figure 1.1. Tuned liquid damper, attached to a mechanical oscillator of mass m , stiffness k and viscous damping coefficient of c . The free surface is shown at a state of rest.

¹Experimental Observations and Numerical Predictions of a Shallow-Depth Sloshing Absorber for Structural Control. Marsh, A.P., Prakash, M., Semercigil, S.E. and Turan, Ö.F. Submitted to Journal of Fluids and Structures, June 2009.

²Experimental Findings and Numerical Predictions of Shallow Depth Sloshing Absorber Behaviour. Marsh, A.P., Prakash, M., Semercigil, S.E. and Turan, Ö.F. 16th Australasian Fluid Mechanics Conference (AFMC), 2007.

³A Numerical Investigation of Energy Dissipation with a Shallow Depth Sloshing Absorber. Marsh, A.P., Prakash, M., Semercigil, S.E. and Turan, Ö.F. Submitted to Applied Mathematical Modelling, June 2009.

⁴Numerical Investigation of Shallow Depth Absorbers for Structural Control. Marsh, A.P., Prakash, M., Semercigil, S.E. and Turan, Ö.F. 16th Australasian Fluid Mechanics Conference (AFMC), 2007.

⁵Predicting the Dynamic Structural Response Controlled by a Sloshing Absorber using SPH. Marsh, A.P., Prakash, M., Semercigil, S.E. and Turan Ö.F. Under preparation.

⁶Predicting the Dynamic Structural Response Controlled by a Sloshing Absorber using SPH. Marsh, A.P., Prakash, M., Semercigil, S.E. and Turan, Ö.F. 7th International conference on Computational Fluid Dynamics in the Minerals and Process Industries.

⁷A Study of Sloshing Absorber Geometry for Structural Control with SPH. . Marsh, A.P., Prakash, M., Semercigil, S.E. and Turan, Ö.F. Submitted to Journal of Earthquake Engineering and Structural Dynamics, September 2009.

⁸A Study of Sloshing Absorber Geometry for Structural Control with SPH. Marsh, A.P., Prakash, M., Semercigil, S.E. and Turan, Ö.F. 4th SPHERIC Workshop, 2009.

⁹A study of the Dynamics of a Natural Sloshing Absorber : The Hen's Egg – A Natural Sloshing Absorber. Marsh, A.P., Prakash, M., Semercigil, S.E. and Turan, Ö.F. Under preparation.

Chapter 2

EXPERIMENTAL OBSERVATIONS AND NUMERICAL PREDICTIONS OF A SHALLOW DEPTH SLOSHING ABSORBER FOR STRUCTURAL CONTROL

2.1 Introduction

In this chapter, an effective means of employing intentionally induced liquid sloshing within a container for structural control is investigated. A sloshing absorber can act as a damped dynamic vibration absorber as shown in Figure 2.1. Generally, a sloshing absorber is tuned so that the frequency of sloshing normally coincides with the natural frequency of the structure (Kareem, 1990; Banjeri et al., 2000). When designed properly, the sloshing fluid oscillates out of phase with respect to the motion of mass m , creating a counteracting pressure force on the side of the container. Shearing of the fluid is the primary form of mechanical damping in this type of absorber, provided that the liquid level is low (Kareem, 1990; Marsh et al., 2009a).

Simple experiments are described here involving a sloshing absorber. The objective of the experimental work is to establish the sloshing absorber as a promising controller for light structures, prone to resonant response. In addition, experimental observations are useful to determine the effect of varying liquid depth on structural control.

Smoothed Particle Hydrodynamics (SPH) is used to model 2-dimensional liquid sloshing absorbers. CSIRO's Mathematical and Information Sciences Division have developed the code used here. Similar work has been undertaken with this code and can be found in Cleary et al., 2007. The objective of the numerical work is to test the accuracy of the predicted free surface, through comparisons with experimental observations, for given prescribed container motion. The validated numerical model can be used for the design and optimisation of such structural control devices. The cases reported in this chapter should be interpreted as the first stage towards the prediction of full fluid-structure interaction where the motion of the container is the result of the structural response to sloshing fluid forces. The numerical prediction of full fluid-structure interaction is presented in Chapter 4 of this thesis.

SPH is a Lagrangian method of solving the equations of fluid flow, suitable for modelling liquid sloshing due to its grid-free nature and inherent ability to model complex free surface behaviour (Monaghan, 1992; Monaghan, 1994). The method works by tracking particles and approximating them as moving interpolation points. These fluid particles (or moving interpolation points) have a spatial distance over which field variables such as density, velocity and energy are smoothed. This is achieved via an interpolation kernel function.

SPH has been successfully applied to a wide range of industrial fluid flow applications (Cleary et al., 2002; Cleary et al., 2006; Cleary et al., 2007; Prakash, 2007). SPH has also been used to successfully model sloshing dampers used as anti-roll tanks, in marine engineering applications to dampen a vessel's roll motion (Bulian et al., 2009; Delorme et al., 2006; Souo-Iglesias et al., 2006; Souo-Iglesias et al., 2004). A detailed description of the method can be found in Monaghan, 1992. A brief description of the method is presented in Appendix 1.

2.2 Experimental Procedure

The experimental setup shown in Figure 2.2 consists of a mechanical oscillator whose structure is configured as an inverted pendulum. Structural stiffness is provided by attached springs. It has been reported that the inverted pendulum arrangement can enhance the energy dissipation of a sloshing absorber by up to 7-fold as compared to that experienced in pure translation (Lu et al., 2004).

A rectangular container to accommodate the sloshing absorber is mounted on the pendulum, 670 mm above the pivot point. Hence, as the structure is excited, the container is subjected to angular oscillations. The structural parameters and container dimensions are given in Table 2.1. The structure is controlled by filling the container with water to varying depths from 2.75 mm to 22 mm. The behaviour of each case is then compared to that of the uncontrolled structure without water.

The disturbance is provided from an initial angular displacement of 16 degrees. A simple stop-block allows consistent initial conditions for all cases. The structure is released from this initial position and allowed to oscillate freely. Experimental observations are video recorded with a standard digital camera, at a speed of 20 frames per second. Such frame speed is sufficient, where the largest fundamental frequency of the structure is in the order of 0.3 Hz. Experimentally recorded structure motion is accurate to within ± 0.05 s and ± 1 degree.

The mass moment of inertia of the uncontrolled structure is measured to be approximately $3.2 \text{ kg.m}^2 \pm 0.1 \text{ kg.m}^2$ about the centre of rotation. This value was calculated by weighing the structure's parts then using the parallel axis theorem. The ratio of mass moment of inertia of fluid (when the container is in the neutral horizontal position) to that of the structure for the above mentioned liquid depths are listed in Table 2.2, along with the corresponding mass ratios.

2.3 Numerical Procedure

The experimental setup shown in Figure 2.2 is modelled numerically with varying liquid depths using SPH. A rigid boundary (representing the container) having the same experimental dimensions, is placed 670 mm above the pivot point, replicating the structure arm seen in Figures 2.2 (a) and (b). It is then filled with different levels of water with a density of 1000 kg m^{-3} and viscosity of 0.001 Pa s . A smoothing length of 1.2 is chosen. This length scale is the ratio of the actual interpolation length to the particle's mean distance. This value is used widely in SPH for predicting free surface flows (Liu and Liu, 2003). The effect of increasing smoothing length is explained in Section 4.4.4. As described in Appendix 1 and Section 4.4.4, smoothing length defines the integration area of the particle of interest.

A particle cross-sectional area of $0.5 \text{ mm} \times 0.5 \text{ mm}$ is used to produce enough resolution to capture all flow characteristics, without extending computational time unnecessarily. Four times as many SPH particles are needed to increase resolution by a factor of two for a two dimensional problem. A resolution study is presented in Appendix 2, establishing the above mentioned particle size as suitable for modelling such flows.

Using the above mentioned particle size, 8404 SPH particles are needed to represent the system with 5.5 mm liquid depth, 6494 fluid particles, and 1910 boundary particles representing the container. At 22 mm liquid depth, 30937 SPH particles are needed, 29027 fluid particles, and 1910 boundary particles. A 3.2 Ghz Xeon processor is used for computation.

The time stepping in this code is explicit and is limited by the Courant condition modified for the presence of viscosity, given in Appendix 1, Equation (A15). The time step used in all simulations is 2.5×10^{-5} s. The total simulation time is chosen to ensure all structure motion is modelled, from the point of release until motion has ceased, and therefore varies depending on liquid level.

To replicate the experimental conditions, the container is given an initial displacement of 16 degrees clockwise, and allowed for 4 seconds to settle the fluid particles, approaching zero velocity. The experimentally observed motion of the container is then imposed on the numerical model to excite the fluid. Simulations are performed in 2-dimensional space.

2.4 Experimental Observations

Angular displacement histories of the uncontrolled case, along with the 2.75 mm, 5.5 mm, 8.25 mm, 11 mm and 22 mm liquid depth cases are shown in Figures 2.3(a) to 2.3(f). The uncontrolled case in Figure 2.3(a) experiences just over seven cycles of oscillation in the first 22 seconds. The frequency of oscillations decreases with the increasing amount of water in the absorber. 2.75 mm depth undergoes six full cycles of oscillation before coming to rest, whereas the 22 mm case experiences only one and a half cycles. The reduction of the frequency of oscillation is the result of negative stiffness imposed by the inverted pendulum configuration, and (to a smaller extent) the added mass.

The behaviour observed at 2.75 mm and 5.5 mm depths is expected for an under-critically damped freely vibrating system (Rao, 1995). For the 8.25 mm depth, some interesting behaviour is observed during the third cycle of oscillation, around $t = 10$ s. At this instant, the pressure force exerted on the right container wall by the fluid is sufficient to change the structure's direction of motion. 11 mm depth exhibits similar behaviour to those of 2.75 mm and 5.5 mm depth. The response of the structure at 22 mm depth is drastically different, no longer possessing exponential decay to represent its behaviour. The added mass is assumed to be the reason for this.

The effectiveness of a sloshing absorber increases as the free surface motion becomes more violent (Banjeri et al., 2000). At shallow liquid depths of 2.75 mm and 5.5 mm, fluid motion is energetic. Strong hydraulic jump and wave breaking are observed. As liquid is added, the structure's motion becomes increasingly more lethargic, transferring less energy to the fluid. Less violent free surface behaviour is observed as a result.

The equivalent damping ratio for each half cycle in Figure 2.3 is marked directly above peaks of rotation. The magnitudes shown indicate the amount of damping produced by one full cycle of oscillation, ending at this peak. Generally, damping increases as the number of cycles experienced by the structure increases. In all cases except for the depth of 11 mm, the highest damping is observed in the last two cycles of oscillation. Damping also increases with liquid depth. The reason for this is presumed to be the negative stiffness and added mass effects. All controlled cases produce a significant increase in damping relative to the uncontrolled case.

Summary of the settling times of all cases is shown in Figure 2.4. The settling time is defined as the time taken from the instant of the structure's release to when its motion has ceased, residing in the central rest position. Cases employing any level of liquid produce considerable reductions in settling time, relative to that of the uncontrolled case. An optimum condition exists between the liquid depths of 2.75 mm and 8.25 mm, the marginally best performer being the 5.5 mm case. It is interesting to notice that the control performance of the sloshing absorber, at least in terms of settling time, is virtually independent of the liquid level for a significantly wide range to the right of 5.5 mm. Such an apparent insensitivity is a great advantage from a practical point of view.

These experimental observations clearly demonstrate the effectiveness of the suggested vibration controller in this section. Hence, further investigation into the physical events responsible for the dissipative qualities is certainly warranted.

It is quite impractical to identify the intricate flow behaviour through flow visualisation alone. Therefore, efforts have been made in the numerical simulations, which are discussed in the following section. Once the accuracy of the modelling tool is established, efforts are concentrated on design, focusing on enhancing the energy dissipation mechanism for better structural control.

2.5 Numerical Predictions

The nominated instances analysed in this section are chosen either as points of reference (when the structure is in the central rest position or at peak displacement) or at points in time where fluid behaviour is exceptionally interesting and/or difficult to capture numerically. The purpose of choosing these instances is to give the reader a complete picture of the modelling tool's capabilities, as opposed to a biased view.

2.75 mm liquid depth was not simulated further due to the predicted free surface shapes being different from those seen experimentally at such low depths.

2.5.1 Liquid depth of 5.5 mm

Free surface comparisons at 5.5 mm liquid depth are shown in Figure 2.5. The left hand column represents experimental findings at certain instants in time. The numerical predictions are shown in the right hand column. Figures 2.5(a) and (b), (c) and (d), (e) and (f), (g) and (h), (i) and (j), (k) and (l), and (m) and (n) correspond to times of 0.00 s, 0.95 s, 1.30 s, 1.60 s, 1.85 s, 2.75 s and 3.70 s, respectively, from the instant of release.

The structure supporting the sloshing absorber is set to an initial clockwise rotation of 16 degrees. This instant is shown just prior to release in Figure 2.5(a), at $t = 0.00$ s. The fluid is seen at the bottom right hand corner of the container. The structure is held in this position until fluid motion is no longer noticeable. The numerical model in Figure 2.5(b) emulates the same behaviour observed, after positioning the container and allowing the fluid particles to settle.

Once released, the structure rotates from right to left. Motion is energetic, passing through the central rest position at $t = 0.95$ s, as shown in Figure 2.5(c). The structure's motion produces travelling wave development in the same direction. Fluid distribution and travelling wave development are predicted well in Figure 2.5(d). However, the predicted free surface is somewhat bumpier than that observed.

At $t = 1.30$ s, in Figures 2.5(e) and 2.5(f), the travelling wavefront collides with the left hand container wall. Fluid is distributed over the entire container bottom at this instant. Wave-to-wall interaction has only just commenced at the left side of the container. The numerical fluid distribution is comparable to that observed, but fluid has not yet reached the container wall.

Energetic wave-to-wall interaction ensues. Fluid flow is laminar and of high velocity (1.1 m/s to 1.2m/s at the wavefront) as it approaches the container wall. Sudden change in the direction of the container contact surface causes the fluid to climb the container wall, producing the strong moving surge hydraulic jump shown in Figure 2.5(g). Such an event produces a rapid transition from a supercritical to subcritical regime fluid flow (Murzyn and Chanson, 2007; Sturm, 2001). Supercritical flow occurs when fluid velocity (V_f) is larger than the shallow-water wave propagation speed C_0 (White, 2003), defined in Equation (1) below, where h_f is the fluid depth and g is the acceleration due to gravity. Kinetic energy is transferred into potential energy due to the change in fluid elevation.

$$C_0 = \sqrt{h_f g} \quad (1)$$

Hydraulic jump is predicted numerically, shown in Figure 2.5(h). The forecasted fluid elevation of the hydraulic jump is similar to that observed experimentally. However, an exaggerated swirling flow pattern is predicted. The elevated fluid then collapses on itself under gravity. Flow becomes turbulent at this point in time, characteristic of hydraulic jump (Chanson, 1999). Steep velocity gradients are produced as a result, along with inherent viscous dissipation due to shear stress. A small amount of air entrainment is seen in the form of bubble formation in Figure 2.5(h).

The structure achieves maximum anti-clockwise rotation at $t = 1.85$ s. As shown in Figure 2.5(i), the free surface is uneven due to swirling fluid behaviour at this time. Around 80% of the container length is exposed. The prediction in Figure 2.5(j) exhibits a slightly sparser distribution; less than two thirds of the container length is predicted to be dry. Swirling behaviour is also seen numerically.

The structure motion commences from left to right shortly after, producing a travelling wave in the same direction. In Figure 2.5(k), the structure is passing through the central rest position at $t = 2.75$ s. The predicted fluid distribution agrees closely with that observed, as illustrated in Figure 2.5(l). The free surface predicted is rougher than that observed experimentally.

Wave-to-wall interaction commences at $t = 3.15$ s, producing a smaller hydraulic jump of the same type, at the right hand container wall. Rotation in the clockwise direction ceases shortly after, at $t = 3.70$ s. The free surface shape at this instant, shown in Figure 2.5(m), is smooth; around one third of the container length is exposed. The predicted fluid behaviour differs from that observed, possessing the irregular free surface shape shown in Figure 2.5(n). Almost two thirds of the container length is predicted to be dry. Motion ceases at around 13 s.

From the comparison with the experimental results as presented in Figure 2.5, the fluid distribution and position have been captured well numerically for 5.5 mm liquid depth. The travelling wavefront position is predicted accurately. Although this is the case, predicted free surface shapes are generally more uneven than those observed. This result is expected to be due to some bumpiness in the imposed motion, caused by the code interpolating linearly between data points. The main discrepancies in free surface shape and fluid behaviour are seen during wave-to-wall interactions. Exaggerated swirling behaviour is predicted during hydraulic jump, whilst the fluid is most energetic.

2.5.2 Liquid depth of 22 mm

Free surface comparisons of the 22 mm liquid depth case are shown in Figure 2.6. Figures 2.6(a) and (b), (c) and (d), (e) and (f), (g) and (h), (i) and (j), (k) and (l), and (m) and (n) correspond to times of 0.00 s, 1.65 s, 2.00 s, 4.35 s, 6.00 s, 7.20 s and 10.15 s, respectively, from the instant of the structure's release.

As in shallower depths, a travelling wave is produced in the direction of the structure's motion. Figure 2.6(c) corresponds to 1.65 s after release. In contrast to lower liquid levels, the structure's motion is lethargic, the travelling wavefront having just collided with the left container wall. Undulating hydraulic jump is observed here, as opposed to the strong jump seen at lower liquid levels during the first wave-to-wall interaction. Minimal energy seems to be dissipated as a result, relative to shallower depths. Fluid particle velocities at the wavefront are around 0.35 m/s. Undulating hydraulic jump is predicted accurately in Figure 2.6(d).

Elevated, subcritical flow evolves into travelling wave movement starting from the left wall, opposing the main body of fluid still moving in the opposite direction. This wave can be seen in Figure 2.6(e) as the structure passes through the central rest position. The structure continues to rotate from right to left until maximum anti-clockwise rotation at $t = 4.35$ s, shown in Figure 2.6(g). All kinetic energy has been converted to potential, the structure's motion has ceased, and all fluid particles reside at the left hand side of the container. The corresponding simulation results are shown in Figure 2.6(h). Numerical and experimental free surface shapes, and fluid distribution are analogous.

As the structure oscillates back towards the central rest position, fluid flows from left to right within the container. At $t = 6.00$ s, fluid is almost touching the right side container wall, as shown in Figure 2.6(i). The numerical solution shown in Figure 2.6(j) predicts a free surface shape that closely matches that observed. The free surface is smooth as the structure passes through the central rest position at $t = 7.20$ s, shown in Figure 2.6(k). The numerical prediction is identical, shown in Figure 2.6(l). The container comes to rest at a maximum clockwise rotation of around 10.5 degrees occurring at $t = 10.15$ s, shown in Figure 2.6(m). Around one third of the container bottom is dry. The numerical prediction shown in Figure 2.6(n) is in agreement with the experimental observations. The motion ceases at $t = 22.60$ s.

All experimentally observed behaviour is replicated using SPH at this liquid depth, 22 mm. Differences between empirical and numerical free surface shapes are minimal. Undulating hydraulic jump is predicted well at this depth. Free surface comparisons of 8.25 mm and 11 mm liquid depths have been completed and are presented in Appendix 3. They are not shown here since little additional understanding is provided by them. Throughout all cases, fluid distribution and position have been captured well numerically. Differences in free surface shape between experimental observations and predictions become less significant as liquid depth increases. Travelling wave development is predicted well. Wavefront position, along with the expected high particle velocities at this location has been captured soundly.

Based on this rather strict form of comparison, the numerical modelling tool is seen to produce exceptional free surface predictions, the accuracy of which improves with increasing liquid depth. SPH has been found to be satisfactory for modelling liquid depths of 5.5 mm and higher with imposed container motion. Since these results are encouraging, SPH is used to predict structural motion through fluid-structure interaction in Chapter 4. This relative insensitivity to the details of the free surface, is due to the pressure force exerted on the structure by the fluid being an integral effect.

2.6 Conclusions

Sloshing absorbers are promising vibration control agents for light structures that are prone to resonance. They are of simple design, are cheap relative to the tuned mass damper (TMD) and other alternatives, and maintenance free due to the absence of mechanical parts such as springs and dashpots.

The primary form of energy dissipation in a sloshing liquid is shearing of the fluid, in the form of travelling and breaking waves and hydraulic jump. Shear stress is increased through providing steep velocity gradients. Wave-to-wall interactions are responsible for producing discontinuities in the flow field and therefore, steep velocity gradients. A significant mechanism of energy dissipation in all depths is the hydraulic jump. Hence, this phenomenon should be encouraged. Energy dissipation caused by hydraulic jump is directly proportional to its height (Sturm, 2001). Jump height is maximised by producing a travelling wavefront of highest possible velocity, just prior to its collision with a container wall.

Generally, fluid distribution and free surface shape are predicted accurately, validating the merit of SPH to model such free surface flows. Details of wave-to-wall interaction at depths lower than 5.5mm (where particularly strong hydraulic jumps are observed) differ slightly from those observed experimentally. Otherwise, fluid behaviour is predicted well numerically even for the extremely shallow cases. Therefore, it is concluded that SPH is a sufficiently accurate prediction tool for modelling the sloshing motion of a liquid within a container given an imposed motion, at liquid depths of 5.5 mm and higher.

Table 2.1. Experimental set-up parameters. Mass and length are reported with an estimated accuracy of 0.010 kg and 0.001m, respectively.

Mass (kg)	16.6
Equivalent viscous damping ratio	0.015 ± 0.002
Inertia (uncontrolled) kg m^2	3.2
Container length x width x depth (mm)	340 x 230 x 142

Table 2.2. Rotary inertia and mass ratios of fluid (when initially quiescent) to those of the structure for different liquid depths.

Depth ± 0.25 (mm)	Inertia ratio	Mass ratio
2.75	1/32	1/80
5.5	1/16	1/40
8.25	1/10	1/26
11	1/8	1/20
22	1/4	1/10

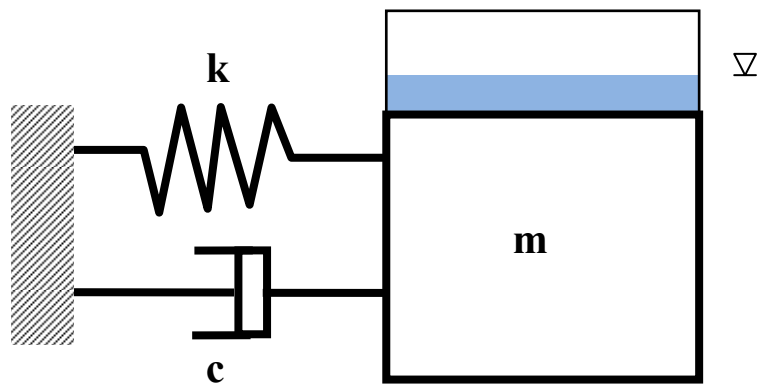


Figure 2.1. Sloshing absorber, attached to a mechanical oscillator of mass m , stiffness k and viscous damping coefficient of c . Repeated from Figure 1.1 for easy reference.

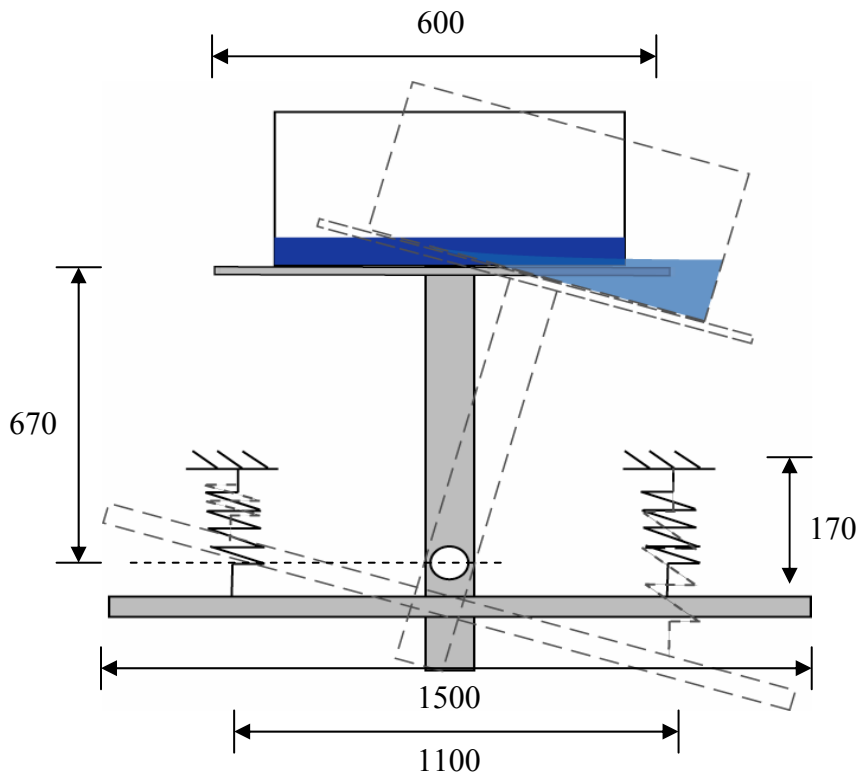


Figure 2.2(a). Schematic showing the structure and the tuned absorber. Dimensions are in millimetres (mm).



Figure 2.2(b). Photograph of experimental setup.

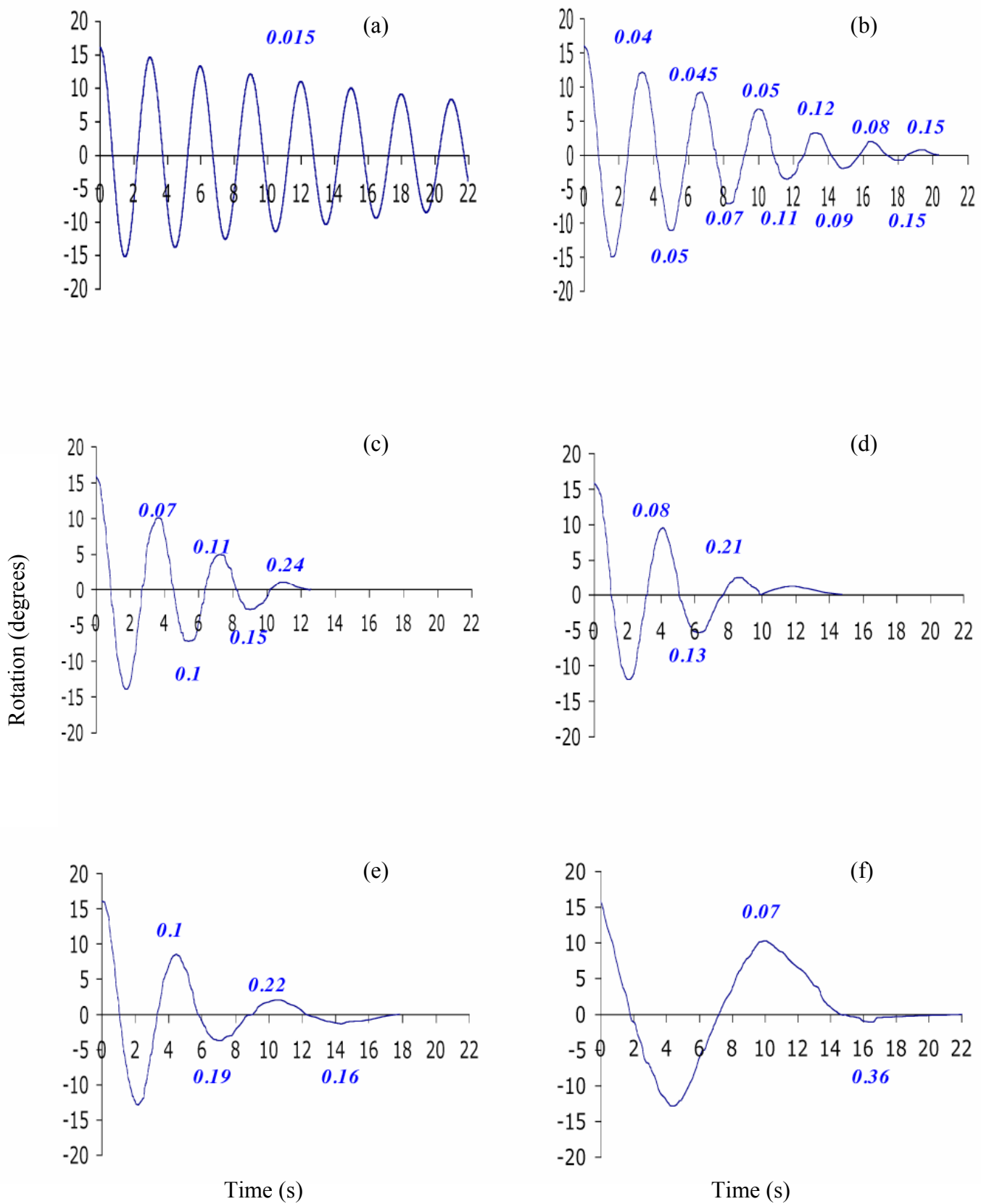


Figure 2.3. Angular oscillation histories of (a) uncontrolled, (b) 2.75 mm, (c) 5.5 mm, (d) 8.25 mm, (e) 11 mm and (f) 22 mm deep cases.

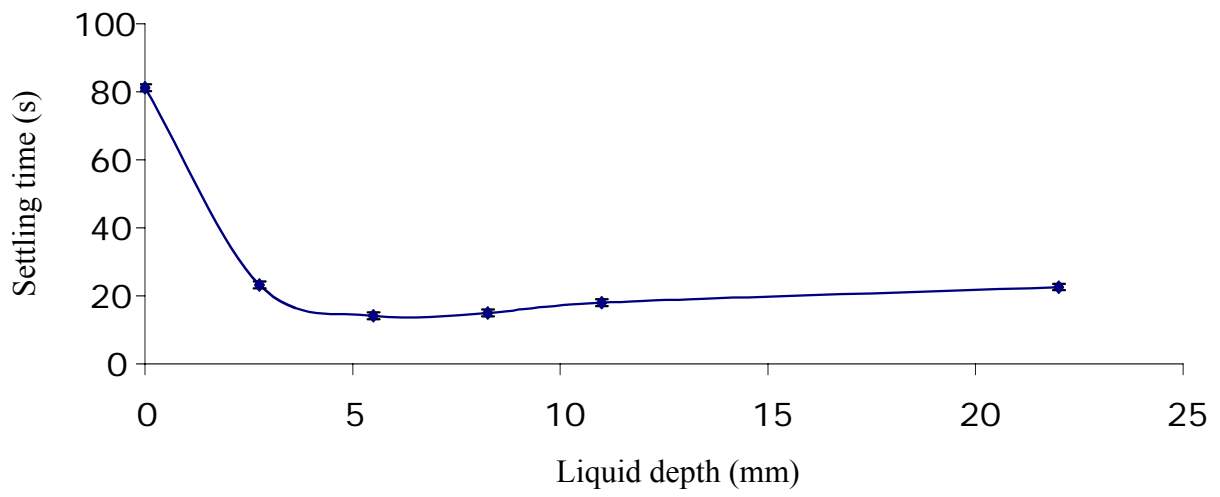


Figure 2.4. Variation of settling time with different water depths.

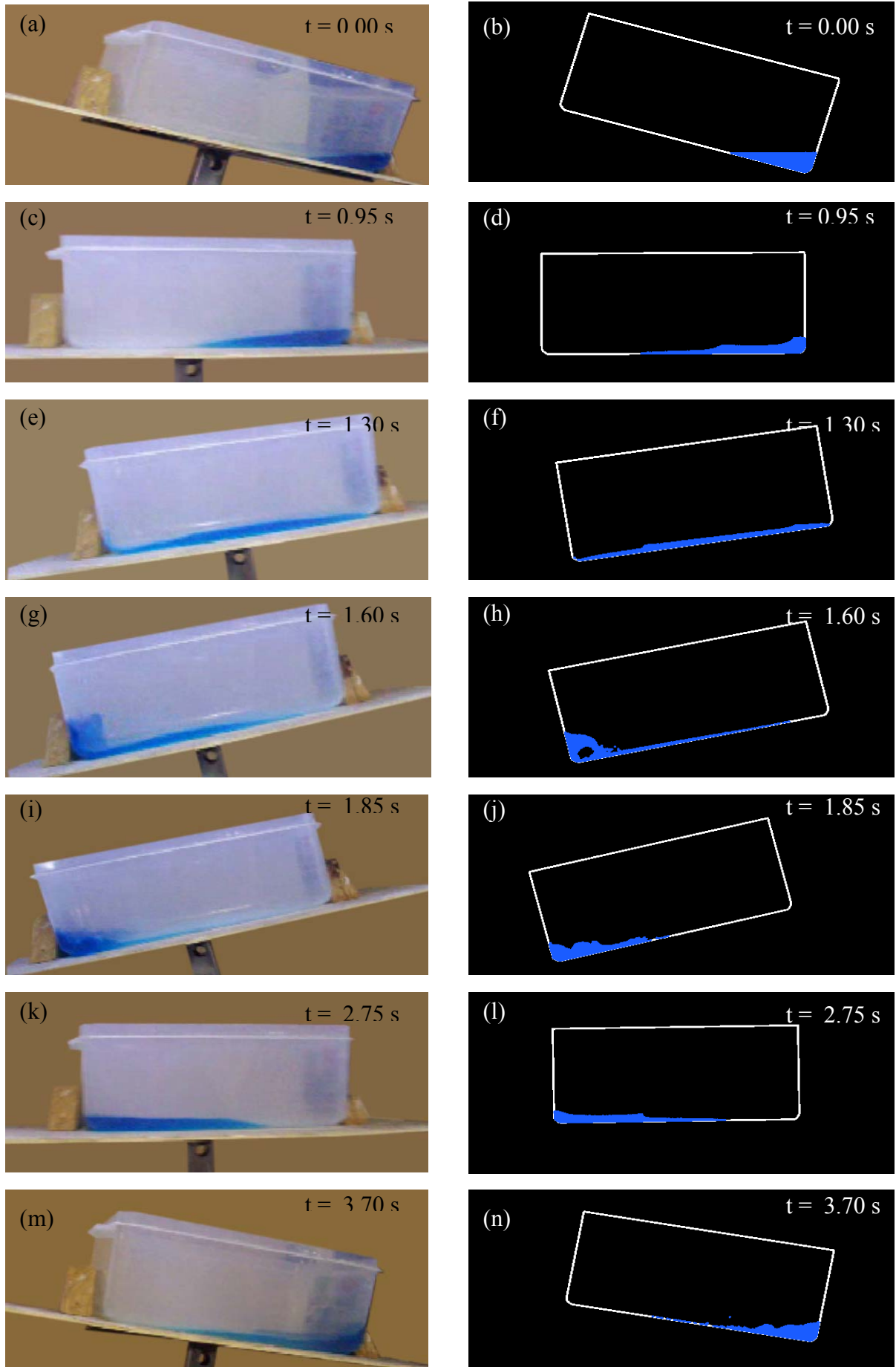


Figure 2.5. Free surface comparisons of 5.5 mm liquid depth; left column has the experimental observations, right column has the numerical predictions.

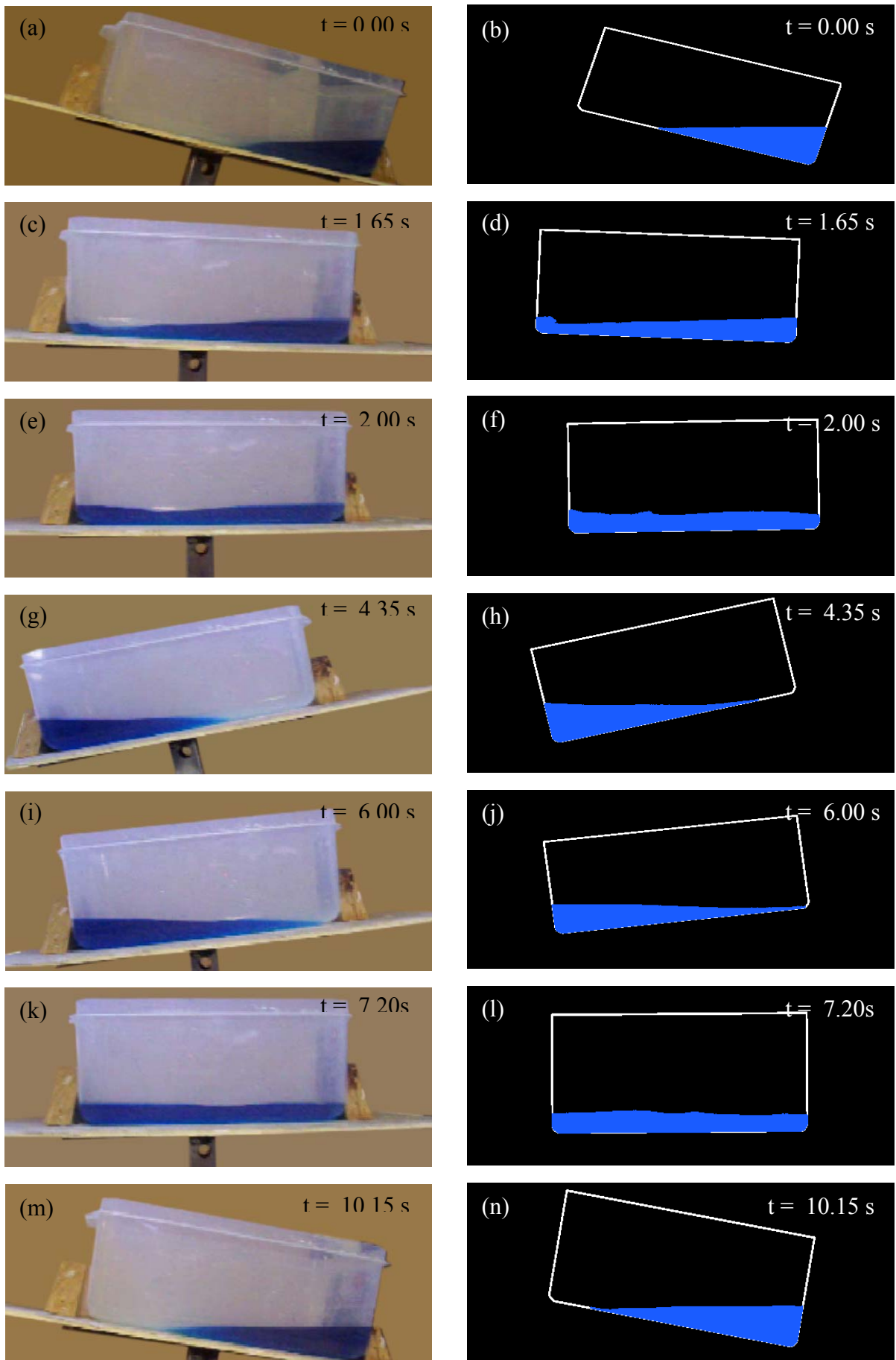


Figure 2.6. Same as in Figure 2.5, but for 22 mm liquid depth.

Chapter 3

A NUMERICAL INVESTIGATION OF ENERGY DISSIPATION WITH A SHALLOW DEPTH SLOSHING ABSORBER

3.1 Introduction

In Chapter 2, SPH was found to provide a sound representation of the fluid behaviour within a rectangular sloshing absorber for depths as shallow as 5.5 mm, when the container's motion is imposed. In this chapter, SPH is used as a design tool, to investigate the effects of varying liquid depth and container width on the energy transfer and dissipation characteristics of the rectangular sloshing absorber. Such numerical studies can indicate more readily the relative importance of the absorber's source of energy dissipation. The same SPH code has been used here as that in chapter 2.

Liquid sloshing in rectangular tanks have long been an area of study (Colagrossi at al., 2004; Colagrossi at al., 2006; Modi and Munshi, 1998). However, the complex free surface behaviour (such as wave breaking and collision) exhibited by such a system has limited the numerical prediction attempts. Such behaviour is of great interest in structural control applications due to its intrinsic ability to dissipate energy quickly.

Various studies focused on using liquid sloshing as a structural control mechanism can be found in the literature. The effects of implementing flexible container walls (Gradinscak, 2002), a net for the fluid to pass through (Kaneko and Mizota, 2000) and the employment of baffles (Anderson et al., 2000) on the energy dissipative characteristics of deep liquid level absorbers have been analysed, all showing improved energy dissipation qualities. However, the principal standing waveform observed at these deep liquid levels is inefficient in nature relative to the travelling waveform observed in shallow liquid levels (Guzel et al., 2005; Marsh et al., 2007).

Studies involving varying liquid depth in a rectangular container of constant width have been undertaken, focusing on the amount of energy dissipation produced (Modi and Munshi, 1998; Reed et al., 1998). Yet, the liquid depth at which the transition from travelling to standing wave development occurs, has not been investigated for a given container width.

Generally, the container width is tuned so that the natural sloshing frequency coincides with the natural frequency of the structure to be controlled (Banjeri et al., 2000). In liquid depths producing strong travelling wave development, this may not be as important. Instead, the focus can be on increasing energy transfer and dissipation through tuning.

The primary objective of this work, is to numerically demonstrate the effect of varying liquid depth and container width, on the energy transfer and dissipation characteristics of a rectangular absorber subject to a specific sinusoidal excitation. Smoothed Particle Hydrodynamics (SPH) is used as a numerical tool in this study to model two dimensional rectangular liquid sloshing absorbers. Physical events that enhance energy dissipation are commented on. Results are presented in the form of numerical case studies.

3.2 Numerical model and procedure

The fluid within the container is left to settle under gravity for a period of one second so that it reaches a zero energy initial state. After this, it is subjected to a sinusoidal excitation for one complete period, of frequency 1.4 Hz and 50 mm amplitude. The fluid is then allowed to respond naturally to the excitation within the container. The total simulation time is 20 seconds. Due to the base excitation imposing increasing amounts of kinetic energy to the fluid as its mass increases, all analysis is presented on a per unit mass basis. The numerical model and base excitation history are illustrated in Figure 3.1.

Due to deeper liquid depths being modelled in this chapter, a particle size of 0.8 mm x 0.8 mm is used to represent the fluid and boundary, in order to reduce computational expense. This particle size is significantly larger than that of 0.5 mm x 0.5 mm, used in Chapter 2. However, the difference in the predicted fluid behaviour between the two resolutions is minimal. Histories of kinetic energy produced at both resolutions, for the representative case of 20 mm depth in a 400 mm wide container, are shown in Figure 3.2. Energy magnitudes and dissipation behaviour are quite similar. As a result, this resolution is expected to provide accurate predictions.

3.3 Observations

An efficient absorber transfers a substantial amount of energy from the structure on which it is attached, to the working fluid. This energy is to be dissipated as quickly as possible. The primary means of energy dissipation seems to be shearing of the fluid. Hence, energy dissipation is enhanced as the velocity gradients in the flow become steeper. Two main events produce steep velocity gradients in a sloshing liquid, namely wave-to-wave and wave-to-wall interactions. In general, wave-to-wave interactions seem to be more effective. This is due to the opposing particle velocities in the two approaching surface waves. The interaction produces steep velocity gradients as a result. Travelling and/or standing waveforms can exist in a sloshing liquid. A travelling wave is capable of producing both type of interactions mentioned, whereas standing waves primarily produce wave-to-wall interactions.

3.3.1 Kinetic energy dissipation

Histories of the sum of kinetic energy per unit mass for cases simulated in a container of 400 mm width are shown in Figure 3.3. The kinetic energy (ke) of a particle is calculated using Equation (2), where m and v are the particle's mass and velocity, respectively. Figures 3.3(a) to 3.3(h) correspond to the liquid depths of 5, 10, 15, 20, 40, 60, 80 and 100 mm, in descending order. Positions indicated with a red mark specify the point of overall maximum kinetic energy, the magnitude of which signifies the energy transfer from the base excitation to the sloshing liquid on a per unit mass basis. All liquid depths were also simulated in container widths of 200 mm and 600 mm, the histories of which are not shown here for brevity. Similar behaviour was observed for all container widths. Instead, these results are included in Appendix 2.

$$ke = \frac{mv^2}{2} \quad (2)$$

Peaks in the kinetic energy histories correspond to high particle velocities, usually when the free surface shape is relatively flat. Troughs in the kinetic energy histories are observed when the fluid is close to largest free surface deformation, corresponding to high potential energy. In cases where periodic behaviour is observed in the history of kinetic energy, two wave-to-wall interactions take place per sloshing cycle, producing two peaks and two troughs. In these cases, the dominant liquid sloshing frequency predicted compares well with the exact solution defined in Milne-Thomson (1968).

Based on the results presented in Figure 3.3, depths of 20 mm and lower produce desirable energy dissipative characteristics. Liquid levels in Figures 3.3(a) to 3.3(d) produce irregular histories, along with an inherent steeper rate of dissipation relative to deeper levels. At these shallow depths, predominant travelling wave formation is observed.

Periodic behaviour is observed as liquid depth increases with the energy dissipation becoming more gradual. The distinct transition from seemingly stochastic behaviour to periodicity is noticeable from Figures 3.3(d) to 3.3(f). A transitional phase between the two behaviours is seen in Figure 3.3(e). The physical significance of this transition is the change in principal waveform from travelling to standing.

In general, the overall time taken to dissipate the total energy increases with liquid depth. The shallowest case of 5 mm dissipates its energy the quickest. The deepest case of 100 mm has the slowest rate of energy dissipation. The rate of dissipation decreases slightly between the depths of 5 mm and 20 mm, yet there is an approximate 5-fold increase in the amount of energy transferred from the excitation to the working fluid. Energy transfer increases with liquid depth. However, cases deeper than 20 mm generate standing waves, sacrificing energy dissipation performance.

3.3.2 Probability density

Probability densities of the kinetic energy histories in Figure 3.3 are shown in Figure 3.4. Such densities show the amount of time spent within a given kinetic energy range (each range is represented by a vertical bar) as a fraction of the total. An ideal energy dissipater would spend all its time in the left most bar, corresponding to the lowest possible kinetic energy.

Figures 3.4(a) through to 3.4(h) correspond to the liquid depths of 5, 10, 15, 20, 40, 60, 80 and 100 mm, in descending order. Liquid depths from 5 mm up to 20 mm possess good energy dissipative qualities relative to deeper levels. These simulations spend well over half their time within the left most kinetic energy bar. The 20 mm liquid depth remains at the lowest possible kinetic energy for almost 70% of the total time.

Energy dissipation performance decreases as liquid depth is increased. Probability densities spread to the right as the water level gets deeper, illustrating the introduction of mid-range kinetic energy. Standing wave development is the cause of this change. The transition from travelling to standing wave formation is seen by comparing Figures 3.4(d) and 3.4(h). In contrast to 20 mm depth, 100 mm depth spends only 18% of the total time at the lowest possible energy.

3.3.3 Settling times

A summary of the settling times for varying liquid depths in the 200 mm wide container is shown in Figure 3.5. In this figure, the horizontal axis indicates liquid depth whereas the vertical axis represents settling time in seconds. Settling time is defined as the time taken for the kinetic energy within the fluid to reach a certain percentage of the maximum amount introduced into the system. In the figure, this percentage is set to 1, 2, 5, 10 and 25%.

There is no significant difference in settling time for depths up to and including 20mm. Settling time is low at these depths, due to the dominant travelling wave development observed. A step change in the settling time is seen between the depths of 20 mm and 60 mm, resulting in a steep increase of around 3 fold. Settling times do not change significantly after a liquid depth of 60mm. Principal standing wave development is observed at these deep liquid levels. The transition from travelling to standing wave formation is responsible for the step change in the settling time.

The same analysis as in Figure 3.5 is shown in Figure 3.6 for the 400 mm wide container. As in a 200 mm wide container, settling time remains relatively low up until and including the 20 mm depth. At 40 mm depth, the evolution in waveform from travelling to standing causes a step change in settling time. At the deepest liquid level of 100 mm, 2% residual energy is not reached within the total observation time of 20 seconds.

A summary of the settling times for the 600 mm wide container is shown in Figure 3.7. As in narrower containers, the settling time remains relatively low up to and including 20 mm liquid depth. From here, the magnitude increases sharply with liquid depth. At the liquid levels of 80 mm and 100 mm, 2% residual energy is not reached within the total simulation time of 20 seconds.

3.3.4 Kinetic energy transfer from the base

The maximum kinetic energy transferred from the moving base to the fluid for varying liquid depths and for container widths of 200 mm, 400 mm and 600 mm, is shown in Figure 3.8. In a container of 200 mm width, an optimal energy transfer condition is predicted at a depth of around 60 mm. For container widths of 400 mm and 600 mm, more energy is transferred into the fluid on a per unit mass basis as liquid level increases. A similar optimal energy transfer condition to that seen in 200 mm container width is expected in these wider containers, occurring at liquid depths higher than those simulated.

The effectiveness of a sloshing absorber increases as free surface motion becomes more violent. The energy required to produce a travelling wave increases with liquid depth. For a high excitation level, the energy transmitted is large, and even absorbers with relatively deep liquid levels can produce wave breaking (Banjeri et al., 2000). Therefore, the conclusion given at the end of Section 3.3.3, regarding the liquid depth range for waveform transition is excitation dependent.

3.3.5 Flow visualisation

Visualisations of 20 mm liquid depth in a 400 mm wide container are shown in Figure 3.9. The scale shown below each frame indicates fluid velocity in metres per second. As in all other cases, the fluid is allowed to settle under gravity for a period of one second, after which the sinusoidal base excitation is applied for one complete cycle.

Container motion commences from right to left, producing a travelling wave (travelling wave 1) in the same direction, shown in Figure 3.9(a) at $t = 1.27$ s. The fluid velocity is high at the wavefront, creating steep velocity gradients. As the prescribed motion changes direction, a second travelling wave develops (travelling wave 2) at the left hand container wall. At $t = 1.42$ s, travelling wave 2 is seen in Figure 3.9(b), moving from left to right, opposing the direction of travelling wave 1. The total kinetic energy increases steadily from when the first travelling wave is generated, up until maximum is observed at $t = 1.57$ s. Travelling waves 1 and 2 are close to collision at this point, shown in Figure 3.9(c).

Immediately after peak kinetic energy is observed, the two opposing travelling waves collide producing a wave-to-wave interaction near the left side container wall. This interaction is responsible for the first sharp decline in kinetic energy after the maximum is observed. A break in the free surface is seen just after as a result of this interaction at $t = 1.61$ s, shown in Figure 3.9(d).

The observed kinetic energy continues to decrease until it reaches the first trough after the maximum kinetic energy is reached, seen in Figure 3.3(d) at $t = 1.71$ s. The predicted free surface is shown in Figure 3.9(e). Complex behaviour is observed including fluid fragmenting and leaving the free surface. It should be noted that low kinetic energy corresponds to large free surface deformation (high potential energy). The fluid velocity range in Figure 3.9(e) is almost one half of that in Figure 3.9(d).

Kinetic energy increases slightly until the second peak is observed in Figure 3.3(d), at $t = 1.80$ s. Fluid behaviour at this instant is shown in Figure 3.9(f). A travelling wave (travelling wave 3) has been generated at the right hand container wall as a result of the excitation motion changing direction, moving from right to left.

Travelling wave 3 collides with the product of travelling waves 1 and 2, shown in Figure 3.9(g). This interaction results in a rapid decline in kinetic energy at $t = 2.10$ s. Following this event, a wave-to-wall interaction occurs at the right side of the container, transferring energy from kinetic to potential forms. As a result, the kinetic energy of the fluid is minimal at $t = 2.59$ s.

The wave-to-wall interaction generates a travelling wave (travelling wave 4) moving from right to left, and kinetic energy increases steadily. Travelling wave 4 is shown just prior to colliding with the left hand container wall at $t = 3.22$ s in Figure 3.9(h). This point in time corresponds to the fourth peak in kinetic energy in Figure 3.3(d). Shortly after a wave-to-wall interaction occurs, rapid decrease in kinetic energy ensues.

Formation of travelling waves causes severe deflections and breaking of the free surface with complex velocity patterns. A travelling wavefront has a discontinuous geometry, which is the product of steep velocity gradients. The wavefront is therefore the location of high shear stress, responsible for the viscous dissipation of kinetic energy.

In contrast to the 20 mm liquid depth case, 100 mm depth possesses a dominant standing wave form. Energy dissipation is poor as a result. Visualisations of 100 mm liquid depth in a 400 mm wide container are shown in Figure 3.10. As excitation commences from right to left, fluid rises at the right hand container wall, generating a travelling wave in the same direction, out of phase with the prescribed motion.

As the excitation slows and changes direction, fluid rises at the left hand wall. The travelling wave merges with the raised section of fluid, generating a breaking travelling wave of high elevation moving from left to right. In Figure 3.10(a), the formation of this travelling wave is shown at the left hand container wall at $t = 1.58$ s. This large free surface deformation corresponds to a low kinetic energy level, approaching the first trough seen in Figure 3.3(h).

The curling of the wave produces a section of fluid that separates from the main body. Then, this section free-falls, making contact again in the middle of the container. The free surface settles to an almost flat level, as shown in Figure 3.10(b), corresponding to the maximum kinetic energy, observed at $t = 1.82$ s. The free surface motion develops into periodic behaviour, exhibiting smaller free surface velocities than the 20 mm depth case. A standing wave is the mechanism with which energy is being transferred between kinetic and potential forms.

Kinetic energy decreases rapidly from this point. In Figure 3.10(c), the free surface shape is shown whilst the system is experiencing a steep rate of change, at $t = 1.95$ s. A standing wave is rising at the right hand container wall at this point in time. At $t = 2.07$ s, the peak free surface displacement is seen in Figure 3.10(d). The first trough in kinetic energy after the maximum is observed at this instant.

Figures 3.10(e) and 3.10(h) correspond to the 2nd ($t = 2.86$ s) and 25th ($t = 14.55$ s) peaks in kinetic energy history, respectively, after the maximum is observed in Figure 3.3(h). These instants in time correspond to close to flat free surfaces. In Figures 3.10(f) and 3.10(g), two of the wave-to-wall interactions are shown occurring at $t = 3.10$ s and $t = 5.68$ s. Large free surface deflections are seen at these instants, and kinetic energy is at a minimum.

As opposed to the discontinuous nature of the surface flow in shallow cases, motion observed in 100 mm depth assumes a periodic behaviour. Oscillation occurs between large free surface deformation (high potential energy) and relatively flat free surface shapes (high kinetic energy). This produces less complex surface velocity patterns of smaller magnitude. The inherent periodic motion of the standing wave inhibits the formation of travelling waves and wave-to-wave interactions, consequently restricting dissipation capabilities.

3.3.6 Tuning

The effects of tuning have been analysed at constant liquid depth of 20 mm. This depth has been chosen as the deepest level possessing a predominant travelling waveform, and therefore, its desirable energy dissipative qualities. Histories of kinetic energy for all cases simulated with a constant liquid depth of 20 mm are shown in Figure 3.11. Figures 3.11(a) to 3.11(h) correspond to container widths of 25, 50, 75, 100, 125, 150, 200 and 400 mm, in descending order. Positions indicated with a red arrow mark the point of maximum kinetic energy with the indicated magnitude.

Periodic behaviour is observed in all dissipation histories except for the 400 mm container width. This behaviour is most noticeable in container widths of and between 50 mm and 150 mm. Overall time taken to dissipate the total energy increases slightly between the container widths of 25 mm and 200 mm, a significant increase is seen between 200 mm and 400 mm container widths. Reducing the container width increases the number of wave-to-wall interactions that occur within a given time period, dissipation becomes faster as a result of this interaction.

Probability densities of the kinetic energy histories of all cases with a liquid depth of 20mm are shown in Figure 3.12. Figures 3.12(a) through to 3.12(h) correspond to container widths of 25, 50, 75, 100, 125, 150, 200 and 400 mm, in descending order. The case in Figure 3.12(a) spends around 95% of the total time in the very first bar, indicating the lowest possible energy level. As the container width increases the amount of undesirable mid-level energy rises marginally. The 125 mm case shown in Figure 3.12(e) exhibits a superior energy distribution than any wider container.

A summary of the settling time analysis of varying container width, employing a liquid depth of 20 mm is presented in Figure 3.13. The general trend shows that the settling time increases as the container width increases, due to decreasing number of wave-to-wall interactions. However, a trough in settling time magnitude is observed at 125 mm container width.

The maximum kinetic energy transferred from the excitation to the fluid for varying container widths, but for the constant liquid depth of 20 mm is shown in Figure 3.14. Optimal energy transfer occurs at the 125 mm container width, corresponding to a dip in settling time, shown in Figure 3.13.

Of the cases simulated, 20 mm of water in a 125 mm wide container possesses the most desirable energy transfer and dissipation characteristics. Hence, it is an optimal 2-D configuration when subjected to the above-mentioned excitation. A 3-D absorber arrangement would have a container length, and width of 125 mm in order to deal with bi-directional motion effectively.

It has been reported that the absorber mass to structure mass ratio should be at least 1/100 for the absorber to be effective, if the structure possesses more than 2 % (very light) damping (Banjeri at al., 2000). In order to reach this mass ratio, the above-mentioned geometry would need to be part of a much bigger, compartmentalized arrangement. For this reason, the number of these absorbers needed to effectively control a structure would depend entirely on its mass.

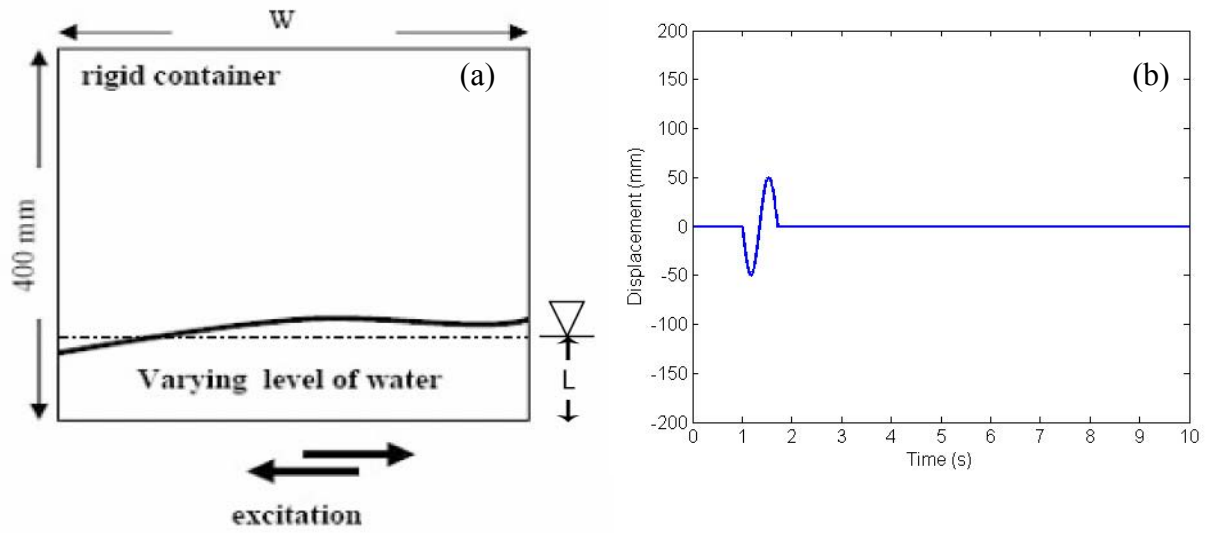
3.4 Conclusion

The primary form of energy dissipation in a sloshing liquid is due to shearing of the fluid. Shear stress is increased through providing steep velocity gradients. Two types of interactions are responsible for producing steep velocity gradients, namely, wave-to-wave and wave-to-wall interactions. Travelling waves have the ability to produce both of these interactions, whereas standing waves only produce wave-to-wall interactions.

A travelling wave front has a discontinuous geometry, which is the product of steep velocity gradients. The wave front is therefore the location of high shear stress, responsible for the dissipation of kinetic energy. A standing wave exhibits periodic behaviour, oscillating between large free surface deformation (high potential energy), and relatively flat free surface shapes (high kinetic energy). Less complex velocity patterns are produced of smaller magnitude.

Travelling waves are generated in shallow liquid levels up to and including 20 mm. As the liquid level increases, a transition to a standing waveform occurs. This transition produces undesirable energy dissipation characteristics resulting in an increase in settling times.

Therefore, employing a liquid depth higher than 20 mm in the container widths simulated is not recommended when subjected to the given excitation. An optimum energy transfer condition exists when varying container width, for a constant liquid depth of 20 mm. Of the cases simulated, this optimum condition occurs closest to the 125 mm container width



W: Container width
 L: Liquid depth

Figure 3.1. Showing (a) numerical model and (b) history of base excitation.

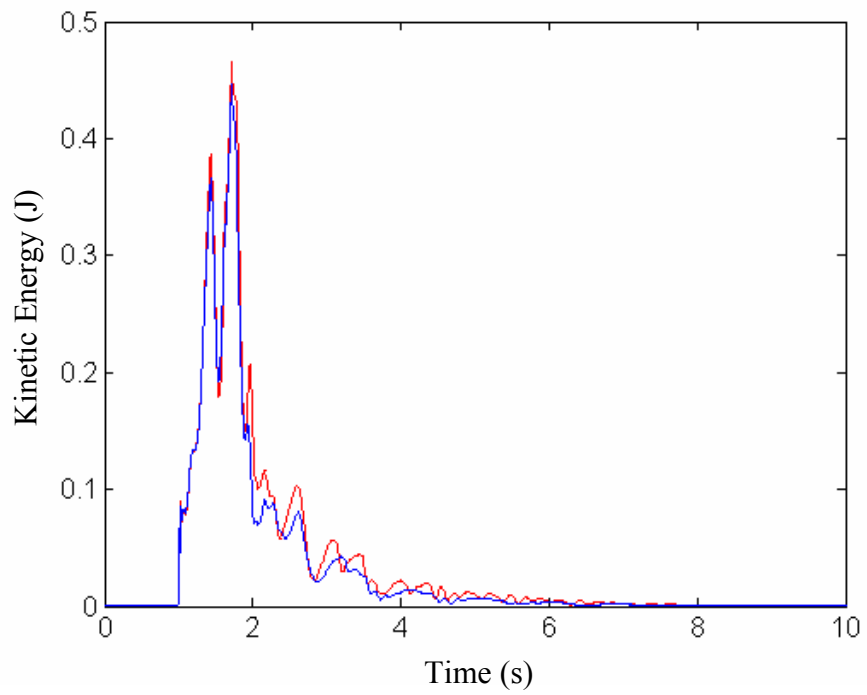


Figure 3.2. Comparison of kinetic energy histories, for 20 mm depth in a 400 mm wide container. Particle size of 0.5 mm x 0.5 mm (—) and 0.8 mm x 0.8 mm (—).

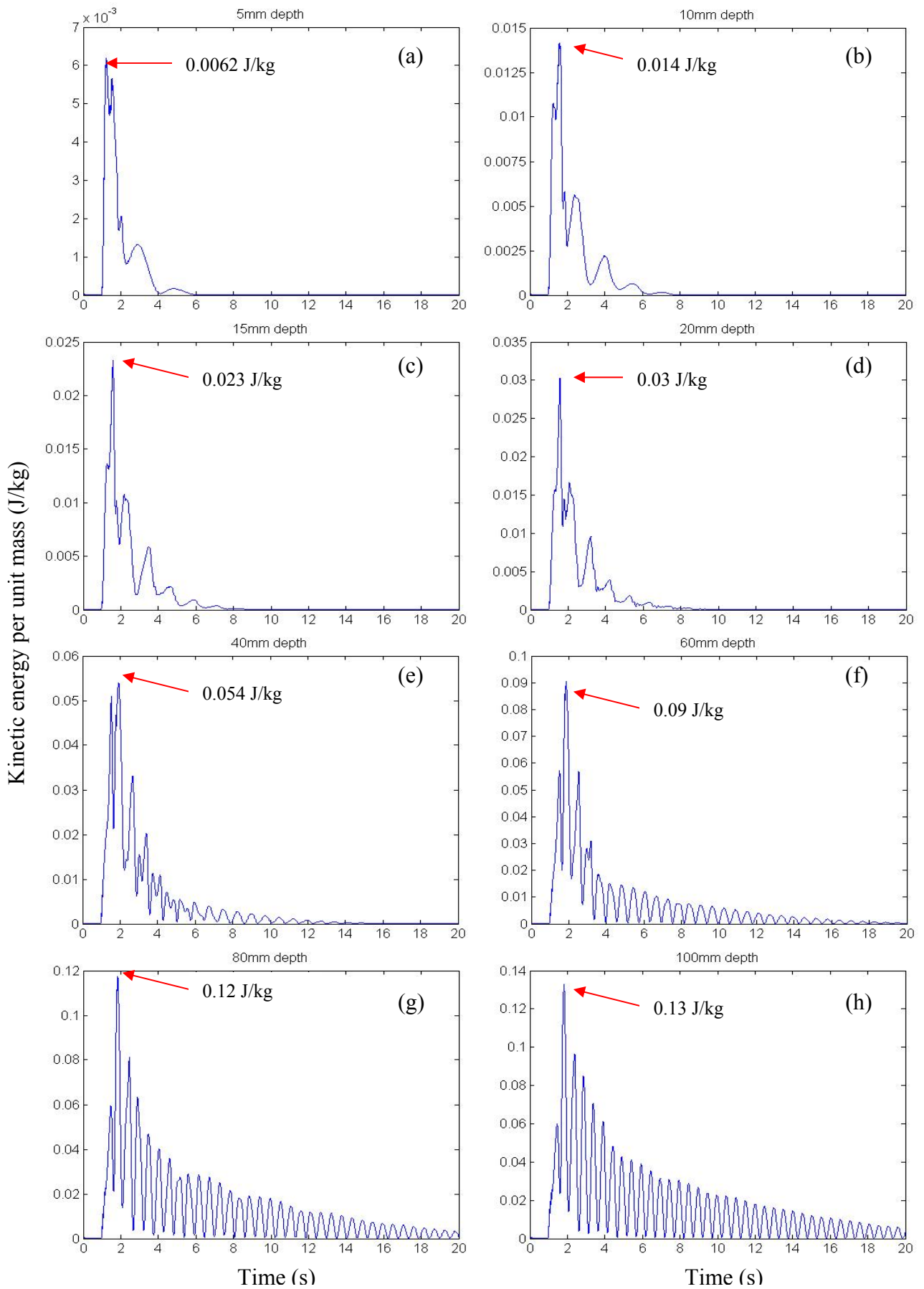


Figure 3.3. Kinetic energy dissipation histories for different water depths of (a) 5 mm, (b) 10 mm, (c) 15 mm, (d) 20 mm, (e) 40 mm, (f) 60 mm, (g) 80 mm and (h) 100 mm. Constant container width of 400 mm. Note y-axis values vary significantly.

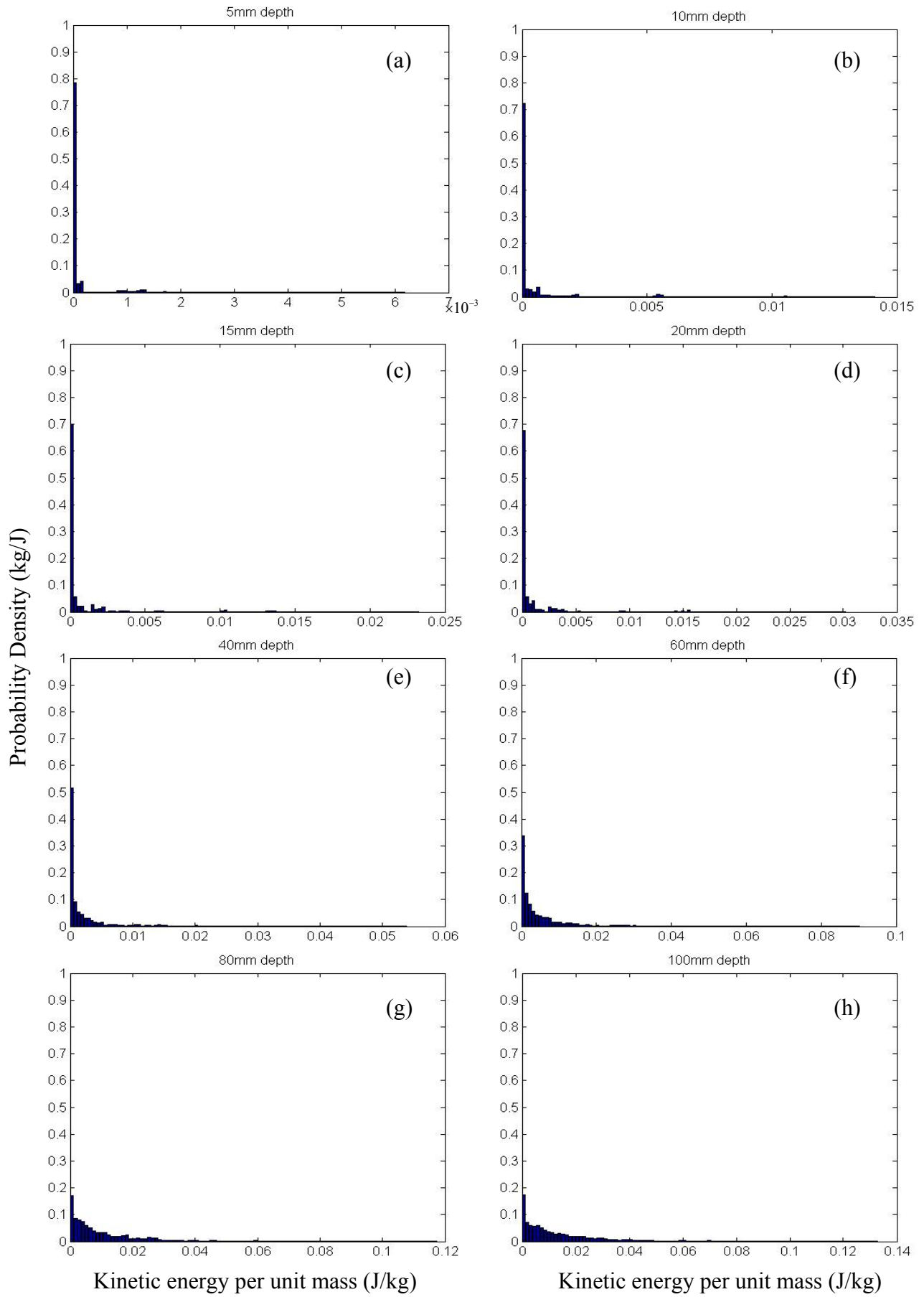


Figure 3.4. Probability densities of kinetic energy shown in Figure 3.3.

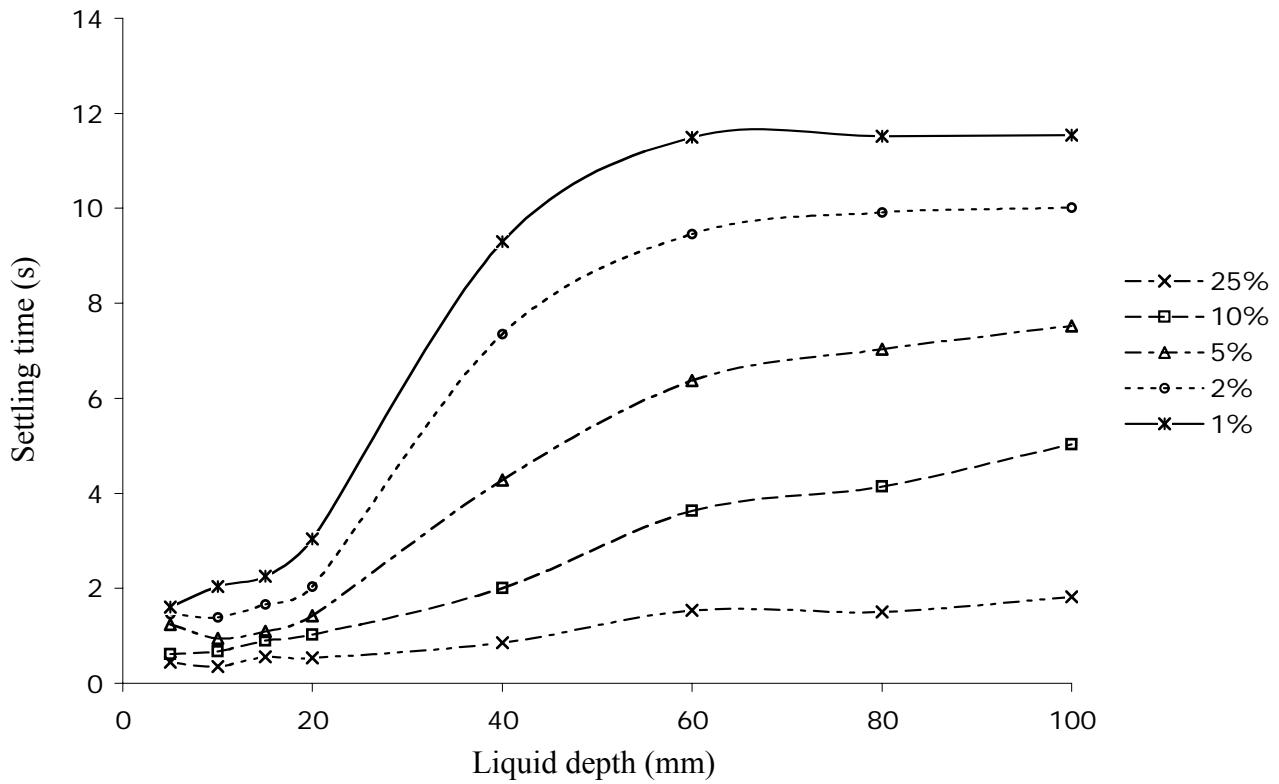


Figure 3.5. A summary of settling times for different water depths with a constant container width of 200 mm. The legend is for the level of residual energy as a percentage of the maximum.

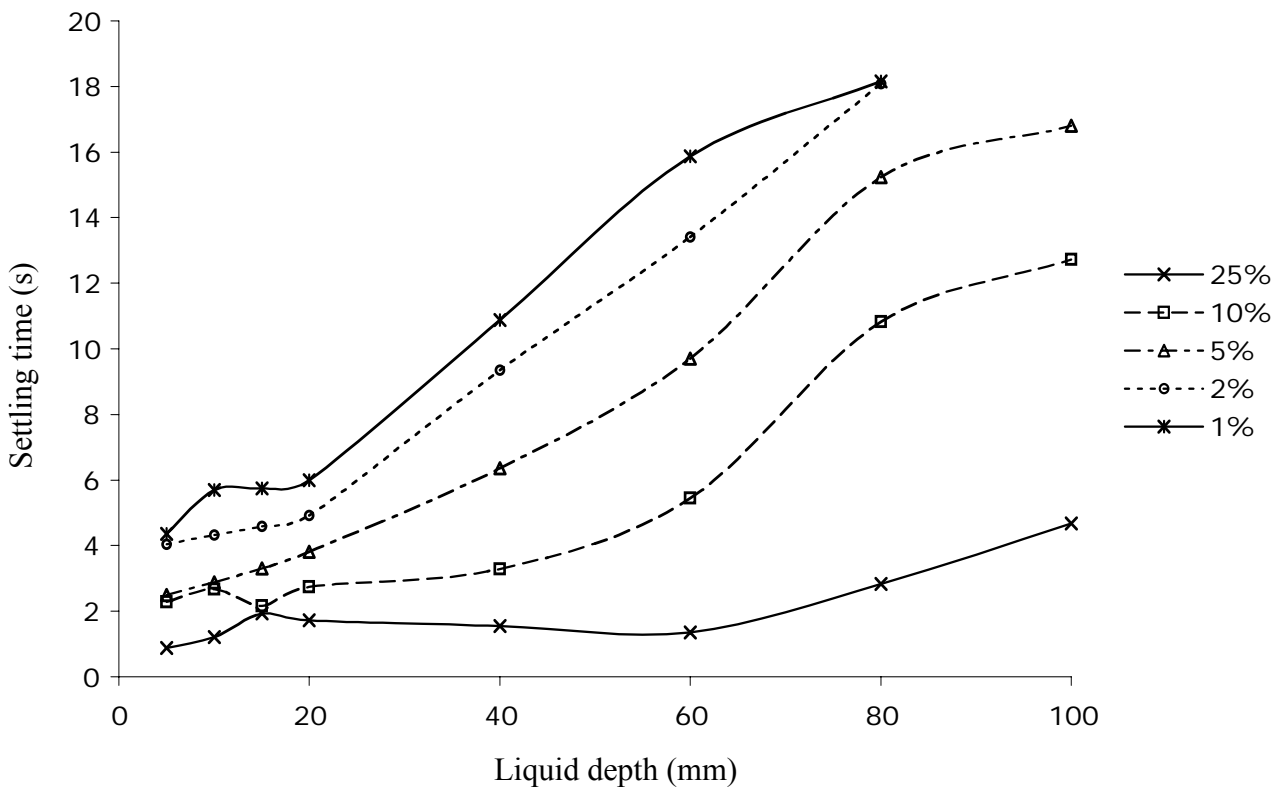


Figure 3.6. A summary of settling times for different water depths. Constant container width of 400 mm. The legend is for the level of residual energy as a percentage of the maximum.

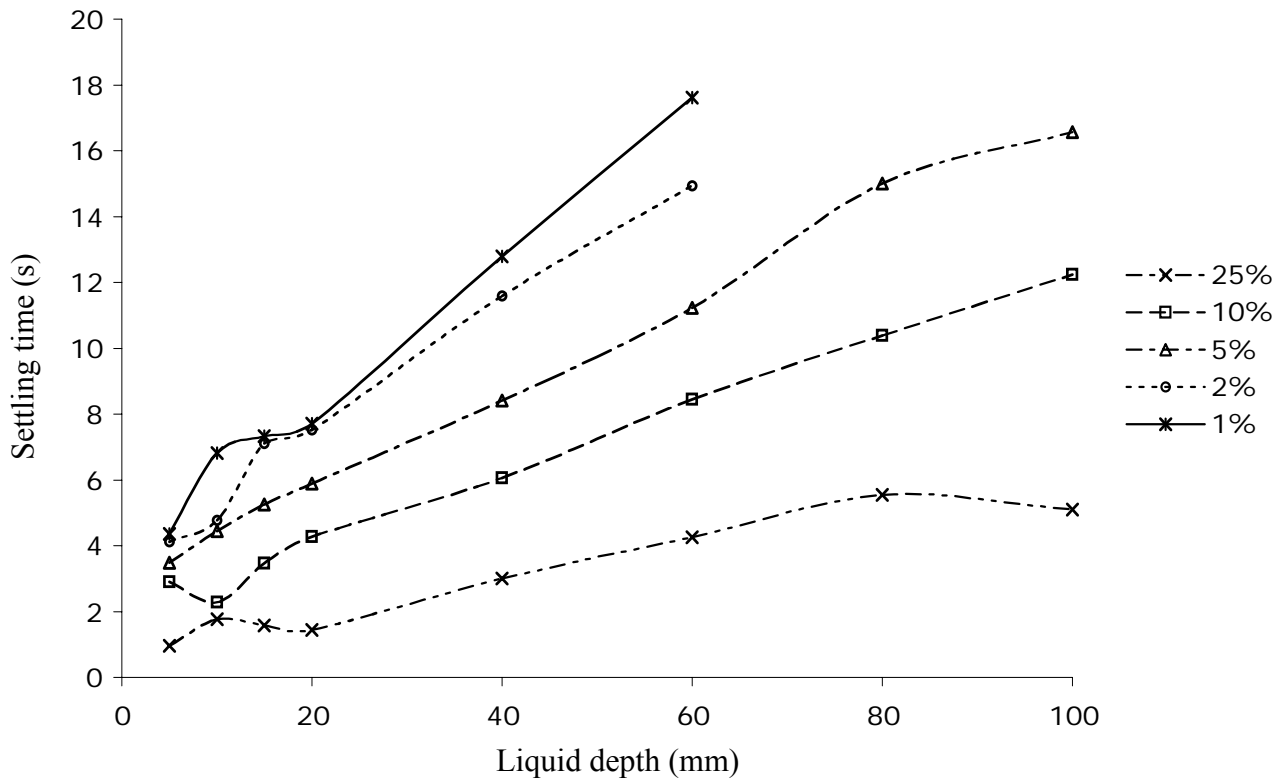


Figure 3.7. A summary of settling times for different water depths. Constant container width of 600 mm. The legend is for the level of residual energy as a percentage of the maximum.

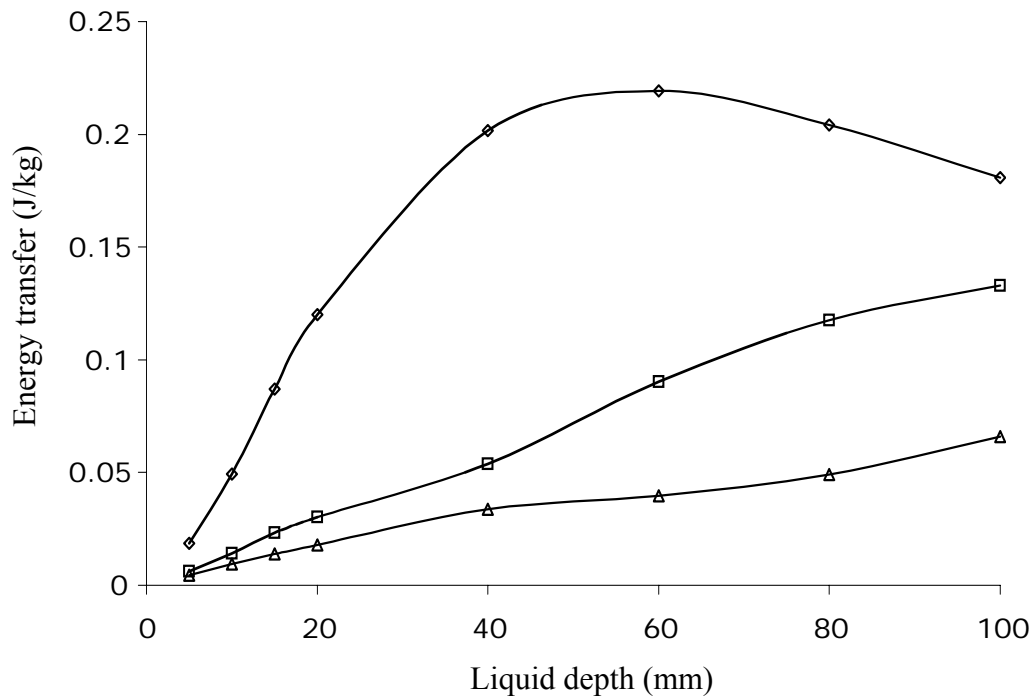


Figure 3.8. Maximum energy transferred from base excitation to the working fluid per unit mass of fluid for container widths of 200 mm (\diamond), 400 mm (\square) and 600 mm (Δ), implementing liquid depths of 5 mm, 10 mm, 15 mm, 20 mm, 40 mm, 60 mm, 80 mm and 100 mm.

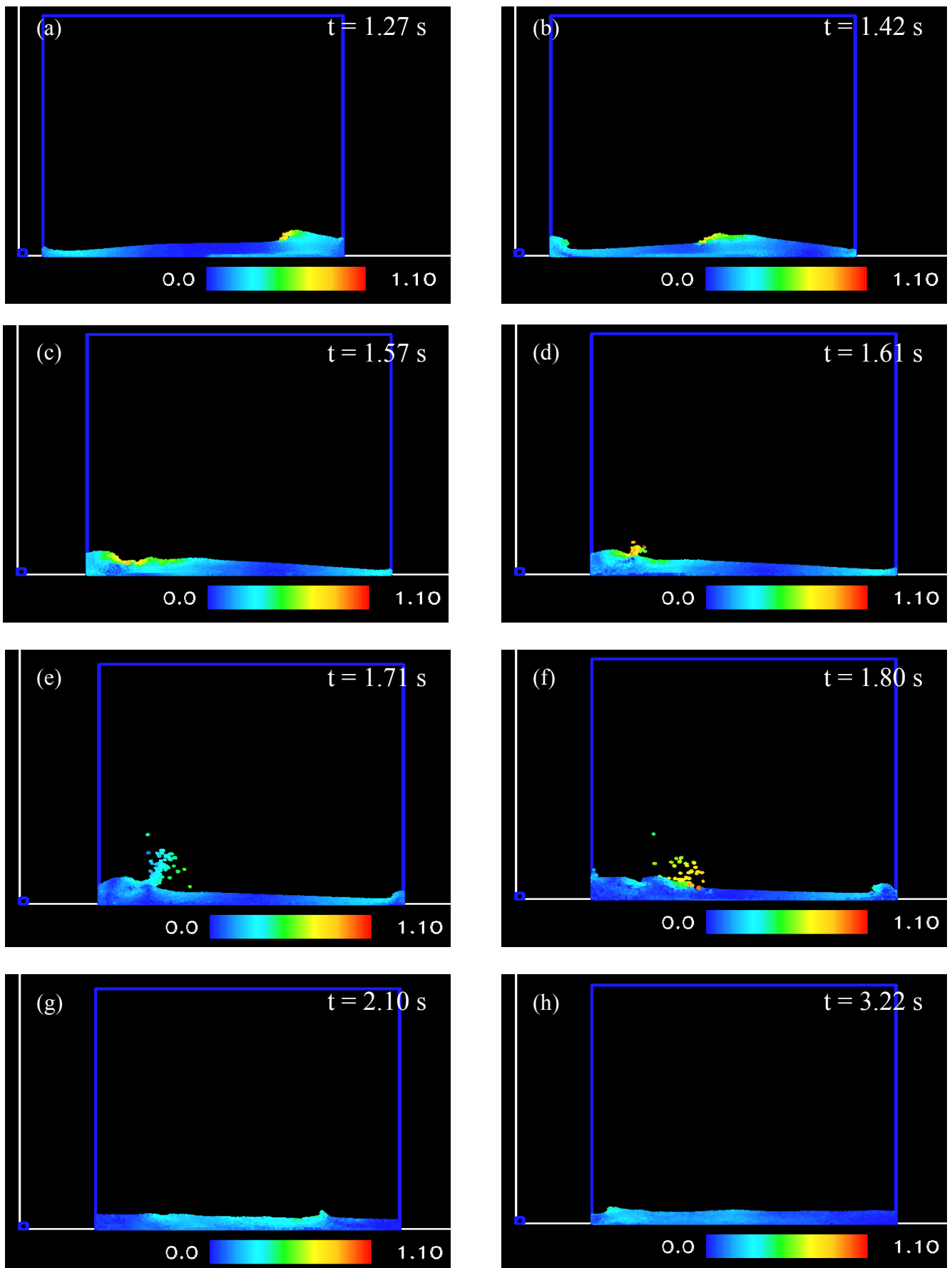


Figure 3.9. Still frames at instants of interest for 20 mm liquid depth and 400 mm wide container. The fixed velocity scale is from 0 to 1.1 metres per second.

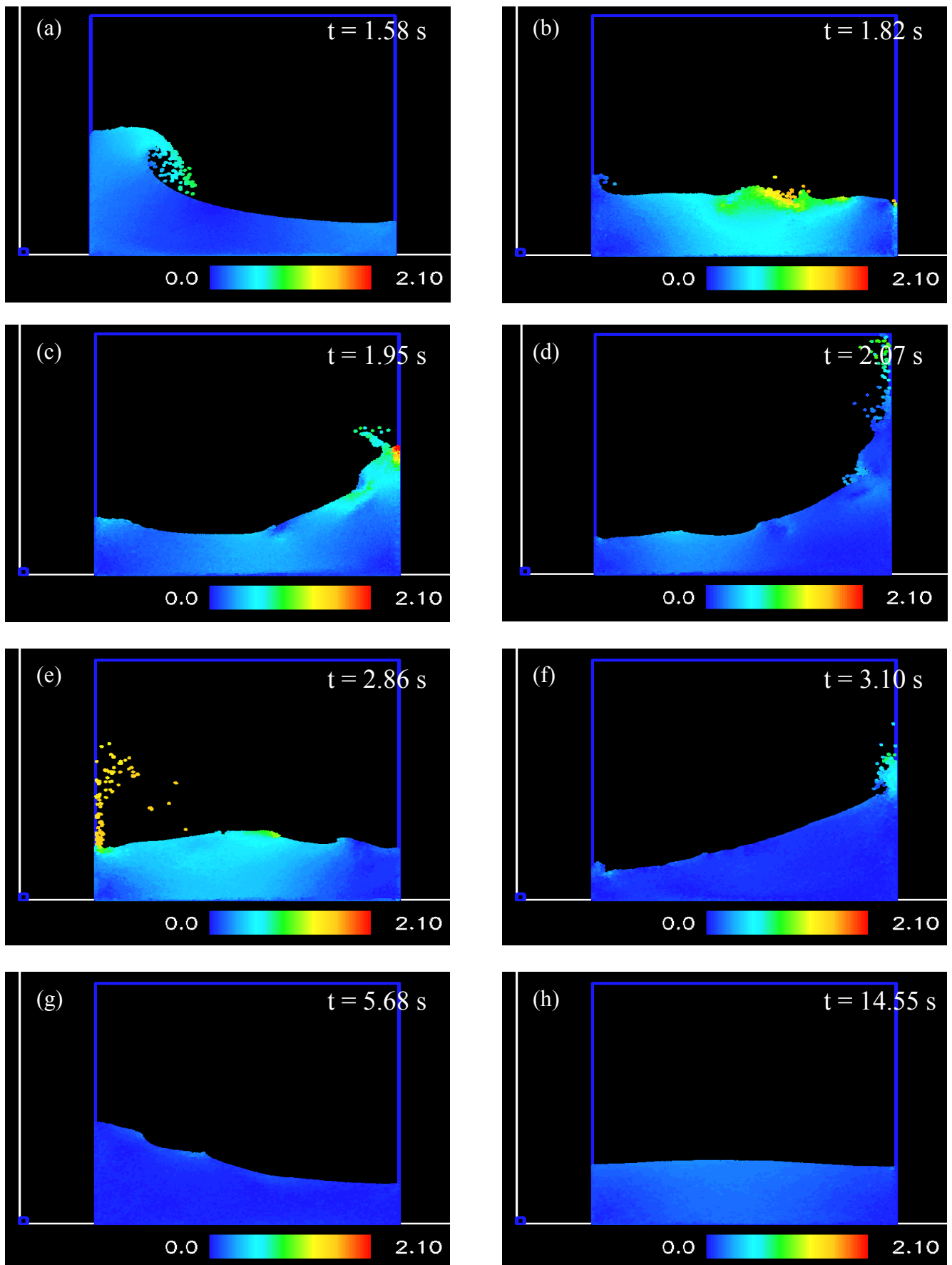


Figure 3.10. Still frames at instants of interest for 100 mm liquid depth and 400 mm wide container. The fixed velocity scale is from 0 to 2.1 metres per second.

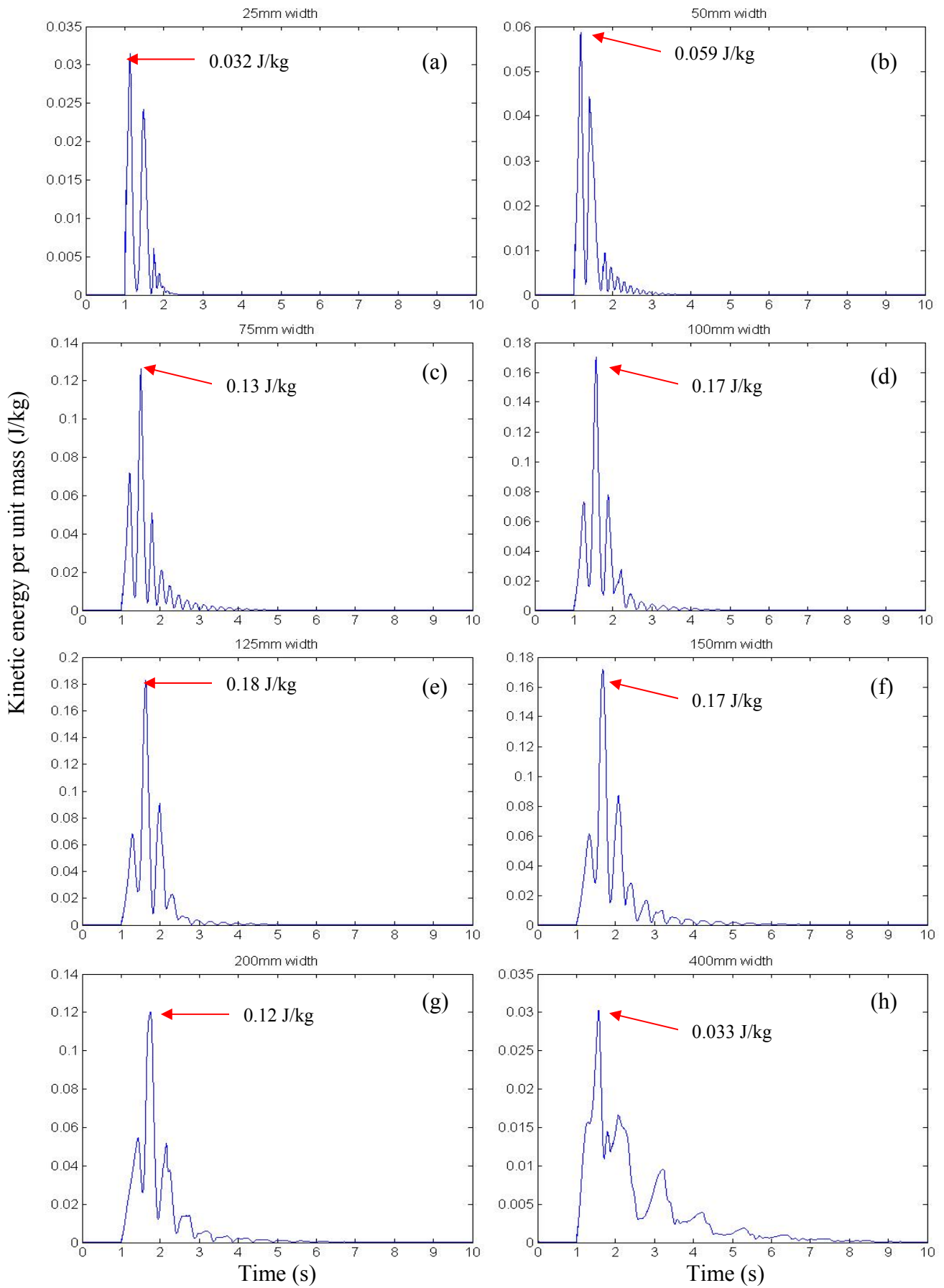


Figure 3.11. Kinetic energy dissipation histories for different container widths of (a) 25 mm, (b) 50 mm, (c) 75 mm, (d) 100 mm, (e) 125 mm, (f) 150 mm, (g) 200 mm and (h) 400 mm. Constant water depth of 20 mm. The y-axis amplitude values vary significantly.

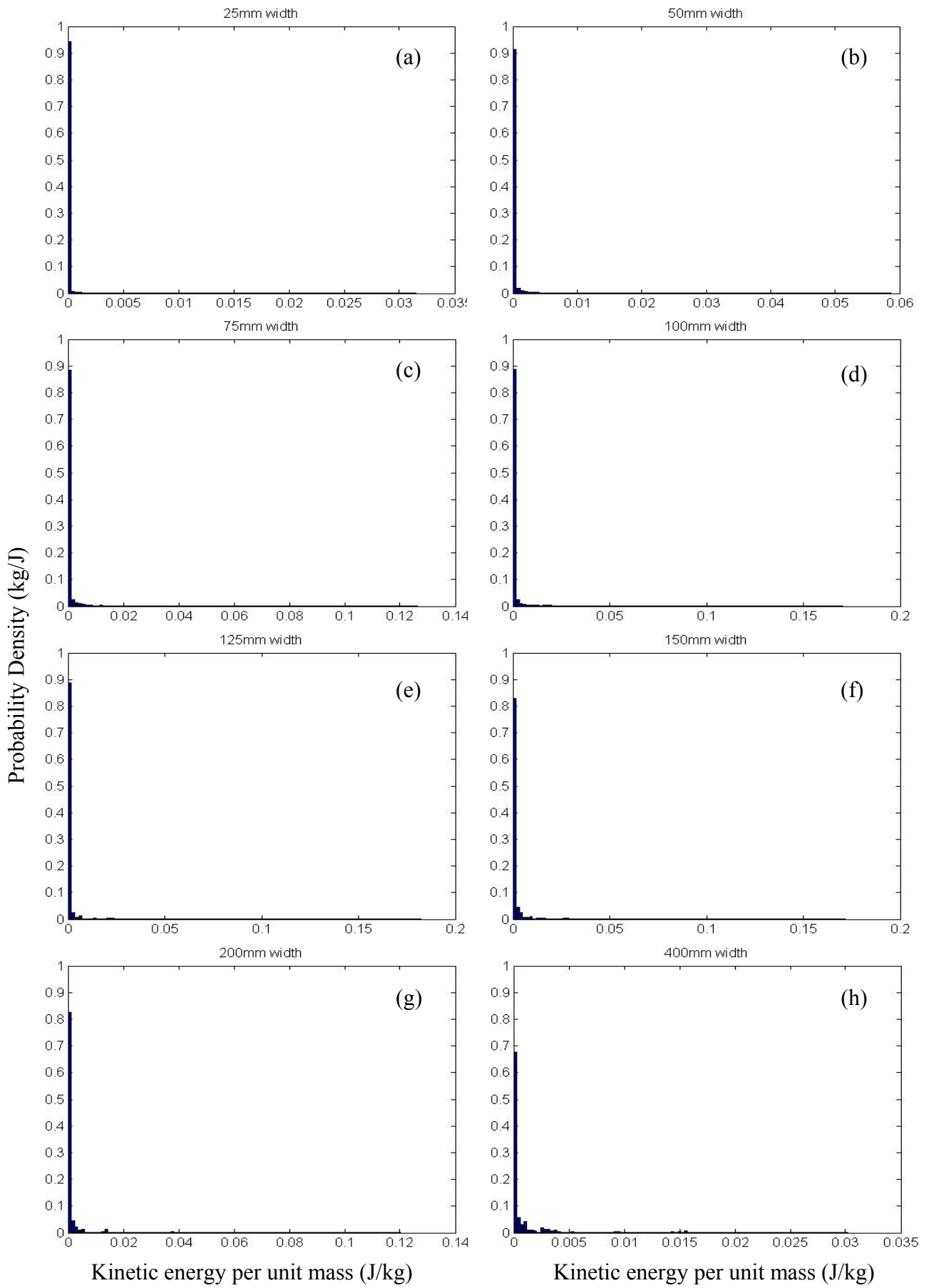


Figure 3.12. Probability densities of the kinetic energy shown in Figure 3.11.

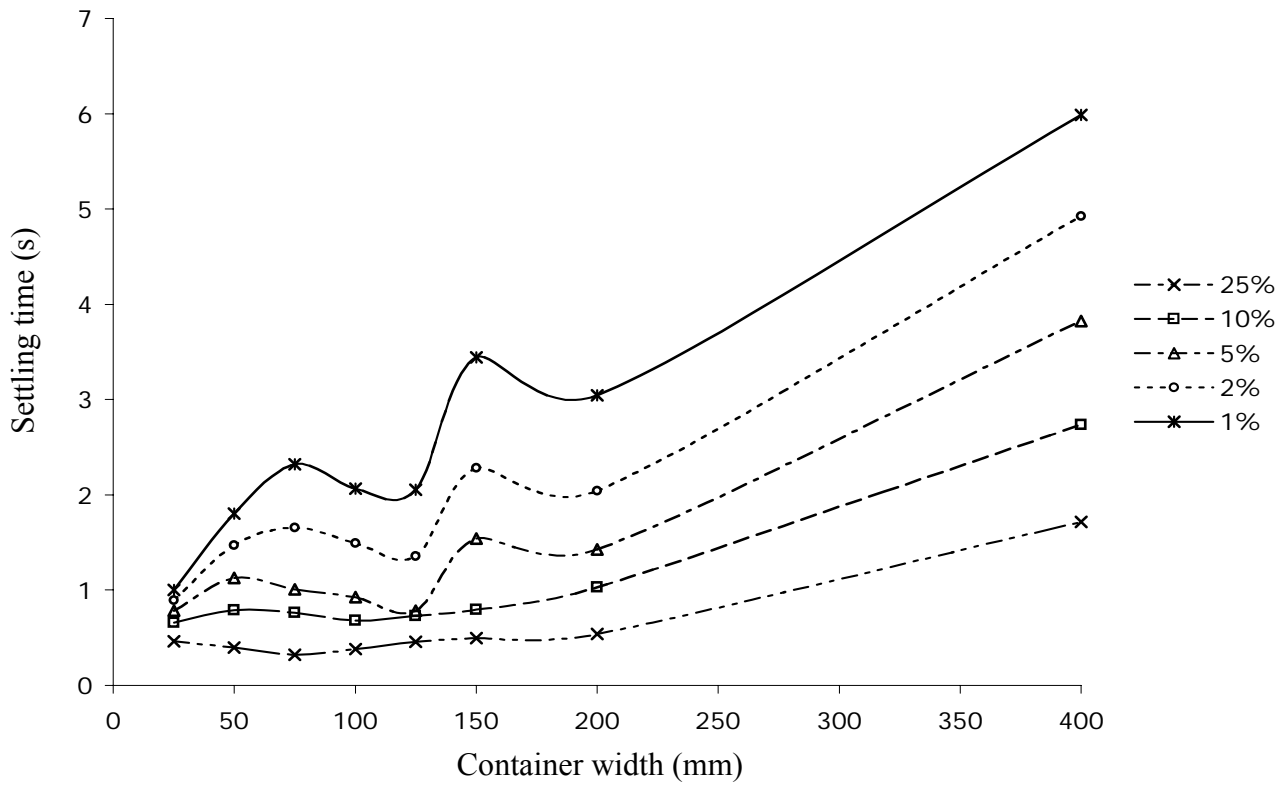


Figure 3.13. A summary of settling times for different container widths with a constant liquid depth of 20 mm. Legend indicates the level of residual energy as a percentage of the maximum.

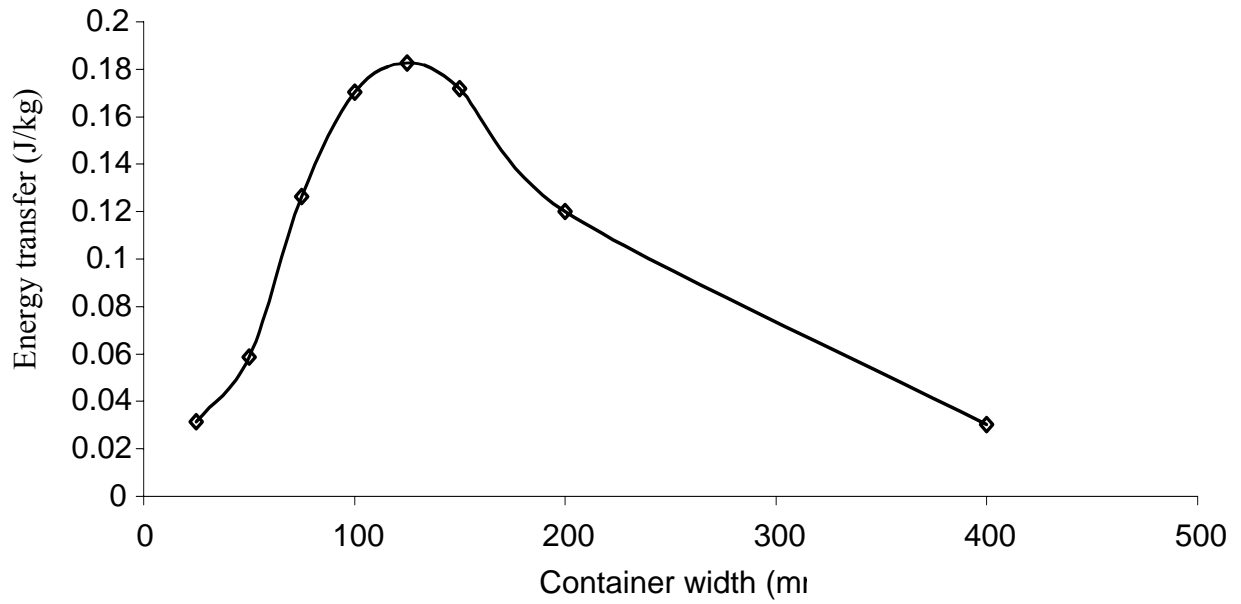


Figure 3.14. The maximum kinetic energy transferred for different container widths. Constant water depth of 20 mm.

Chapter 4

PREDICTING THE DYNAMIC STRUCTURAL RESPONSE CONTROLLED BY A SLOSHING ABSORBER USING SPH

4.1 Introduction

In the previous chapters, SPH has been used to predict the fluid behaviour within a sloshing absorber experiencing imposed motion. The objective of this chapter is to demonstrate the broader ability of this technique to reliably predict the dynamic motion of a structure/sloshing absorber system, and the inherent fluid-structure interaction forces produced. When tuned properly, these interaction forces generate the required control of excessive structural oscillations.

Simple experiments are described, involving an inverted pendulum controlled by a sloshing absorber. A series of shallow liquid levels are investigated to generate travelling free surface waves. An ideal depth range is identified. The numerical predictions of structural motion and fluid free surface shapes obtained with SPH are compared within those observed experimentally. A study is presented identifying the effects of varying the SPH smoothing length on the energy dissipation characteristics of the fluid. The same SPH code has been used here as that in chapter 2.

4.2 Experimental procedure

The experimental set-up used in this work is similar to that in Chapter 2. As shown in Figure 4.1, it consists of a structure configured as an inverted pendulum. A container made of Perspex, having similar dimensions (340 mm x 230 mm x 180 mm), has replaced the food container used for the sloshing absorber. The Perspex container is heavier than the container used in Chapter 2, increasing the weight of the structure. To compensate for the additional weight, stiffer springs are now used to support the structure.

The natural frequency and equivalent viscous damping ratio of the uncontrolled structure are $0.5 \text{ Hz} \pm 0.02$ and $0.9 \% \pm 0.1$, respectively. The sloshing absorber is tuned to this frequency when a depth of $\sim 12 \text{ mm}$ is employed (Milne-Thomson, 1968). However, this process of tuning is not able to take into account the effect of free surface discontinuities, as discussed further in Section 4.4.2.

The container has been changed to minimise the 3 dimensional effects caused by the rounded edges of the food container, by introducing a completely square geometry. As in Chapter 2, the container is mounted on the pendulum, 670 mm above the pivot point. Hence, as the structure is excited, the container is subject to angular oscillations.

The mass moment of inertia of the uncontrolled structure is measured to be approximately 3.4 kg.m^2 about the centre of rotation. The ratios of mass moment of inertia of fluid to that of the structure for the above-mentioned liquid depths are about $1/34$ (2.75 mm), $1/17$ (5.5 mm), $1/11$ (8.25 mm), $1/9$ (11 mm) and $1/4$ (22 mm). The ratios of fluid mass to structure mass for these liquid depths are about $1/80$ (2.75 mm), $1/40$ (5.5 mm), $1/27$ (8.25 mm), $1/20$ (11 mm) and $1/10$ (22 mm).

The disturbance is provided in the same way, from an initial angular displacement of 16 degrees (the structure is shown in this position by the dashed lines in Figure 4.1). A simple stop-block allows consistent initial conditions for all cases. The structure is released from its initial position and allowed to oscillate freely. Experimental observations are video recorded with a standard digital camera at a frame speed of 30 frames per second. A higher frame speed than that used in Chapter 2 is needed due to the increased natural frequency of the structure, from 0.3 Hz to 0.5 Hz. Experimentally recorded structure motion is accurate to within $\pm 0.033 \text{ s}$ and ± 1 degree.

4.3 Numerical Model

The structure and sloshing absorber system is represented by a rigid boundary, having the same dimensions as the experimental setup. The structure's motion is restricted to dynamic rotation about its pivot point. Tethers are attached, representing the structure's stiffness, and mechanical damping due to friction. The stiffness and damping of the tethers are chosen to replicate the experimentally observed structure motion. The sloshing fluid is water with a density of 1000 kg.m^{-3} and dynamic viscosity of 0.001 Pa.s .

A particle size of $0.5 \text{ mm} \times 0.5 \text{ mm}$ has been found to be fine enough to model the boundary and fluid, for depths as shallow as 5.5 mm (Chapter 2 and Appendix 2). For the depth of 2.75 mm , a boundary and fluid particle size of $0.25 \text{ mm} \times 0.25 \text{ mm}$ has been used. This produces a discretized fluid volume 11 particles deep, the same number as for the 5.5 mm depth case, with a particle size of $0.5 \text{ mm} \times 0.5 \text{ mm}$. Time stepping is explicit and is limited by the Courant condition modified for the presence of viscosity, given in Appendix 1, Equation A15.

To replicate the experimental conditions, the structure/absorber system is given an initial displacement of 16 degrees clockwise, storing potential energy in the tethers. As in chapter 2, the fluid is allowed to settle for 4 seconds in this position until the liquid velocity approaches 0 m/s . The structure is then released responding dynamically, its motion exciting the liquid within. Structural motion ceases due to the damping of the attached tethers, and the additional control of the working fluid.

4.4 Liquid Sloshing and Structural Response

4.4.1 Displacement History

The observed angular displacement history of the structure is compared to the SPH prediction of the uncontrolled case, along with the 2.75 mm, 5.5 mm, 8.25 mm, 11 mm, and 22 mm liquid depth cases. These comparisons are shown in Figures 4.2(a) to 4.2(f). In the figures, the horizontal axis is time normalised by the undamped natural period of oscillation (T_n). As in Chapters 2 and 3, the boundary is constructed of a single layer of particles for the numerical predictions. These particles exert a force of the Lennard-Jones form on the fluid particles in the normal direction (Monaghan, 1994). A smoothing length of 1.2 times the particle separation is used. The smoothing length defines the size of the integration domain. The smoothing length is described further in Appendix 1.

For the uncontrolled structure, experimental data is recorded for the first 10.5 cycles only. This data is then compared to the SPH prediction of the uncontrolled case, to verify the accurate selection of structural damping, stiffness, and inertia used in Equation A.21. As shown in Figure 4.2(a), the SPH prediction of the uncontrolled structure's motion is an exact match to that seen experimentally. The quality of prediction when the structure is controlled varies with liquid depth. However, a good representation is obtained when fluid behaviour is 'dynamic'. These instances are typically seen when the structure is experiencing large displacements and for shallow liquid levels. For depths of 2.75 mm and 5.5 mm, presented in Figures 4.2(b) and 4.2(c), dynamic behaviour is observed almost all the time. As liquid depth increases from 8.25 mm to 22 mm, in Figures 4.2(d) to 4.2(f), dynamic fluid behaviour is observed less often.

Whilst fluid behaviour is dynamic, predicted peak amplitudes and the frequency of structural oscillation are close to those observed experimentally. As structural displacements become small (less than about 6 degrees), the fluid behaviour becomes less dynamic. At these instances, more energy dissipation is predicted than observed experimentally. As a result, predicted peak displacements are smaller than those observed for all liquid depths.

At the depths of 8.25 mm and higher, enough excess energy dissipation is predicted to affect the structure's damped frequency, ω_d . As indicated in Equation (3) below, as ζ_{eq} increases ω_d decreases.

$$\omega_d = \omega_n \sqrt{1 - \zeta_{eq}^2} \quad (3)$$

Where ω_n is the undamped natural frequency of the structure, and ζ_{eq} is the structural damping caused by energy dissipation within the fluid.

This results in the developing phase difference between the predicted and experimentally observed structural displacement histories in Figures 4.2(d), 4.2(e) and 4.2(f). However, even with this difficulty, SPH provides a good representation of the structure's behaviour when controlled at all liquid depths. Efforts focused on correcting ζ_{eq} are presented in Section 4.4.4.

4.4.2 Settling Times

A summary of experimental settling times is shown in Figure 4.3(a) for the structure controlled by the sloshing absorber with varying liquid depths. Here, settling time is defined as the time taken from the structure's release to when its motion has ceased, residing in the central rest position. Cases employing all levels of liquid studied here produce a considerable reduction in the settling time, relative to the uncontrolled case (liquid depth of zero).

Settling time is shortest (about 12 s) when employing a liquid depth of either 5.5 mm or 8.25 mm. In fact, settling time is largely insensitive to the amount of fluid within the absorber between depths of 2.75 mm and 11 mm. At all these depths, the travelling waveform is dominant. At 22 mm of depth, standing waves are observed. As a result, settling time increases significantly.

Optimum performance of the sloshing absorber occurs at a depth shallower than that of the tuned case (~12 mm). At these shallow depths, there are extreme discontinuities in the flow field. Steep velocity gradients occur as a result, producing large amounts of shear stress and inherent energy dissipation. Therefore, it seems more important to select a liquid depth that maximises energy dissipation, as opposed to one that tunes the sloshing frequency to that of structure's frequency.

A comparison of settling times between the SPH predictions and experimental data is shown in Figures 4.3(b) to 4.3(f) for liquid depths of 2.75 mm, 5.5 mm, 8.25 mm, 11 mm and 22 mm, respectively. Here, settling time is defined as the time taken from the instant of the structure's release to when it reaches a certain percentage of its initial rotation. This percentage is indicated on the horizontal axis in these figures. The vertical axis represents settling time in seconds. The accuracy of experimentally recorded settling time is related to the roll angle of the structure. This angle is measured by analysing the experimental video frame by frame, then tracing the structure arm position onto transparencies. The subsequent angle is then taken from the transparencies. The error in experimental measurement is expected to be around ± 1 second and is indicated in the figure with error bars. It can be seen that SPH provides an accurate estimate of settling time for all liquid depths, at all levels of residual displacement.

4.4.3 Free Surface Comparison

Free surface comparisons at a liquid depth of 2.75 mm are shown in Figure 4.4. This depth is the shallowest, and therefore, it is the most difficult case to obtain an accurate prediction of the free surface. For this reason, it has been chosen as a representative case, to illustrate the ability of SPH to capture the fluid behaviour within the container. Free surface comparisons at all other liquid depths are shown in Appendix 5, but are not described here in the text, due to providing little additional understanding for the reader.

In Figure 4.4, the left hand column represents experimental observations at certain instants in time, and the numerical predictions are shown in the right hand column. Figures 4.4(a) and (b), (c) and (d), (e) and (f), (g) and (h), (i) and (j), and (k) and (l) correspond to times of 1.00 s, 1.13 s, 1.60 s, 2.13 s, 3.23 s, and 4.70 s, respectively, from the instant of release. These nominated instances are chosen either as points of reference (when the structure is in the central rest position, or at maximum angular displacement), or at points in time where fluid behaviour is exceptionally interesting.

At the instant of its release, the structure's motion commences from right to left. At $t = 1.00$ s, the travelling wavefront shown in Figure 4.4(a) has impacted on the left wall, causing a wave-to-wall interaction. The predicted wavefront reaches the container wall prior to this instant, resulting in a small phase difference between experimental and numerical fluid flow of ~ 0.02 s.

High wavefront velocity causes a hydraulic jump with a maximum height recorded at $t = 1.13$ s. This instant is shown in Figure 4.4(c). Hydraulic jump behaviour is predicted well, however the initial phase difference between the experimental and numerical fluid behaviours is noticeable still in comparing Figure 4.4(c) with 4.4(d). Fluid has begun to fall under gravity already in Figure 4.4(d). The structure passes through the central rest position shortly after at $t = 1.60$ s. Fluid is distributed over around three fifths of the container bottom at this instant, as shown in Figure 4.4(e). The predicted fluid free surface length is smaller than that observed.

The wave to wall interaction that follows, at the right side of the container, is shown in Figure 4.4(g). Peak rotation is also observed at this instant. Fluid distribution is predicted well in Figure 4.4(h). However, the predicted hydraulic jump height is marginally smaller than that observed.

The motion commences again from right to left, causing the wave-to-wall interaction shown in Figure 4.4(i), at $t = 3.23$ s. Severe mixing and air entrainment are observed at this instant. Although the details of this behaviour cannot be captured, possibly due to the lack of a turbulence model, fluid distribution is predicted well. Swirling motion is forecast throughout this event, as shown in Figure 4.4(j). The structure again passes through the central rest position during the third cycle of structural oscillation, shown in Figure 4.4(k). The fluid is observed to be covering around one half of the container bottom at this instant. The predicted free surface in Figure 4.4(l), is similar to that observed. The phase difference between the experimental and numerical fluid behaviours has now closed.

At the depth of 2.75 mm, SPH provides a close representation of the fluid free surface behaviour within the absorber. Some observed local fluid behaviour is not replicated exactly, particularly during energetic hydraulic jumps. During such events, it is not uncommon to observe significant swirling of the fluid. Overall fluid distribution is accurately predicted at all instances. This overall behaviour seems to be more important than local detail, due to the pressure force exerted on the structure by the fluid being an integral quantity. As a result, the structure's motion is relatively insensitive to the small scale details of the free surface.

The accuracy of free surface shape predictions increases with liquid depth, similar to the forced motion cases presented in Chapter 2. However, due to excessive energy dissipation being predicted by SPH in full interaction cases, a phase difference develops between the predicted and observed structural motion when controlled by depths of 8.25 mm and higher. This makes presenting a ‘fair’ free surface comparison over time difficult at these depths.

4.4.4 Correcting ζ_{eq}

The effects of changing the treatment of the boundary from a Lennard-Jones type force to a gradient of kernel approximation are presented next. These two forms of boundary treatment are described in Appendix 1. It is expected that the change in boundary treatment can provide some correction to ζ_{eq} due to eliminating much of the noise produced by the Lennard-Jones boundary approximation (see Appendix 1).

The same analysis as in Figure 4.2 is shown for a gradient of kernel boundary approximation in Figure 4.5. The uncontrolled case, along with the 2.75 mm, 5.5 mm, 8.25 mm, 11 mm and 22 mm liquid depths is shown in Figures 4.5(a) to 4.5(f) respectively. Here, the boundary consists of 5 layers of particles, as opposed to the single layer of particles needed for the Lennard-Jones approximation described in Appendix 1. These boundary particles are included in the summations for the fluid particles.

No significant difference in structural behaviour is seen when the treatment of the boundary is changed. The structural displacement histories obtained in Figure 4.5 are almost identical to those in Figure 4.2. At the liquid depths of 2.75 mm and 5.5 mm, both methods of boundary force formulation produce acceptable predictions of the structural motion.

When using a gradient of kernel boundary approximation, the SPH smoothing length can be increased. This has been done at the depths of 8.25 mm and higher, in order to reduce the amount of energy dissipation within the fluid. In SPH, smoothing length defines the area of the support (integration) domain. The particle approximations used by the method depend on having a sufficient number of particles within this area. If the smoothing length is too small, there may not be enough number of particles to exert force on the particle of interest. On the other hand, if the smoothing length is too large, local details of the flow are smoothed out. Both of these outcomes result in low accuracy (Liu and Liu, 2003).

Therefore, the desired value of smoothing length is one that identifies a sufficient number of neighbouring particles, without smoothing significant detail from the free surface. Dynamically evolving smoothing length to maintain a constant number of neighbours is expected to be of significant advantage by the authors. However, the effects of dynamically evolving smoothing length are not investigated in this study.

The experimentally observed angular displacement history of the structure is compared to the SPH prediction when controlled with 8.25 mm of liquid in Figure 4.6. For the SPH predictions, smoothing lengths of (a) 1.2, (b) 2.4, (c) 3.6 and (d) 4.8 times the particle separation (psep) are used. The particle separation is the distance between the centres of two neighbouring particles. This distance is equal to the particle length in one direction (Appendix 1). As stated in Chapter 2 and Appendix 1, a smoothing length of 1.2 x psep is generally used when modelling free surface flows. Higher values are introduced here. Peak displacement amplitudes increase with smoothing length. In addition, the phase difference developing between experimental data and the SPH prediction becomes less severe. An increasing number of small amplitude oscillations are also predicted. These are not observed. However, they may not be unreasonable due to the amplitude being so small (≤ 1 degree) that they are unable to be recorded experimentally.

The same analysis as in Figure 4.6 is shown for the structure when controlled with 11 mm of liquid in Figure 4.7. Similar observations are made here, as those for 8.25 mm of depth. Predicted peak displacement amplitudes approach those of the experiment as smoothing length increases from 1.2 to 3.6 x psep in Figures 4.7(a) to 4.7(c). The phase difference developing between experimental data and the SPH prediction closes at a smoothing length of 2.4 x psep as presented in Figure 4.7(b). For the benefit of structural frequency alone, no further increase in smoothing length is required. This result suggests that a good number of neighbouring particles are found within the support domain when using a smoothing length of 2.4 x psep.

The same analysis as in Figure 4.7 is shown for the structure when controlled with 22 mm of liquid in Figure 4.8. As in 11 mm depth, the peak displacement amplitudes increase with smoothing length, up to a value of $3.6 \times p_{sep}$, as shown in Figures 4.8(a) to 4.8(c). Increasing smoothing length further to $4.8 \times p_{sep}$ causes peak displacements to drop in amplitude, in Figure 4.8(d). At this high value, significant local information is smoothed out, resulting in low accuracy.

The damped frequency of the structure increases with smoothing length. For a value of $1.2 \times p_{sep}$, the predicted structural motion lags behind that observed by one half of a cycle, after 10 cycles in Figure 4.8(a). For a value of $2.4 \times p_{sep}$, predicted structural motion leads that observed by one third of a cycle, after 10 cycles in Figure 4.8(b). As smoothing length is increased further, the phase difference advances. The ideal smoothing length for 22 mm of liquid depth, is therefore somewhere in between 1.2 and $2.4 \times p_{sep}$.

4.4.5 Summary results for computational smoothing length

At shallow depths, the SPH wavefront may be only very few particles deep. As a result, approximations for the particles in and near the wavefront can be averaged over an insufficient number of neighbours. Inaccurate field variable magnitudes can be calculated as a result. When this is the case, the system responds positively to an increase in smoothing length.

With deeper liquid levels, more neighbours are found within the support domain. Therefore, smaller smoothing lengths can be used to obtain the same level of accuracy. At the depth of 11 mm, an increase beyond $2.4 \times \text{psep}$ provides no further increase in accuracy. At the depth of 22 mm, doing so has a detrimental effect on the accuracy of prediction. The number of neighbours becomes too high, smoothing out significant local information. Such an effect is noticed when the standing waveform is dominant, from the fourth cycle onwards, in Figure 4.8.

If one smoothing length were to be used for all liquid depths, to optimise the accuracy of the predicted structural response, a value of $2.4 \times \text{psep}$ could be chosen. However, another primary concern is the method's ability to accurately describe local fluid behaviour when smoothing length is increased. The effect that this has on the free surface is described next, for the depths of 8.25 mm and higher.

4.4.6 Flow visualisation results for computational smoothing length

The following free surface comparisons are performed at the instant when the fluid is most energetic, during the first wave-to-wall interaction. Significant swirling behaviour is seen during this event. Such behaviour is likely to be misrepresented when too much smoothing occurs. The free surface comparison at the depth of 8.25 mm is shown in Figure 4.9. The comparison is between the experimental snapshot in (a), and SPH predictions obtained using a Lennard-Jones boundary treatment with a smoothing length of $1.2 \times \text{psep}$ in (b), and a gradient of kernel approximation with smoothing lengths of (c) 1.2, (d) 2.4, (e) 3.6 and (f) $4.8 \times \text{psep}$.

For the smoothing length of $1.2 \times \text{psep}$, changing the treatment of the boundary from the Lennard-Jones type force in (b), to the gradient of kernel approximation in (c), produces some local differences in free surface shape. Although this is the case, the nature of the predicted fluid behaviour is the same. As smoothing length is increased, the local detail of the free surface is smoothed out. At the larger smoothing lengths of 3.6 and $4.8 \times \text{psep}$, swirling behaviour is not predicted in Figures 4.9(e) and 4.9(f).

The same analysis as in Figure 4.9 is shown for 11 mm depth in Figure 4.10. As with the in 8.25 mm depth, the detail of the free surface is lost as smoothing length increases. The swirling nature of the fluid is unrecognisable at the smoothing lengths of 3.6 and $4.8 \times \text{psep}$ in Figures 4.10(e) and 4.10(f). In Figure 4.11, the same analysis is shown for 22 mm depth. The same conclusions can be drawn here as for the shallower depths. However, the extent of the loss of local detail due to smoothing is not as extreme.

At all liquid depths, a smoothing length of $1.2 \times \text{psep}$ produces the most accurate free surface shape. The type of boundary treatment used affects the free surface shape. However, the differences between the two methods are minimal, and are therefore considered to be insignificant. Increasing smoothing length reduces the amount of energy dissipation within the fluid. This reduction results in a more accurate damped structural frequency, and peak structural displacement amplitudes.

Increasing the smoothing length to a value higher than $2.4 \times p_{sep}$ causes excessive smoothing. This results in the loss of significant local detail in the free surface. Identification of the fluid behaviour responsible for effective control becomes inherently difficult. This difficulty limits the design capabilities of the modelling tool. It is for these reasons, that a smoothing length of $2.4 \times p_{sep}$ is considered to be the best compromise for predicting both the structural response and fluid behaviour at the free surface, amongst the smoothing lengths tested.

4.5 Conclusions

A sloshing absorber can successfully mitigate vibration of a light resonant structure. To optimise control, it is more important to select a liquid depth that maximises energy dissipation, than one that tunes the sloshing frequency to coincide with the natural frequency of the structure. The sloshing absorber's performance in terms of settling time is largely insensitive to the amount of fluid used, within a range of liquid depths from 2.75 mm to 11 mm, similar to the range identified in Chapter 2. Such insensitivity is of great practical advantage from a design point of view.

SPH has been used to predict the fluid-structure interaction between a structure and the sloshing absorber. The quality of prediction is dependent on the nature of fluid behaviour, being more accurate when the flow is dynamic. When the fluid is relatively less dynamic, excess energy dissipation is predicted. This excess results in the forecasting of lower peak displacements for the structure than those observed. With liquid depths of and above 8.25 mm, the predicted period of structural oscillation increases during small displacements, also seemingly as a result of excessive energy dissipation within the fluid.

At the liquid depth of 2.75 mm, free surface shapes are predicted well. Some observed local fluid behaviour is not replicated exactly, particularly when hydraulic jumps are observed. Overall fluid distribution is accurately predicted at all instances. This is considered to be more important due to the pressure force exerted on the structure by the fluid being an integral effect. The accuracy of free surface shape predictions increases with liquid depth. However, the phase difference that develops between the predicted and observed structural motion when controlled by depths of 8.25 mm and higher, makes presenting a ‘fair’ free surface comparison at these depths difficult.

The SPH smoothing length used for these depths has been varied in an attempt to control the amount of structural damping produced by the fluid, ζ_{eq} . Increasing the smoothing length from 1.2 to 2.4 x psep reduces ζ_{eq} to an acceptable level. The result is improved accuracy of the predicted structural response, whilst maintaining an acceptable level of free surface detail. A further increase results in excessive smoothing, and the inherent loss of significant local information at the free surface.

Overall, SPH predicts the behaviour of the structure/sloshing absorber system soundly. At all liquid depths, SPH provides a good prediction of settling time and structural motion, proving the method to be a valuable tool for sloshing absorber design.

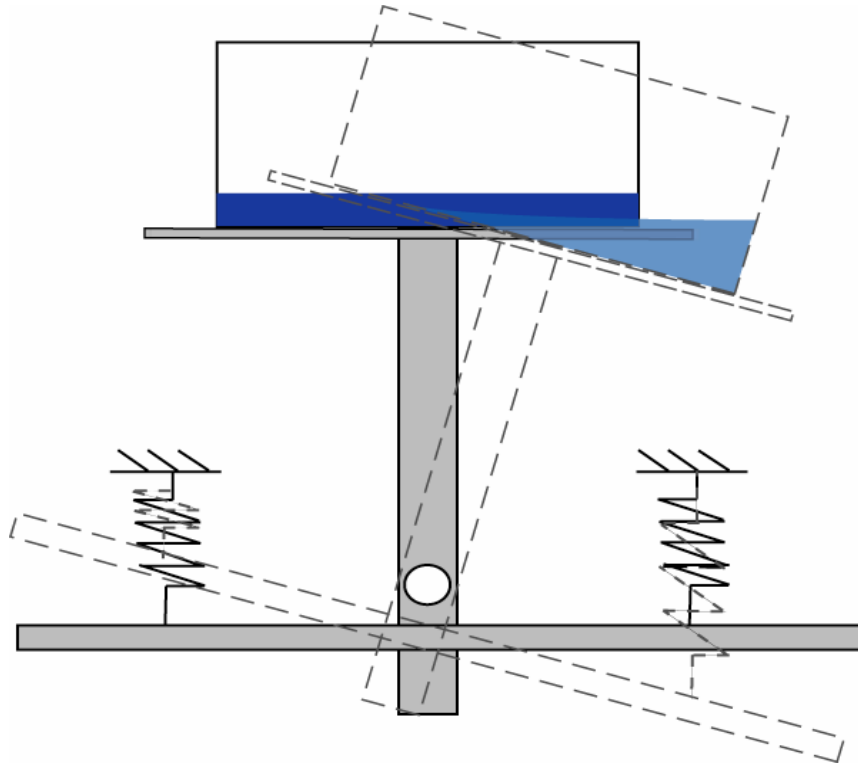


Figure 4.1. Showing the structure and the sloshing absorber at rest (vertical) and at initially displaced positions. Repeat of Figure 2.2(a)

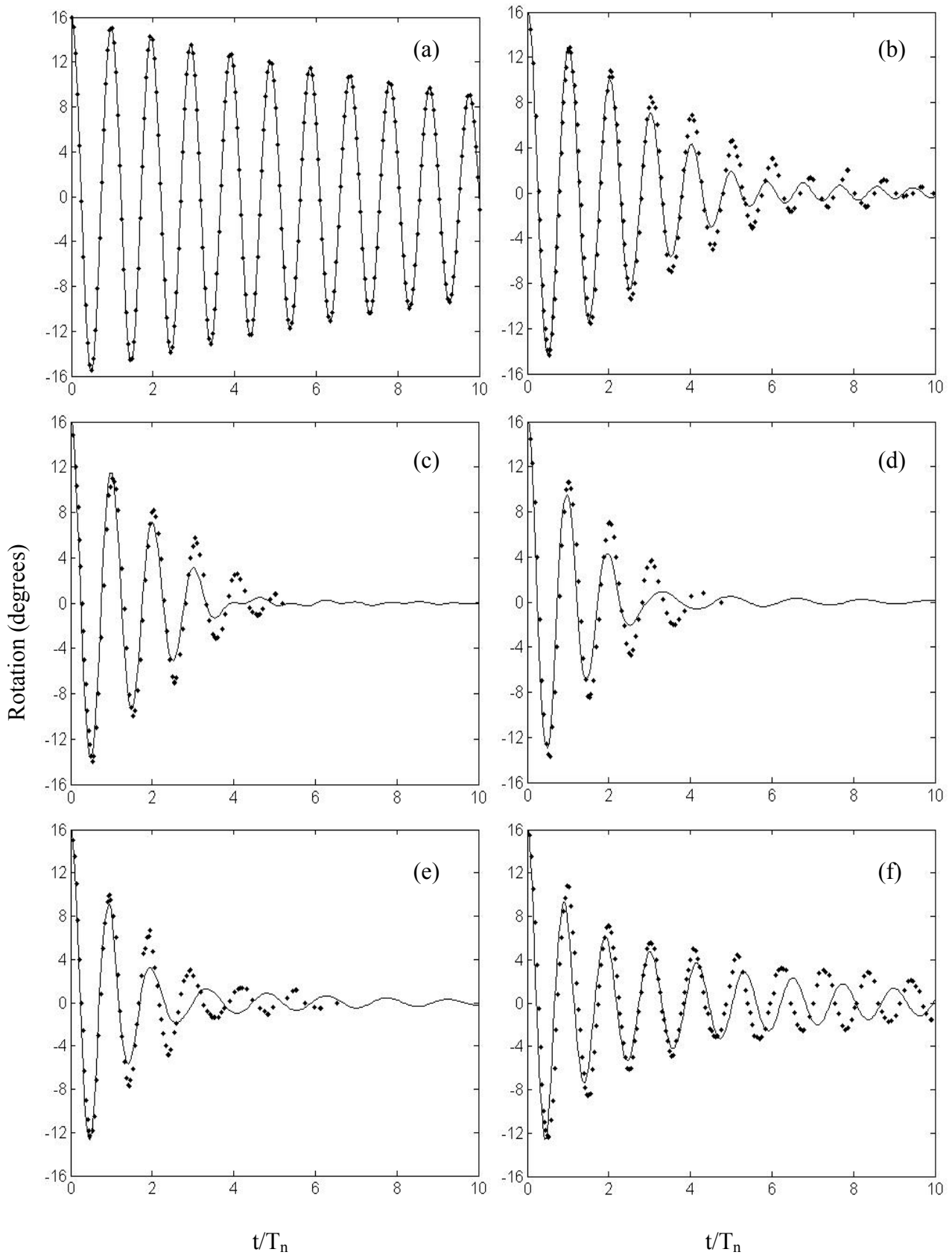


Figure 4.2. History of angular displacement of experimental observations (●) and SPH predictions (—) for (a) uncontrolled, (b) 2.75 mm, (c) 5.5 mm, (d) 8.25 mm, (e) 11 mm and (f) 22 mm deep cases. Lennard-Jones boundary treatment. Smoothing length (h) of 1.2.

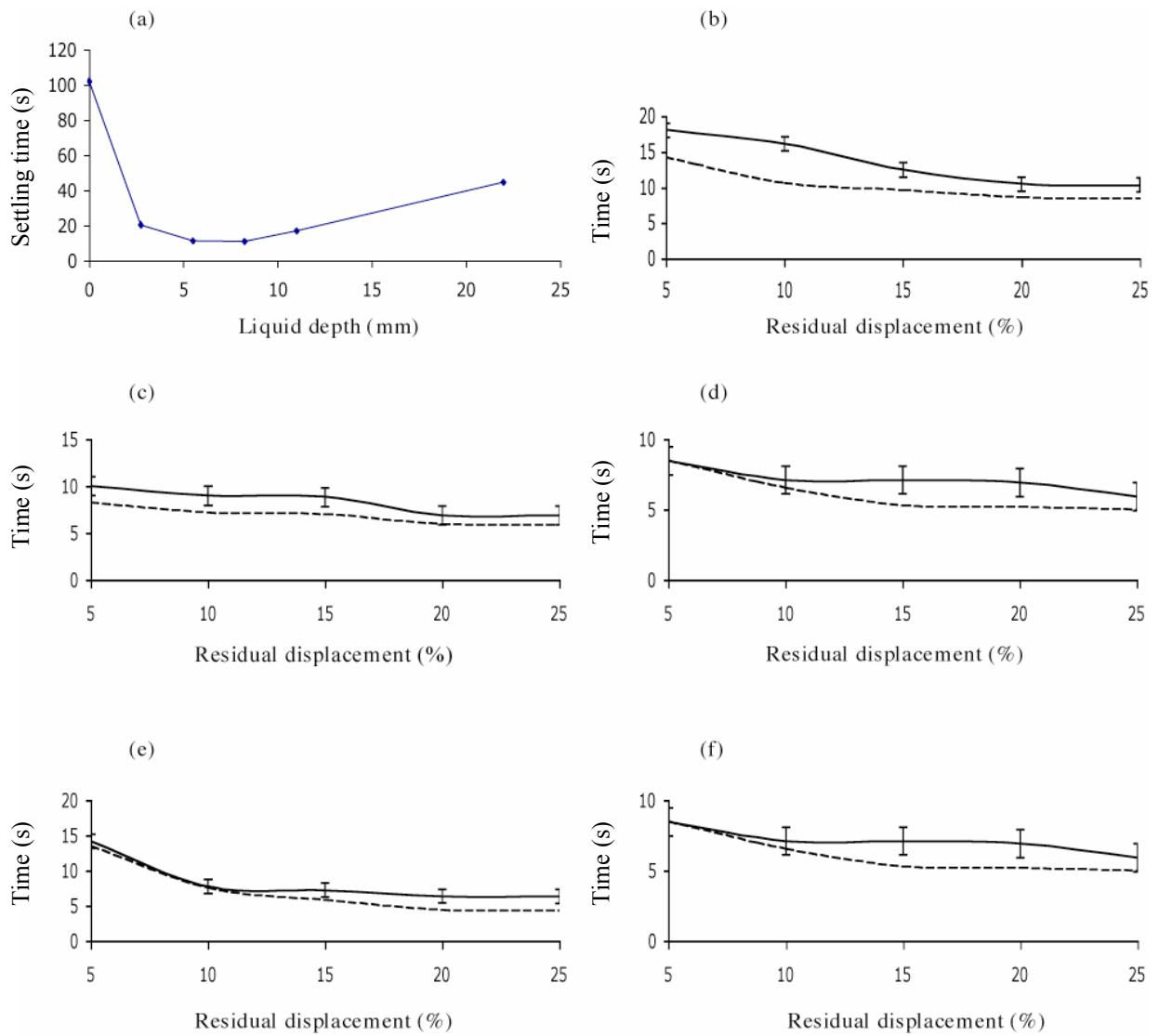


Figure 4.3. (a) Variation of experimentally observed settling time with liquid depths and residual displacement comparisons for (b) 2.75 mm, (c) 5.5 mm, (d) 8.25 mm, (e) 11 mm and (f) 22 mm liquid depths between experiments (—) and predictions (---).

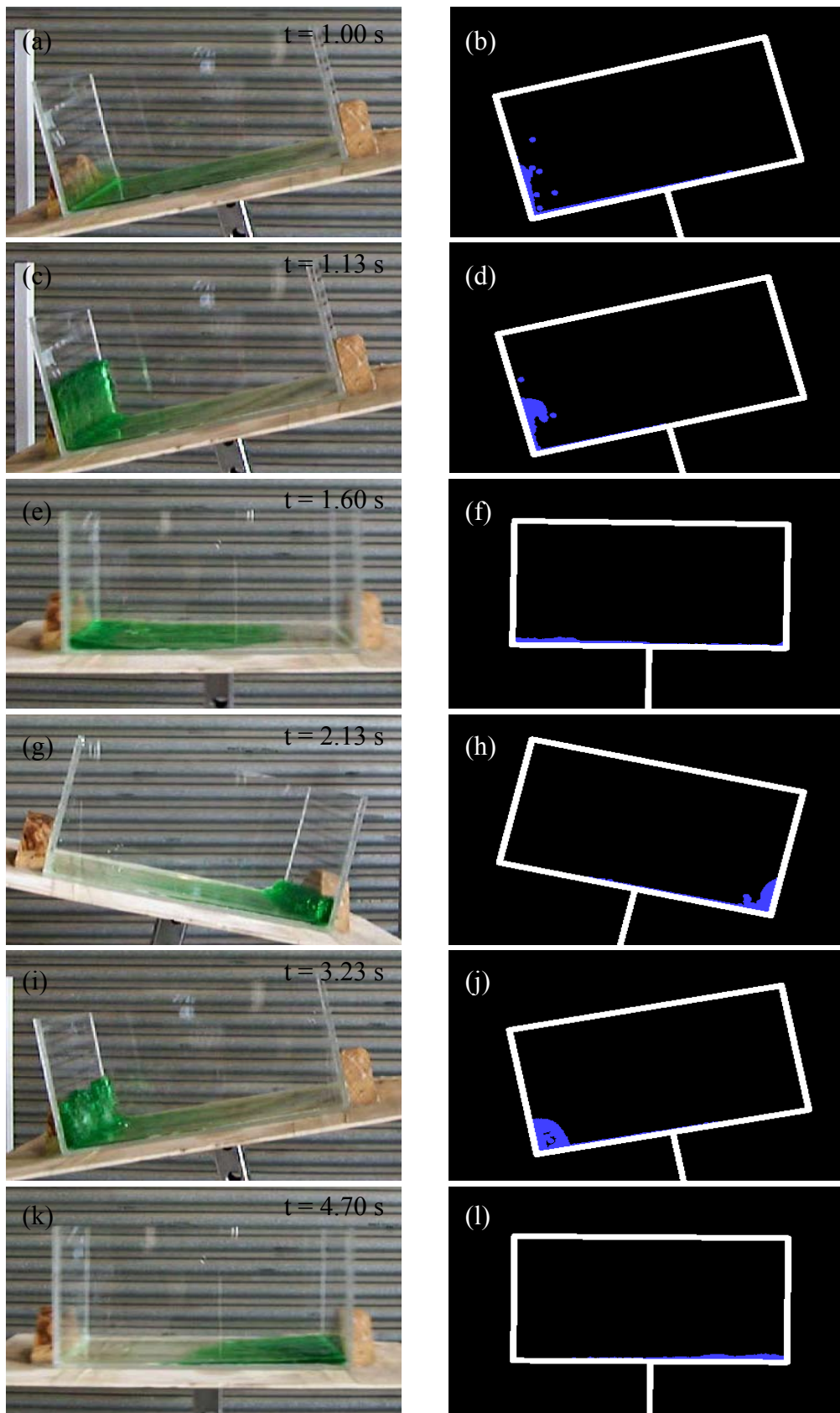


Figure 4.4. Free surface comparisons of 2.75 mm liquid depth at different marked instances. The left column has the experimental observations, and the right column has the numerical predictions.

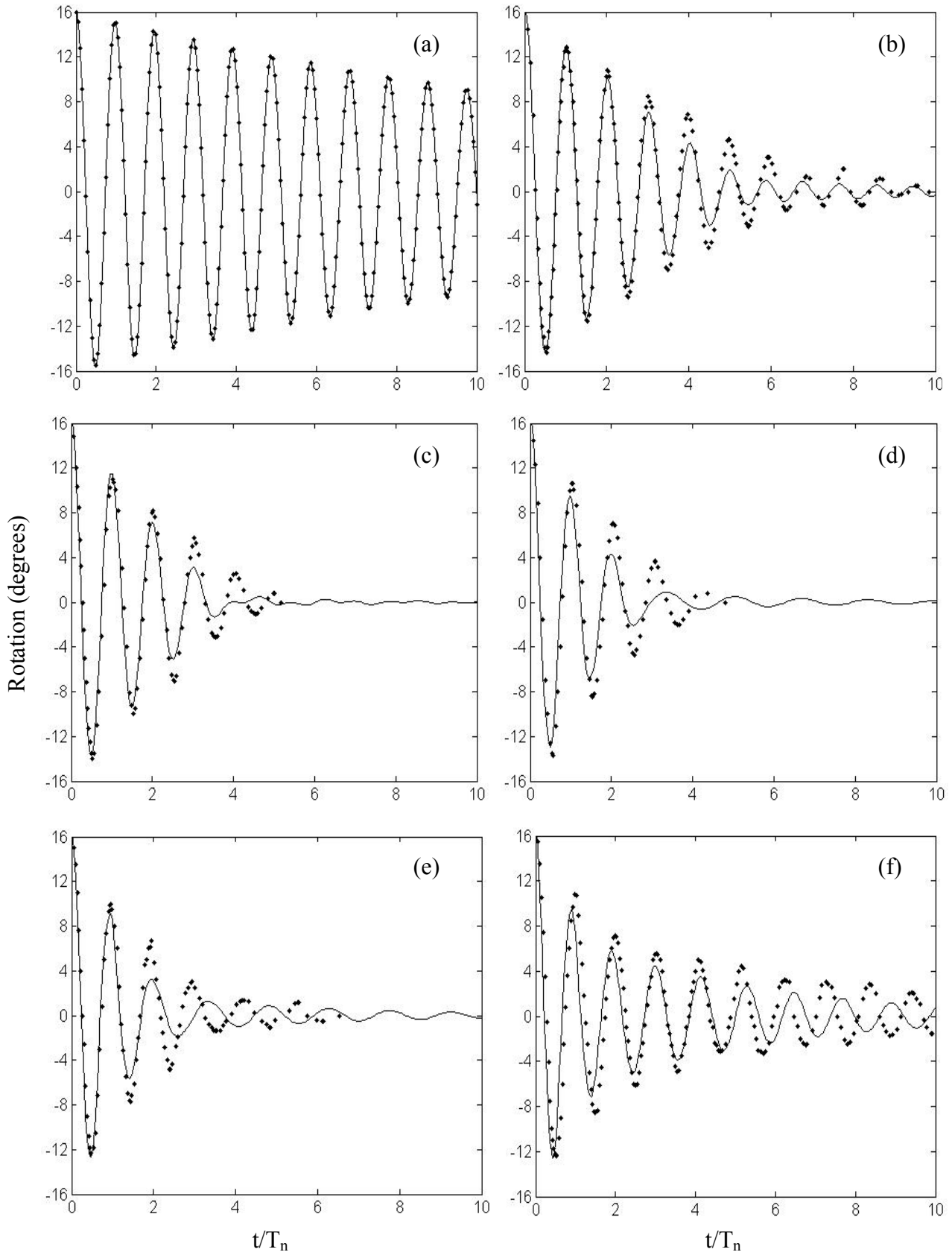


Figure 4.5. Same as in Figure 4.2, but for a gradient of kernel boundary approximation. (a) uncontrolled, (b) 2.75 mm, (c) 5.5 mm, (d) 8.25 mm, (e) 11 mm and (f) 22 mm deep cases. Smoothing length of 1.2 x psep.

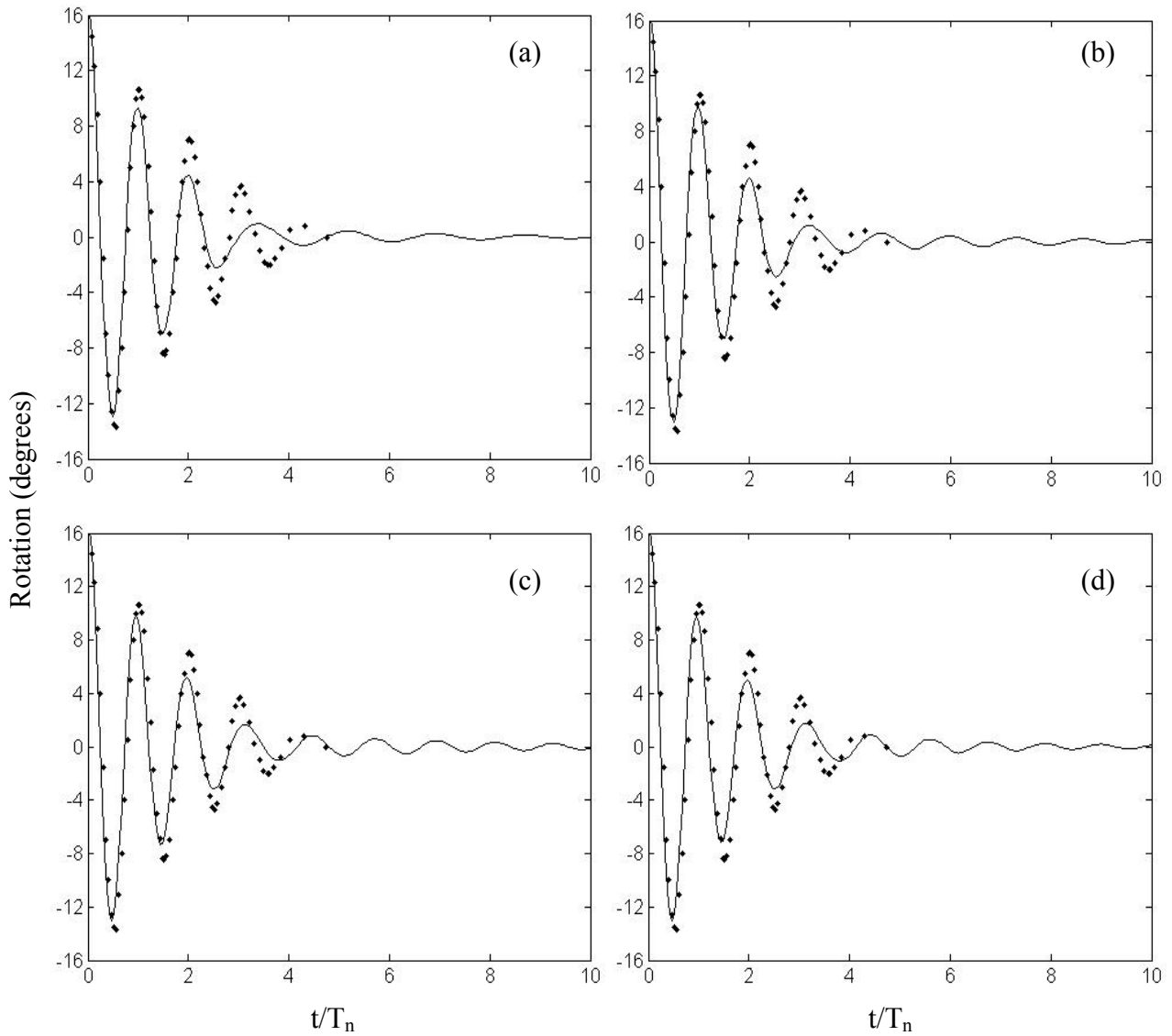


Figure 4.6. History of angular displacement of experimental observations (•) and SPH predictions (—) for 8.25 mm depth. Smoothing lengths of (a) 1.2, (b) 2.4, (c) 3.6 and (d) 4.8 x psep.

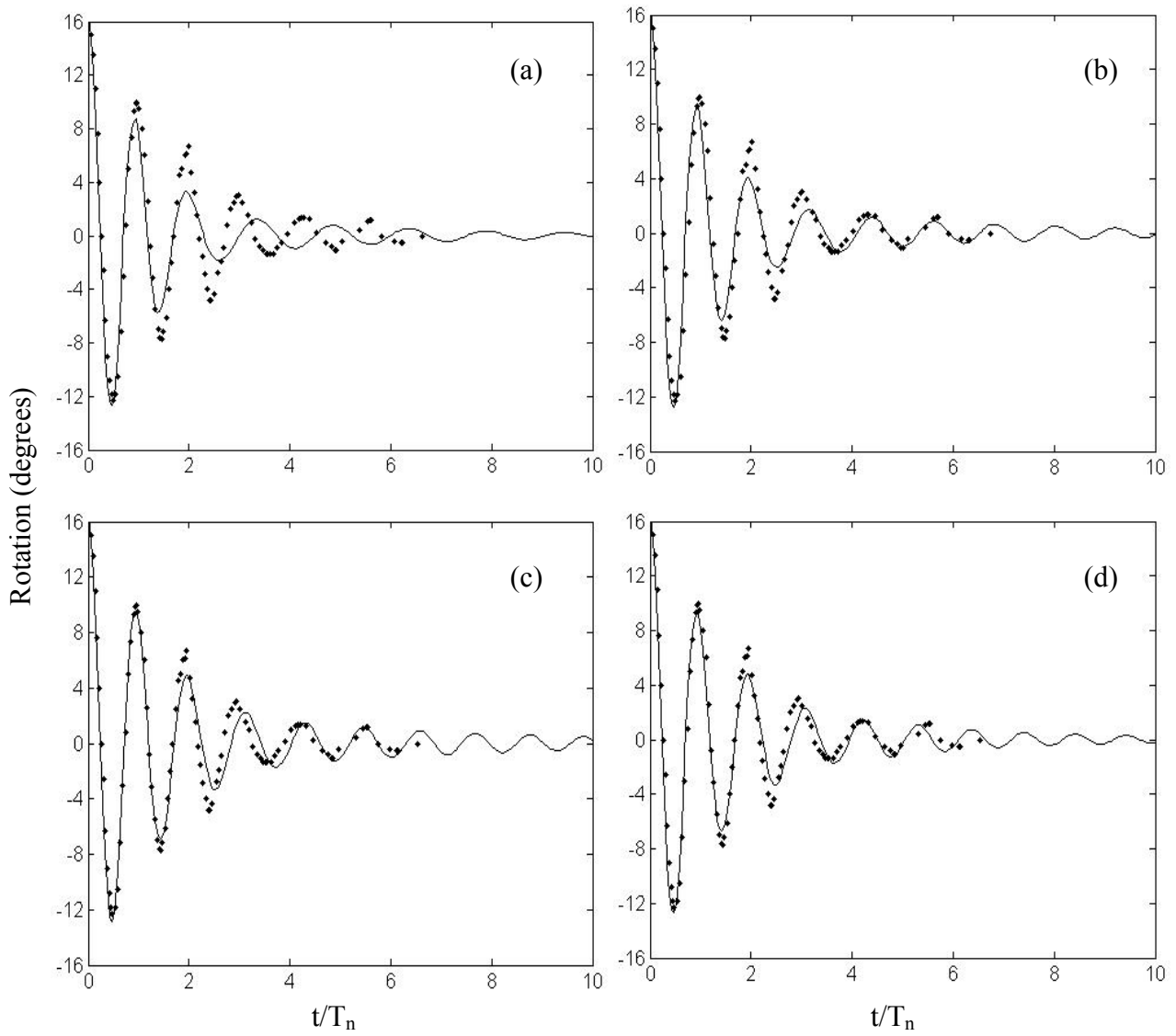


Figure 4.7. Same as in Figure 4.6, but for 11 mm depth.

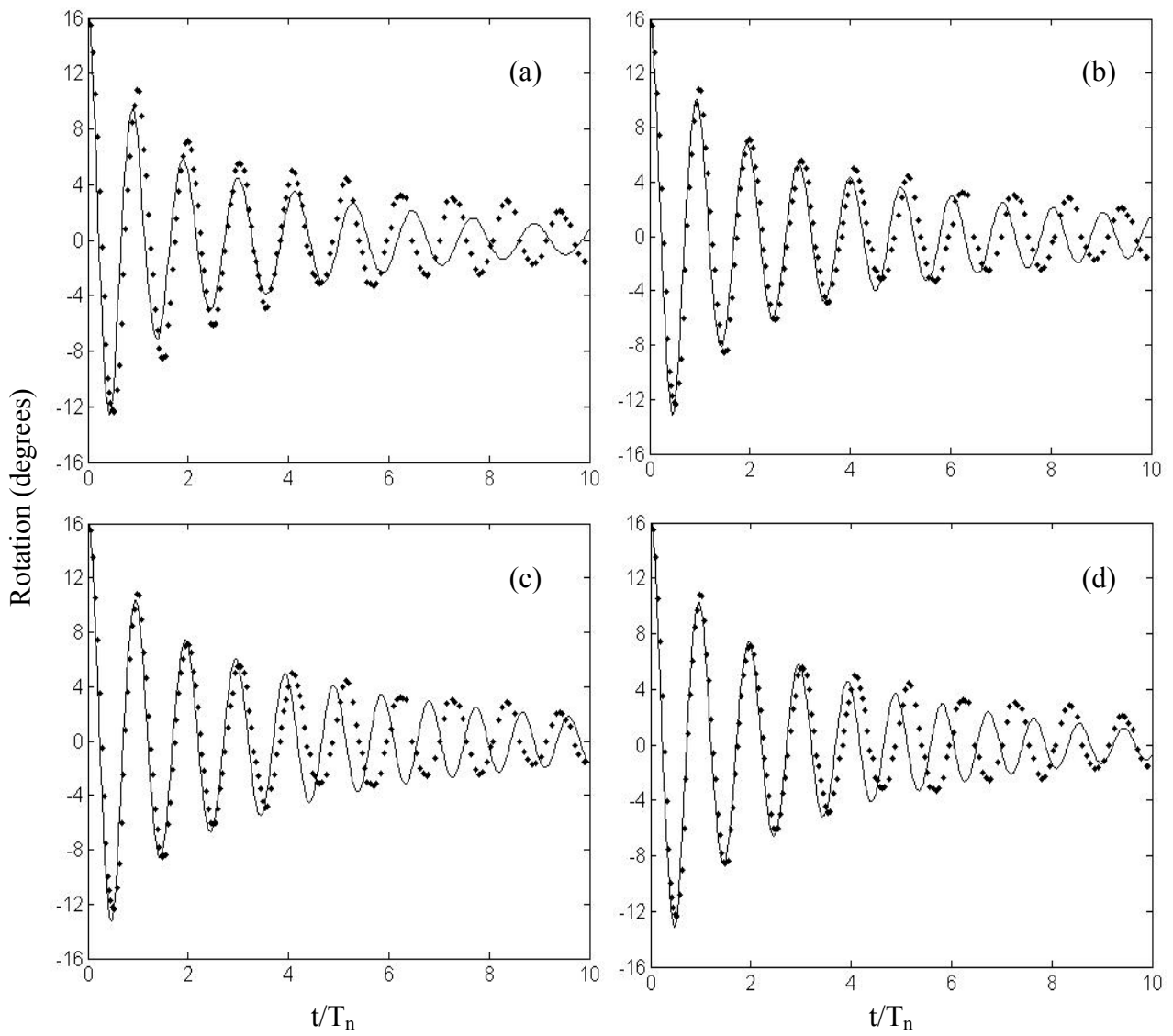


Figure 4.8. Same as in Figure 4.7, but for 22 mm depth.

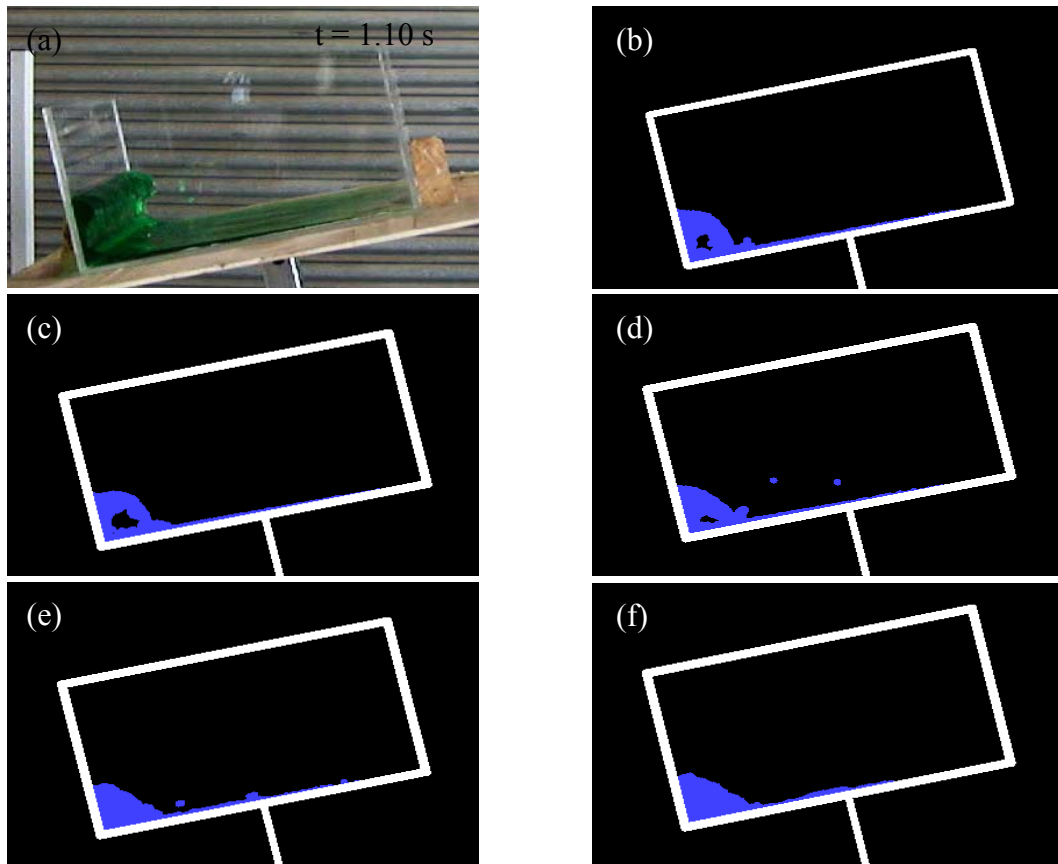


Figure 4.9. Free surface comparison between the experimental snapshot in (a), and SPH predictions obtained using a Lennard-Jones boundary treatment with a smoothing length of $1.2 \times \text{psep}$ in (b), and a gradient of kernel approximation with smoothing lengths of (c) 1.2, (d) 2.4, (e) 3.6 and (f) $4.8 \times \text{psep}$.

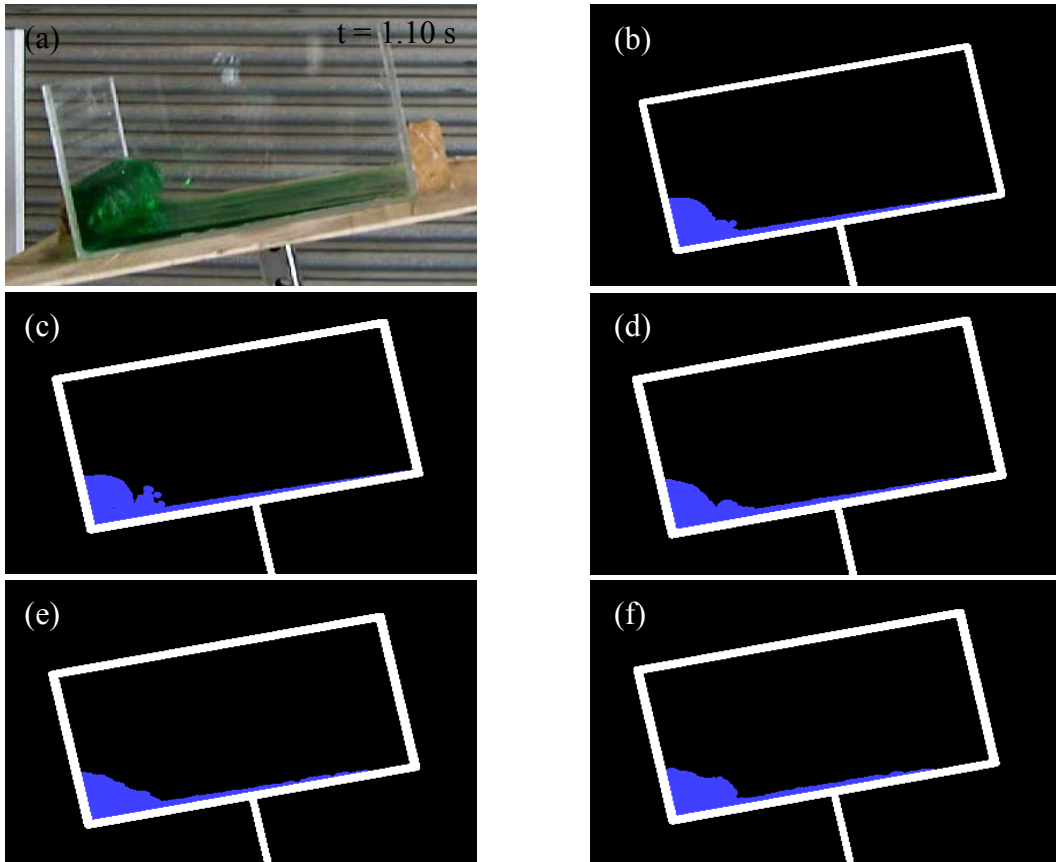


Figure 4.10. Same as in Figure 4.9, but for 11 mm depth.

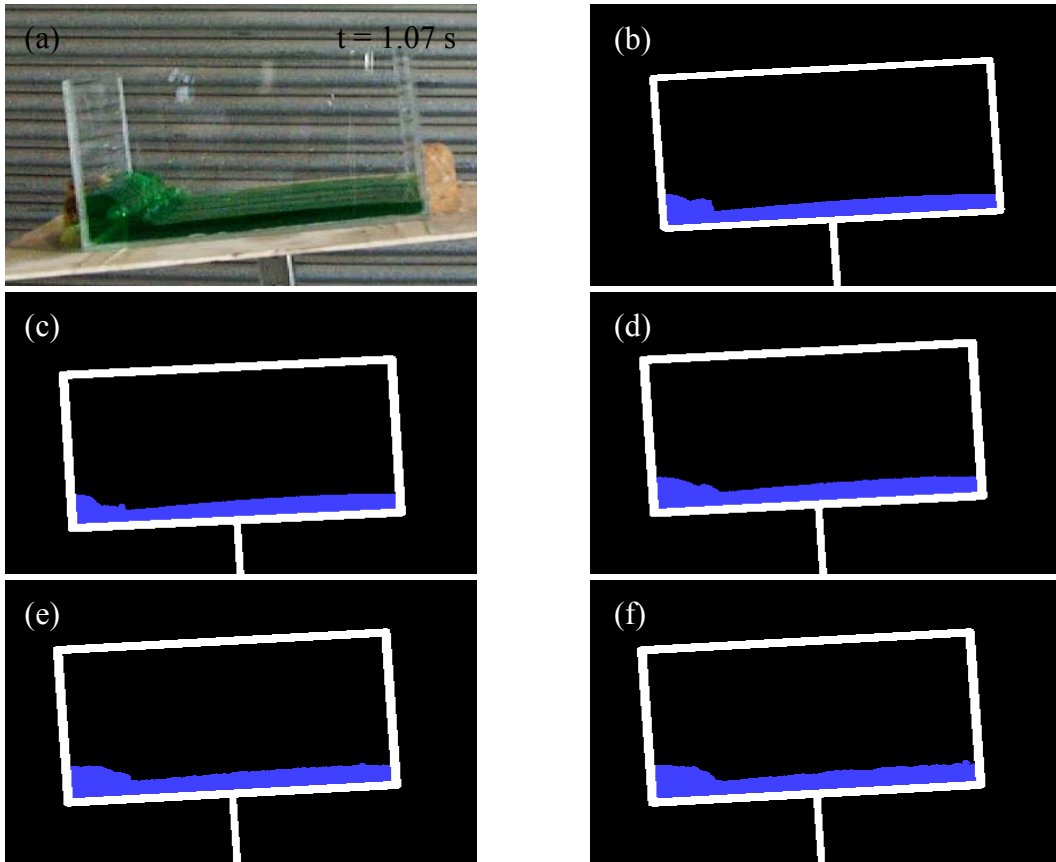


Figure 4.11. Same as in Figure 4.10, but for 22 mm depth.

Chapter 5

A STUDY OF SLOSHING ABSORBER GEOMETRY FOR STRUCTURAL CONTROL WITH SPH

5.1 Introduction

Thus far in this thesis, performance characteristics of rectangular sloshing absorber's have been presented for structural control, along with design initiatives to achieve improved performance. In this chapter, alternative sloshing absorber geometries are used to control a structure. The relationship between an absorber's shape and its control performance is investigated. The primary objective is to explore potential enhancements, with simple shapes, different than a rectangular one.

In the past, significant effort has been focused on increasing energy dissipation performance of the widely used rectangular absorber geometry. Variations on the conventional design have included the introduction of wedge shaped objects on the container bottom (Modi and Akinturk, 2002), baffles on the container walls (Anderson at al., 2000), wall flexibility (Gradinscak at al., 2002) and the introduction of floating solid particles at the free surface (Tamura at al., 1996). Studies involving varying liquid depth have been undertaken, focusing on increasing the amount of energy dissipation produced (Anderson at al., 2000; Guzel at al., 2005; Reed at al., 1998). These studies have demonstrated that shallow depths are more effective at dissipating energy than deep liquid levels, on a per unit mass basis. Yet prior to the work in this chapter, a comparative study on the effect of different container shapes has not been reported.

Smoothed Particle Hydrodynamics (SPH) is used to model fluid-structure interaction of the structure/sloshing absorber system in two dimensions. The structure to be controlled is a system with a single degree of freedom possessing stiffness and light damping. The structure is subject to a transient excitation in the form of an initial velocity. It is then allowed to respond dynamically, coming to rest due to its own damping and the added control of the sloshing absorber.

5.2 Numerical Model

Smoothed Particle Hydrodynamics (SPH) is used in this study to model the interaction between the sloshing liquid and the absorber container coupled with the structure to be controlled. The same SPH code has been used here as that in chapter 2. A schematic representation of the modelled structure/sloshing absorber system is given in Figure 5.1. In the numerical model, the rigid container of a sloshing absorber is represented by a partially constrained moving boundary, allowed dynamic translation in one-direction, only. Tethers are attached to the boundary, representing the force relationship between the structure and the absorber. This relationship exists due to the structure's stiffness (k) and viscous damping (c) properties. The structure's stiffness (k), and mass (m) are 4260 N/m and 60.5 kg respectively, to give a natural frequency of 1.33 Hz. The viscous damping coefficient is chosen to give a critical damping ratio of 1%, to represent a lightly damped resonant structure. The sloshing absorber attached on the structure consists of a container partially full of liquid. The sloshing fluid is water with a density of 1000 kg m^{-3} and dynamic viscosity of 0.001 Pa s.

As in Chapter 3, a particle size of 0.8 mm by 0.8 mm is used to model the water within the container in a two-dimensional space. Based on the comparison given in Figure 3.2, this particle size represents a reasonable compromise between accuracy and computational speed. The time step of integration is $1\mu\text{s}$, corresponding to approximately 75,000 integration steps for each natural period of oscillation. This time step is limited by the Courant condition modified for the presence of viscosity, given in Appendix 1, Equation A15.

The fluid within the container is allowed to settle under gravity for one second, so that it reaches an initial state of rest. The structure is given an initial velocity of 0.5 m/s over one time step. The structure is allowed to respond freely, and its motion excites the water within. Liquid depth is kept relatively shallow in order to promote travelling free surface waves. In all cases, mass of the sloshing water is 6.05 kg, 10% of the structure's mass.

5.3 Rectangular geometry

The dashed line in Figure 5.2(a) is the displacement history of the uncontrolled structure. Maximum displacement reached by the structure, is around 60 mm. The light damping characteristics of the structure result in almost unrestricted free vibration.

The response of the structure is significantly improved with a tuned rectangular sloshing absorber, indicated by the solid line in Figure 5.2(a). An approximately 95% reduction in the time taken for the structure to come to rest, is achieved here relative to the uncontrolled case. For the rectangular container, the container width and liquid depth have been chosen (tuned) to produce a 1.33 Hz fundamental sloshing frequency equal to the natural frequency of the structure using the standard approach (Milne-Thomson, 1968). This tuning corresponds to a container width of 200 mm and a liquid depth of 30 mm.

Strong fluid-structure interaction occurs within this type of absorber. Such interaction transfers energy from the structure to the fluid through the sloshing force. This force is the resulting net effect from the pressure (normal) force and tangential force due to shear stress that the fluid exerts on the boundary. The control characteristics produced by the sloshing force can be demonstrated by examining the fluid power exerted on the container. Fluid power is the dot product of the sloshing force and the structure's velocity. Control is achieved when the product is negative. When the product is positive, on the other hand, fluid excites the structure, sometimes resulting in an undesirable beat in the structure's displacement history.

The histories of fluid power and structure's displacement for the first 10 seconds of simulation for the tuned rectangular sloshing absorber, are shown in Figure 5.2(b). All peaks in power correspond to instances when a wave impacts on a container wall, near maximum structure velocity (or zero displacement). Significant negative power and almost no positive power is seen through the first two cycles of structural oscillation. Control is highly effective as a result. Fluid begins to excite the structure in the 2nd half of the 2nd cycle continuing through to the 5th. After the 5th cycle, the power magnitude becomes almost insignificant, with minimal control effect.

Snapshots of some critical physical events within the rectangular container, are shown in Figure 5.3. Fluid and boundary colouring relate to the scales shown below each frame. In the left hand column, this scale indicates fluid velocity in m/s. In the right hand column, it is an indication of the rate of shear energy dissipation in W. Shearing of the fluid is the primary form of mechanical damping in such flows. Shear stress is defined in the same way here, as that in Gomme et al, 2006. Initially, the fluid and structural motion are highly energetic and out of phase with one another. The opposition of the fluid and structural momentum exerts a strong controlling effect on the structure.

Two distinct system states are observed. The first is of high fluid kinetic energy and high structural potential energy. The second is of high fluid gravitational potential energy and high structural kinetic energy. The instant shown in Figure 5.3(a) is an example of the second state described. The wave-to-wall interaction shown is responsible for the second peak in fluid power seen in Figure 5.2(b), when the fluid elevation is maximum. At this instant, the rate of shear energy dissipation is also high at the container bottom and right wall, as shown in Figure 5.3(b).

The wave-to-wall interaction that follows, shown in Figure 5.3(c), causes fluid to rise to the container ceiling against the left wall. The extensive free surface deformation seen here prolongs the duration of the interaction, and therefore, the time over which it has a controlling effect. This type of wave-to-wall interaction is typical within the rectangular container, when subject to such large amplitude excitation. This event produces the third power peak in Figure 5.2(b). The rate of shear energy dissipation continues to increase at the boundary. Significant dissipation is also observed at the free surface in Figure 5.3(d).

The large free surface deformations produced during wave-to-wall interaction cause the phase difference between the fluid and structure to close. The first event responsible for producing positive fluid power is shown in Figure 5.3(e). A travelling wave has moved through the container from right to left, impacting on the left container wall and producing a hydraulic jump. At the instant of collision, fluid and structural motion are in phase, albeit for a short period of time. The speed at which this wave travels causes very steep velocity gradients to be produced along the bottom of the container. A high rate of shear energy dissipation is seen in this area as a result, now indicated in red in Figure 5.3(f).

Fluid and structural motion are mostly in phase from around $t = 3.5$ s. Positive peaks are now larger than the negative peaks in fluid power. Energy is passed back to the structure as a result, causing an increase in structural displacement amplitude. Following events display smaller fluid elevations during the wave-to-wall interactions than previously seen. In Figure 5.3(g), a small, breaking travelling wave moves from wall-to-wall. The rate of shear energy dissipation is generally small, however it remains somewhat significant at the container bottom. From $t = 7.50$ s onwards, standing waves are observed, with further restricted control effect. Finally, structure's displacement decays to 1% of its maximum value at $t = 20.0$ s.

Peaks in sloshing force are caused by wave-to-wall interaction. The duration of these events along with sloshing force magnitude, is responsible for the amount of energy transferred. Duration is long when fluid reaches high gravitational potential energy. Therefore, high fluid elevation leads to high energy transfer. Although this is the case, excessive fluid elevation can cause in-phase motion between the fluid and the structure. This in-phase motion restricts the control effect due to momentum opposition, and it can even cause the fluid to excite the structure.

Energy transferred to the fluid must be dissipated effectively. Viscous dissipation is the primary form of dissipation within the working fluid. Wave-to-wall interaction and travelling wave motion produce high shear stress at the container walls and at the bottom. Dissipation performance is poor when travelling waves do not exist.

5.4 Effect of container shape

The effects of implementing angled and curved surfaces as absorber geometry are investigated next. The objective is to improve on the control characteristics of the tuned rectangular absorber design. The shapes in Figure 5.4 have been chosen to control the structure, due to their significant differences from one another, and simplicity in design.

A constant free surface length of 200 mm (f_l) is kept in all cases except for the circular cylinder in Figure 5.4(b). Keeping both liquid depth and free surface length constant is not possible, for different shapes. Hence, the liquid depth is allowed to vary, as indicated in the figure. The same fluid volume is used in all containers to keep the added fluid mass at 10%. For the circular cylinder, this condition results in a free surface length of 174 mm to keep the liquid height similar to other cases at 50.8 mm.

The displacement histories of the structure, in the same order as that in Figure 5.4, are shown in Figure 5.5. In Figure 5.5(a), the tuned rectangular absorber, is the most effective controller. This effective performance is due to the fact that the free surface length of 200 mm and the depth of 30 mm, are tuned to the natural frequency of the structure to be controlled for the purposes of momentum opposition. All other shapes in Figure 5.4, however, only maintain the same free surface length. Hence, they cannot be considered 'tuned'.

In Figure 5.5, rows 2 and 3 show behaviour that may be useful. Row 2, with converging walls, is quite effective in dissipating energy rapidly. Row 3, with diverging walls, show clearly beating envelopes indicating the presence of strong interaction between the fluid and the structure but lack of effective dissipation. Beating manifests as an increase in structural displacement amplitude, caused by the fluid exciting the structure. The implementation of more complex elliptical sidewalls (in row 4) shows no advantage over the simpler linear arrangements, whereas the circular cylinder in Figure 5.5(b) is the poorest performer.

The difference in control characteristics for four different containers is demonstrated through the fluid power histories in Figure 5.6. The case of the tuned rectangular absorber in Figure 5.2(a) is repeated in Figure 5.6(a) for the purpose of comparison. The circular cylinder in Figure 5.6(b) produces significant control during the first cycle of structural oscillation. The first cycle of structural vibration produces significant control. After this, the circular surface produces a standing waveform. The fluid now acts mainly as an added mass. The power is positive periodically, exciting the structure around half of the time. Poor control is observed as a result.

The performance is shown in Figure 5.6(c) of the converging trapezoid (with 30-degree wall angle). Initially, the fluid motion is out of phase with that of the structure. Introduction of positive power is seen from the second cycle of vibration. More positive power peaks are seen here than in the tuned rectangular absorber, yet no beat is observed in the structural displacement history. The lack of beat is due to the fluid motion staying in-phase with that of the structure for short periods of time only.

Figure 5.6(d) corresponds to the diverging trapezoid (with 30-degree wall angle). Beating is clearly seen in the power history for this case. Energy transfer is effective in this shape. However, the fluid's inability to dissipate all of this energy results in its being passed back to the structure periodically, causing a beat envelope.

5.5 Tuning trapezoidal containers

Tuning of the free surface length in the diverging and converging trapezoids is analysed next. The objective is to establish a free surface length that produces a sloshing frequency equal to the natural frequency of the structure. Optimal effectiveness occurs when the absorber is tuned in this way. The performance of these shapes can then be compared fairly with the tuned rectangular geometry.

Histories of structural displacement, when coupled to a diverging trapezoid (with 30-degree wall angle) are shown in Figure 5.7. Figures 5.7(a) to 5.7(k) correspond to free surface lengths of 150 mm, 160 mm, 170 mm, 180 mm, 190 mm, 200 mm, 210 mm, 220 mm, 230 mm, 240 mm, and 250 mm, in descending order. The beat gets stronger with shorter beat periods, with increasing free surface length until 220 mm. Further increase in free surface length results in a reduction in sloshing frequency, to lower than the natural frequency of the structure. Beat strength and frequency reduce as a result. The diverging trapezoid is considered tuned at the free surface length of 220 mm.

Figures 5.8(a) to 5.8(k) correspond to free surface lengths of 150 mm, 160 mm, 170 mm, 180 mm, 190 mm, 200 mm, 210 mm, 220 mm, 230 mm, 240 mm, and 250 mm, in descending order, in the converging trapezoid (with 30-degree wall angle). Narrow free surface lengths produce an exponential decay in structural displacement. Damping effectiveness increases with free surface length. In Figure 5.8(h), decay envelope appears to be linear, where the converging trapezoid is considered to be tuned. This case is an improvement on the tuned rectangular absorber. From 220 mm onwards, performance deteriorates with increasing free surface length.

A summary of settling times for varying free surface length, in a converging trapezoid (with 30-degree wall angle) is shown in Figure 5.9. Settling time is defined as the time taken for structural displacement to reach a certain percentage of its maximum. The level of residual displacement is indicated in the figure caption. In instances where a data point is not given, the structure did not reach this level of residual displacement within the total simulation time. Settling time magnitudes decrease with increasing free surface length, until a value of 220 mm. Settling time increases from here with increasing free surface length. The absorber is considered tuned at the free surface length of 220 mm.

Structural displacement and fluid power histories for this tuned case are shown in Figure 5.10. At almost all instances negative power is observed. Only two significant positive power peaks are seen. The constant opposition of sloshing force to structural motion is responsible for the linear decay of its displacement.

In Figure 5.11, free surface comparisons are presented of the tuned rectangular (left column) and tuned converging trapezoid (right column) absorbers at instances of typical wave-to-wall interaction. Large free surface deformation is seen in the tuned rectangular absorber, reducing the sloshing frequency during these events. The walls of the converging trapezoid restrict free surface deformation by directing the fluid downward, keeping free surface length within an allowable range. This results in retaining the out-of-phase motion between the fluid and the structure.

5.6 Effect of varying excitation magnitude

The tuned rectangular and tuned converging trapezoidal absorbers' ability to handle varying excitation magnitudes is analysed next. The left and right columns of Figure 5.12 correspond to the structure's displacement with the rectangular and the converging trapezoid absorbers, respectively. Figures 5.12(a) and 5.12(b) correspond to an initial velocity of 0.25 m/s; Figures 5.12(c) and 5.12(d) correspond to 0.5 m/s; and Figures 5.12(e) and 5.12(f) to 1.0 m/s.

A relatively strong beat pattern is noticeable in Figure 5.12(a) for the tuned rectangular absorber subjected to the lowest initial velocity, 0.25 m/s. Significant standing wave development is observed (not shown) at this low level of excitation. The structure takes longer to come to rest here than the case when the excitation level is four times as large, shown in Figure 5.12(e). As the excitation magnitude is increased, the beat phenomenon becomes lighter, with the quickest settling time for 0.5 m/s and only very slightly longer time for the 1 m/s excitation.

In contrast to the rectangular container, the converging trapezoid is able to avoid passing enough energy back to the structure to cause beating. This is due to its ability to maintain out of phase motion and effective dissipation patterns. The trapezoidal container produces a comparable performance to that of the rectangular one for the largest disturbance, but it becomes clearly more effective for smaller disturbances. Hence, the robustness of the trapezoidal absorber may be of some significance when the external disturbance is of uncertain nature.

5.7 Conclusions

The tuned rectangular sloshing absorber can successfully mitigate vibration of structures subject to impulse type loading. Control is achieved by fluid-structure momentum opposition, and energy dissipation produced via shearing of the fluid. Dissipation via this means is highest at the container surface due to the no-slip condition. Significant energy dissipation occurs at the free surface when travelling waves are present. This waveform is discontinuous in nature, having steep velocity gradients and causing inherent high shear stress. For this reason, the travelling waveform should be encouraged.

A series of container shapes have been used to control the structure. The objective is to identify a geometry that has control characteristics superior to that of the tuned rectangular absorber. Controlling a structure with a circular cylinder shaped absorber results in poor control. A dominant standing waveform is seen in this shape, resulting in the fluid acting as added structure mass. The implementation of diverging walls at a 30-degree angle on rectangular geometry maximises energy transfer between the structure and the fluid. However, the fluid cannot dissipate this energy, resulting in its being passed back to the structure. Undesirable beating is seen in the structure's vibration history as a result.

Improvements on the tuned rectangular absorber can be made through a simple shape modification. Implementation of converging walls at a 30-degree angle eliminates beat, provided that the free surface length is tuned. The inherent restriction on free surface deformation ensures that out-of-phase motion between the structure and the fluid is maintained. The out-of-phase motion results in damping characteristics analogous to Coulomb friction, where the damping force always opposes structural velocity, producing a linear decay envelope.

The inward angled walls cause the free surface breakage during wave to wall interaction, producing travelling waves more readily than in a rectangular container. For this reason, inward angled walls may improve control performance over broader excitation levels, due to less effort being required to generate wave breaking and inherent effective energy dissipation.

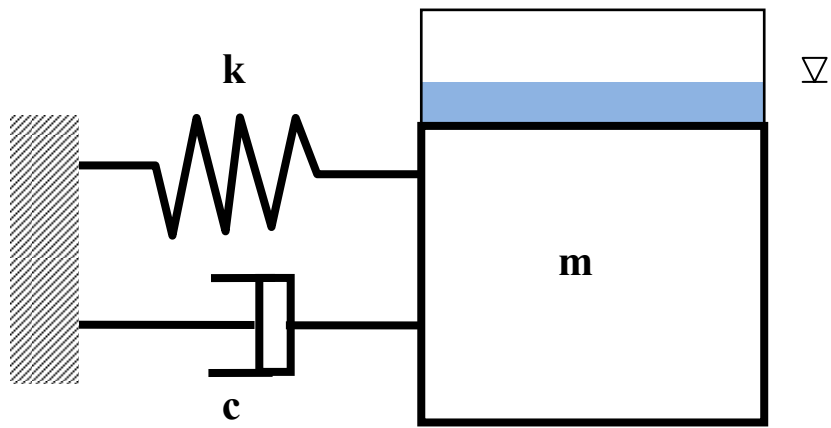


Figure 5.1. Tuned rectangular liquid damper coupled to a single degree of freedom structure. Repeat of Figure 1.1 for easy reference.

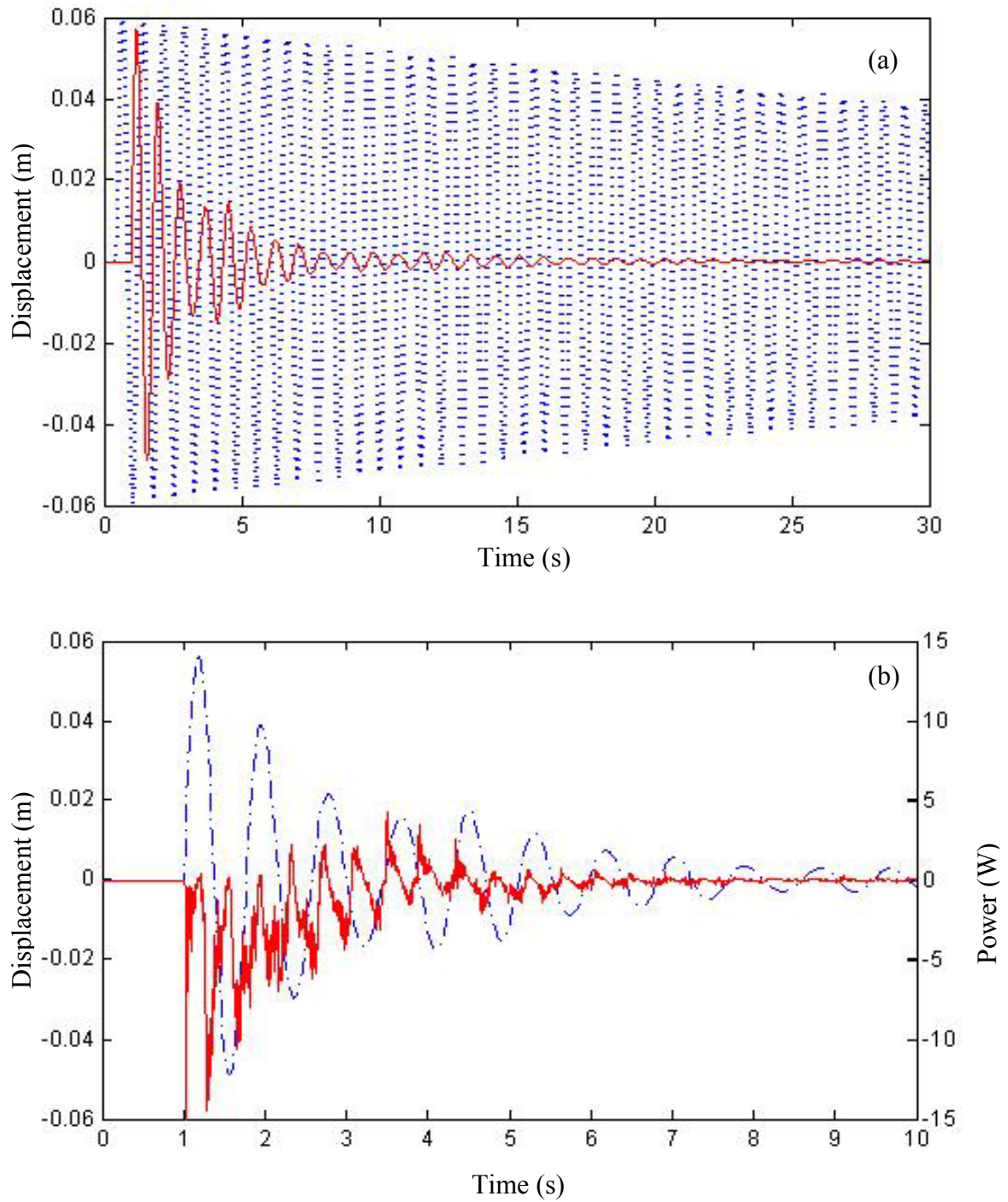


Figure 5.2. (a) Structural displacement history (---) uncontrolled and (—) controlled with a tuned rectangular liquid sloshing absorber. (b) First 10 seconds of the controlled structural displacement (— □ —) and the corresponding fluid power (—).

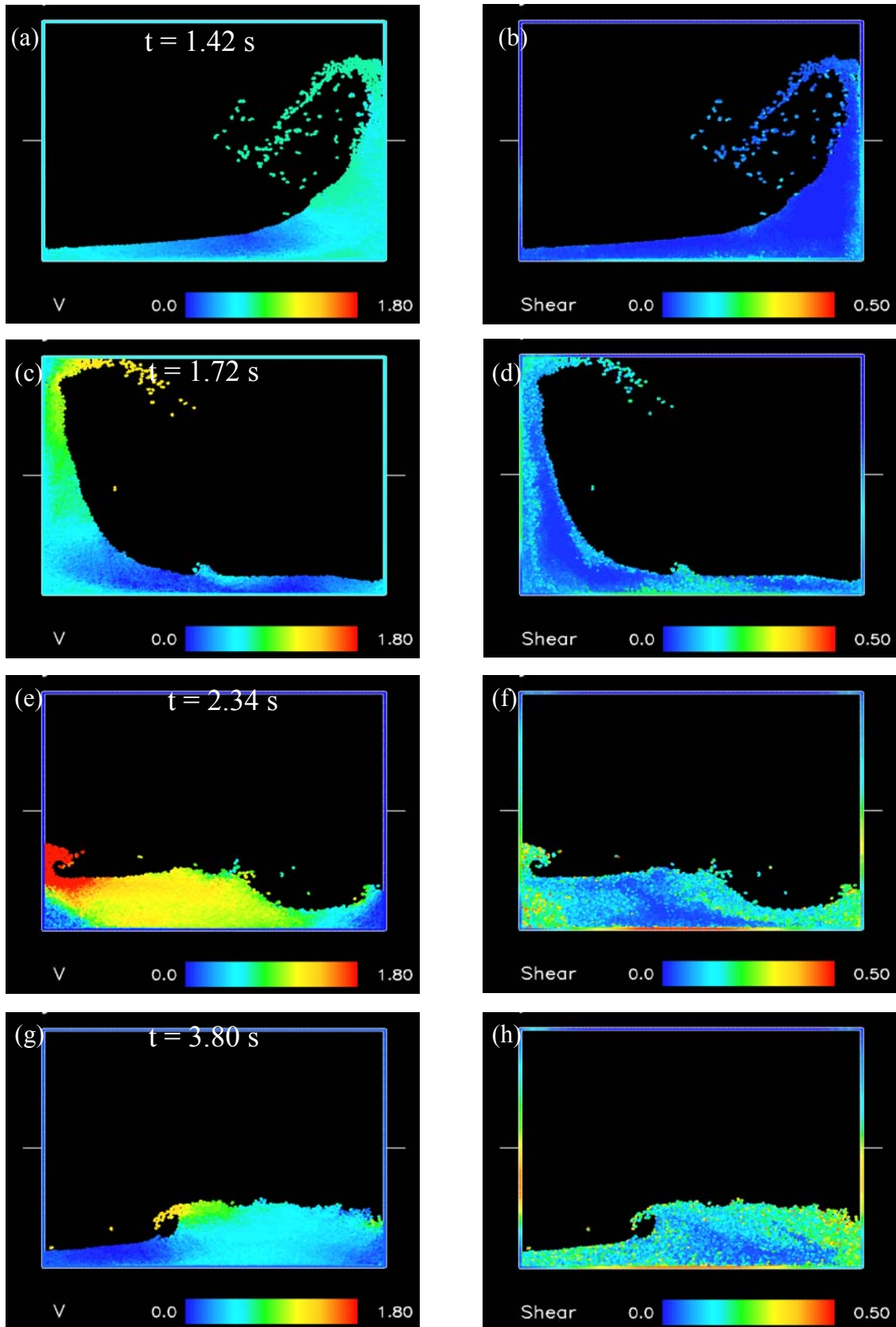


Figure 5.3. Still frames at instants of interest within the tuned rectangular absorber. Colour scale in the left column represents fluid speed (m/s); whereas the scale in the right column represents rate of shear energy dissipation (W).

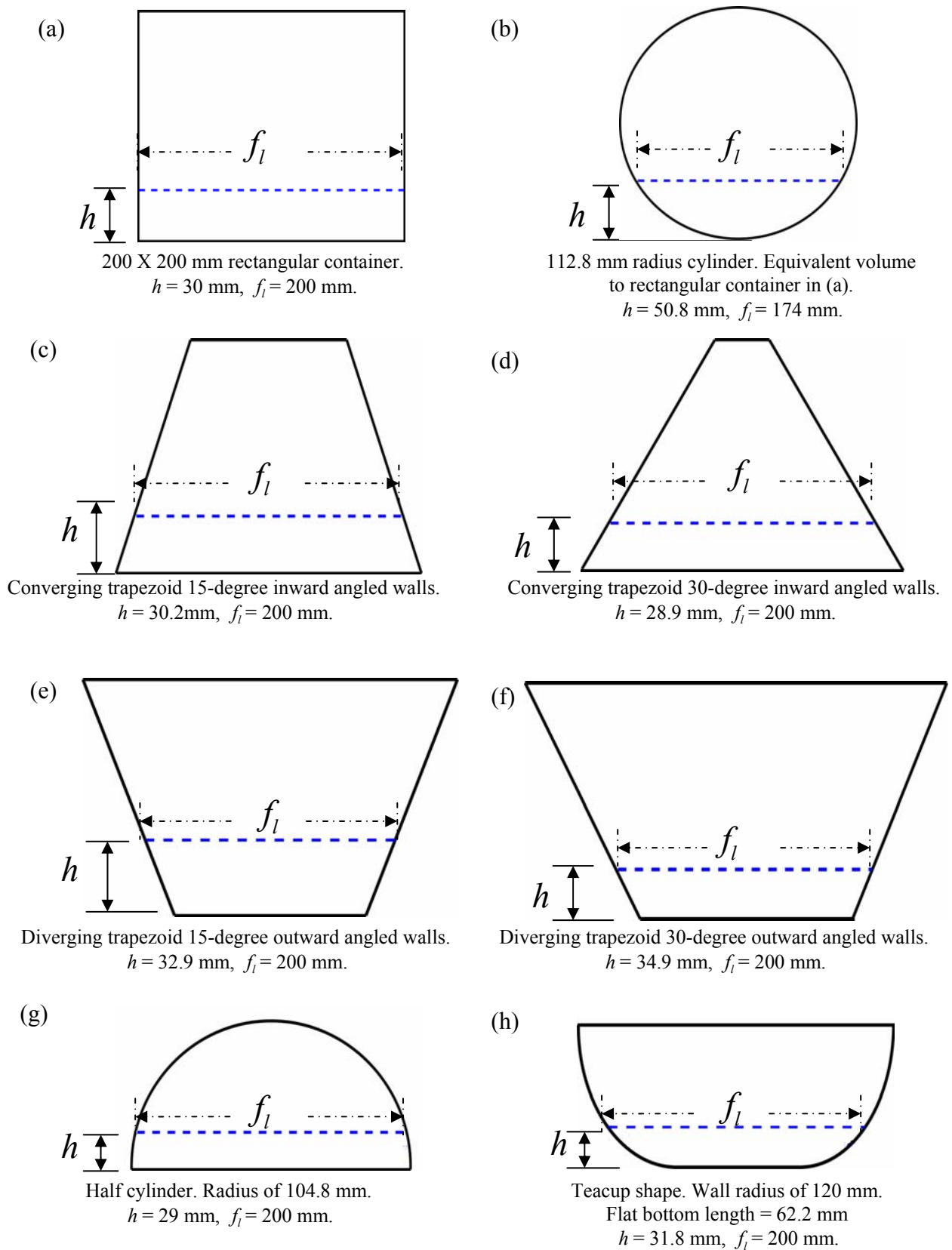


Figure 5.4. Series of shapes investigated. h is the liquid depth used, f_l is the free surface length. The same fluid volume was used in all shapes to keep added fluid mass constant at 10%. Dashed line indicates water free surface position.

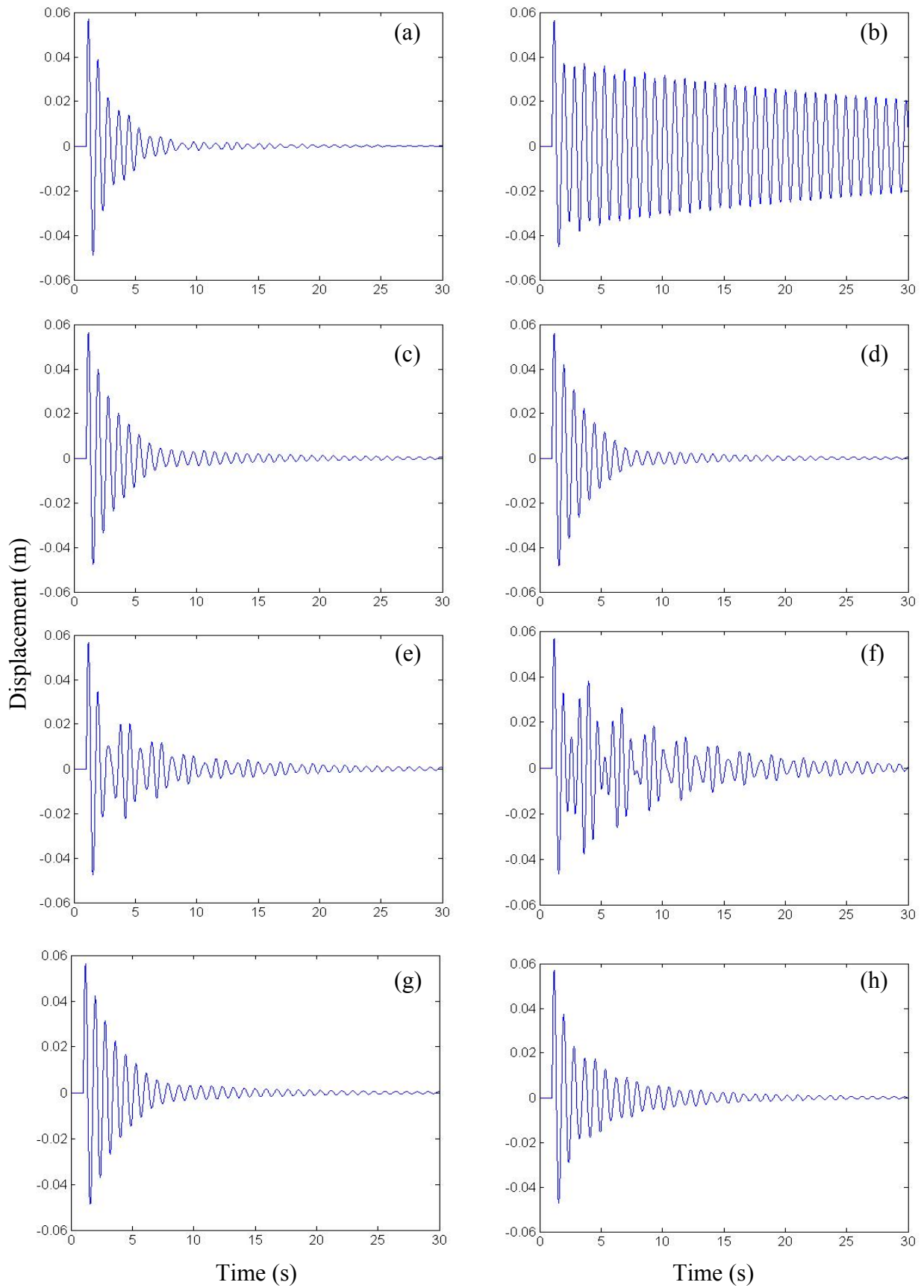


Figure 5.5. Structural displacement histories corresponding to shapes in Figure 5.4.

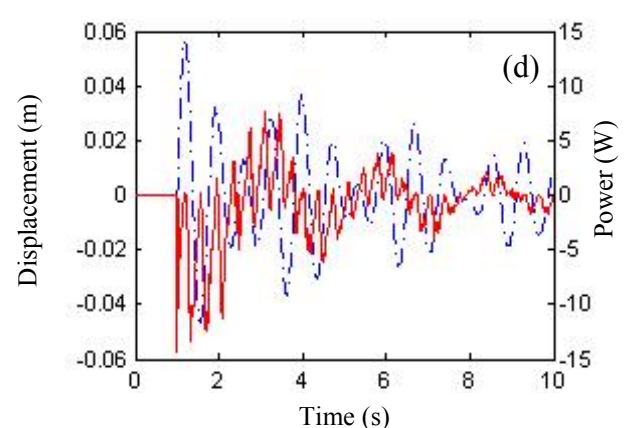
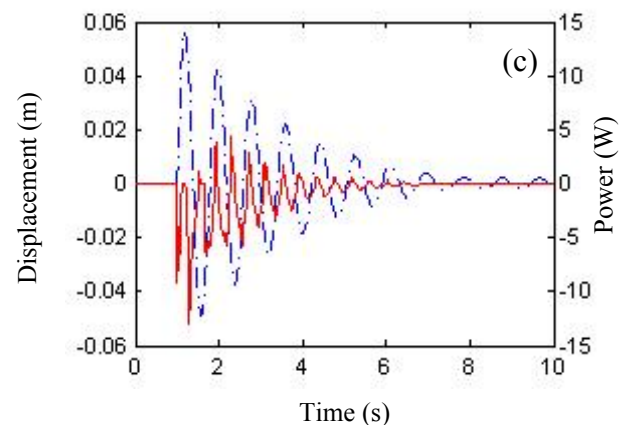
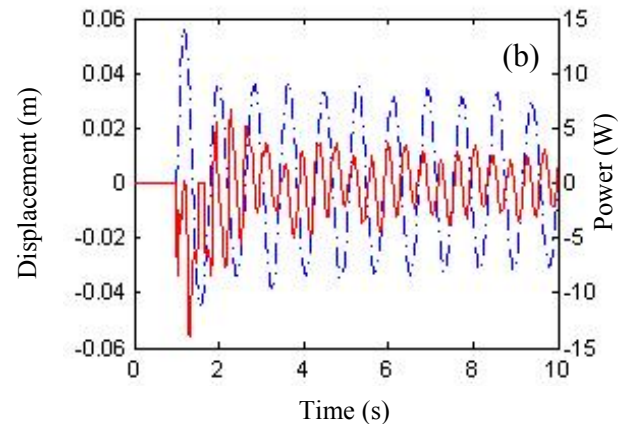
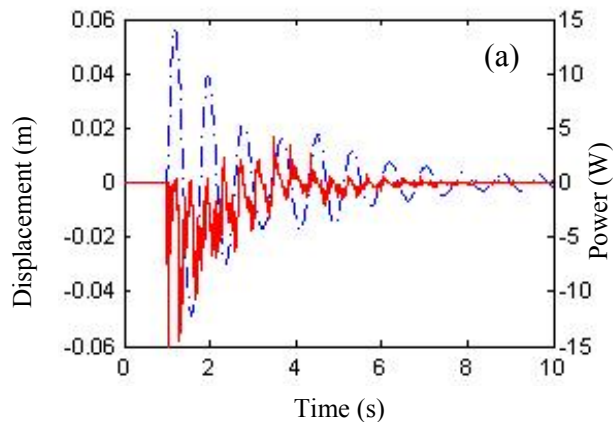


Figure 5.6. First 10 seconds of displacement (---) and fluid power (—) histories of the (a) tuned rectangular absorber, (b) cylindrical absorber, (c) trapezoidal damper with converging walls at an angle of 30 degrees and 0.2 m free surface and (d) trapezoidal damper with diverging walls at an angle of 30 degrees and 0.2 m free surface.

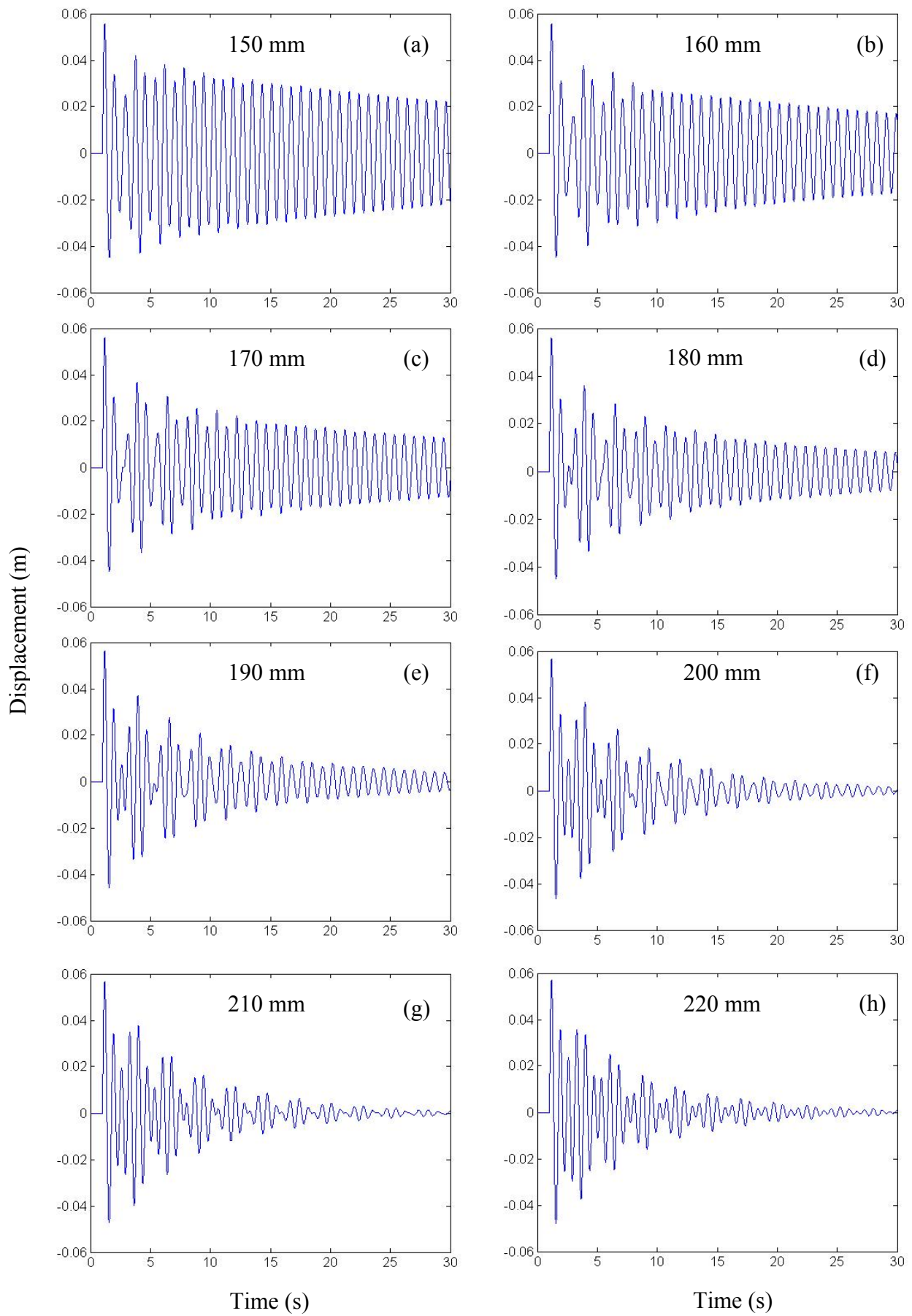


Figure 5.7. Continued over page.

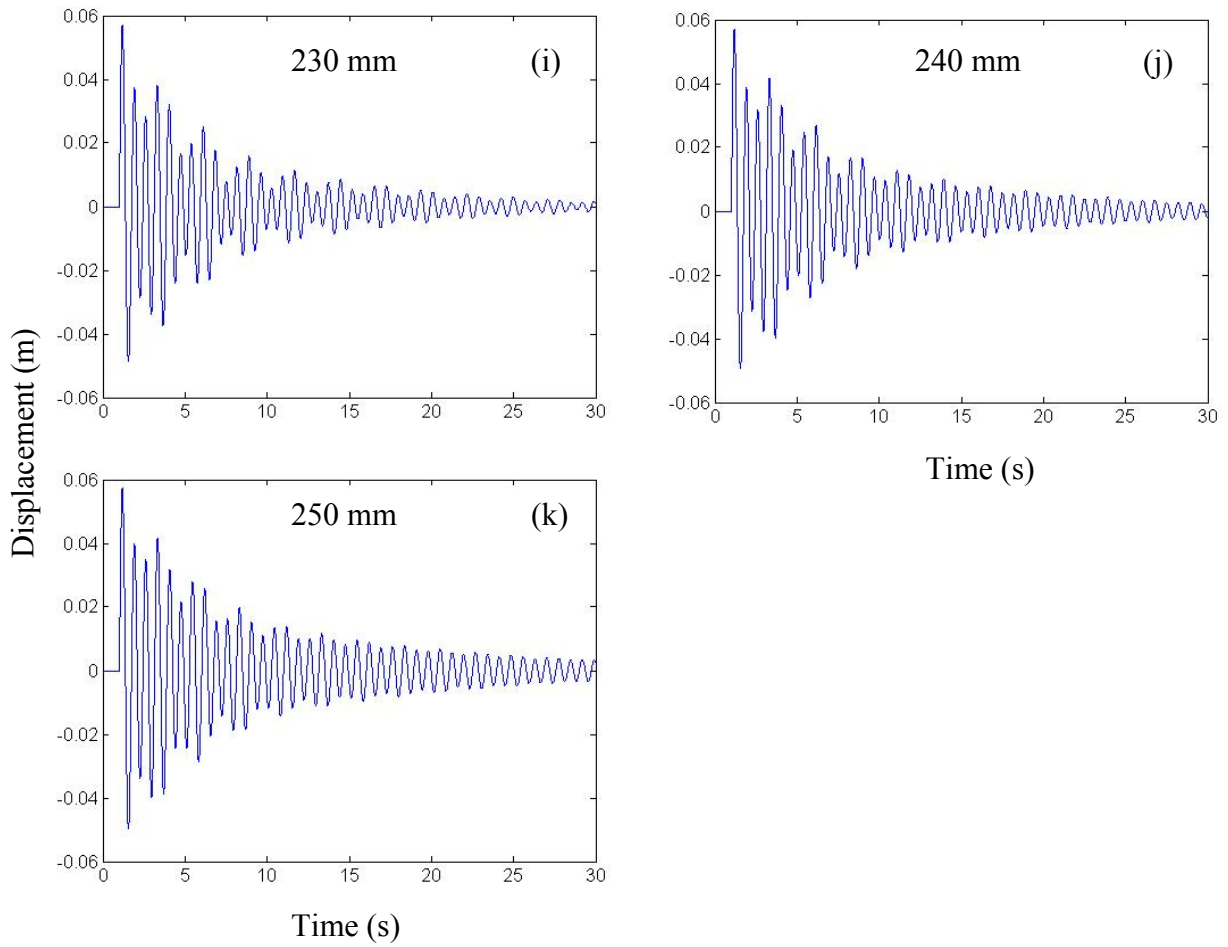


Figure 5.7. Displacement histories with a trapezoidal absorber of 30 degree diverging walls and free surface length of (a) 150 mm, (b) 160 mm, (c) 170 mm, (d) 180 mm, (e) 190 mm, (f) 200 mm, (g) 210 mm, (h) 220 mm, (i) 230 mm, (j) 240 mm and (k) 250 mm.

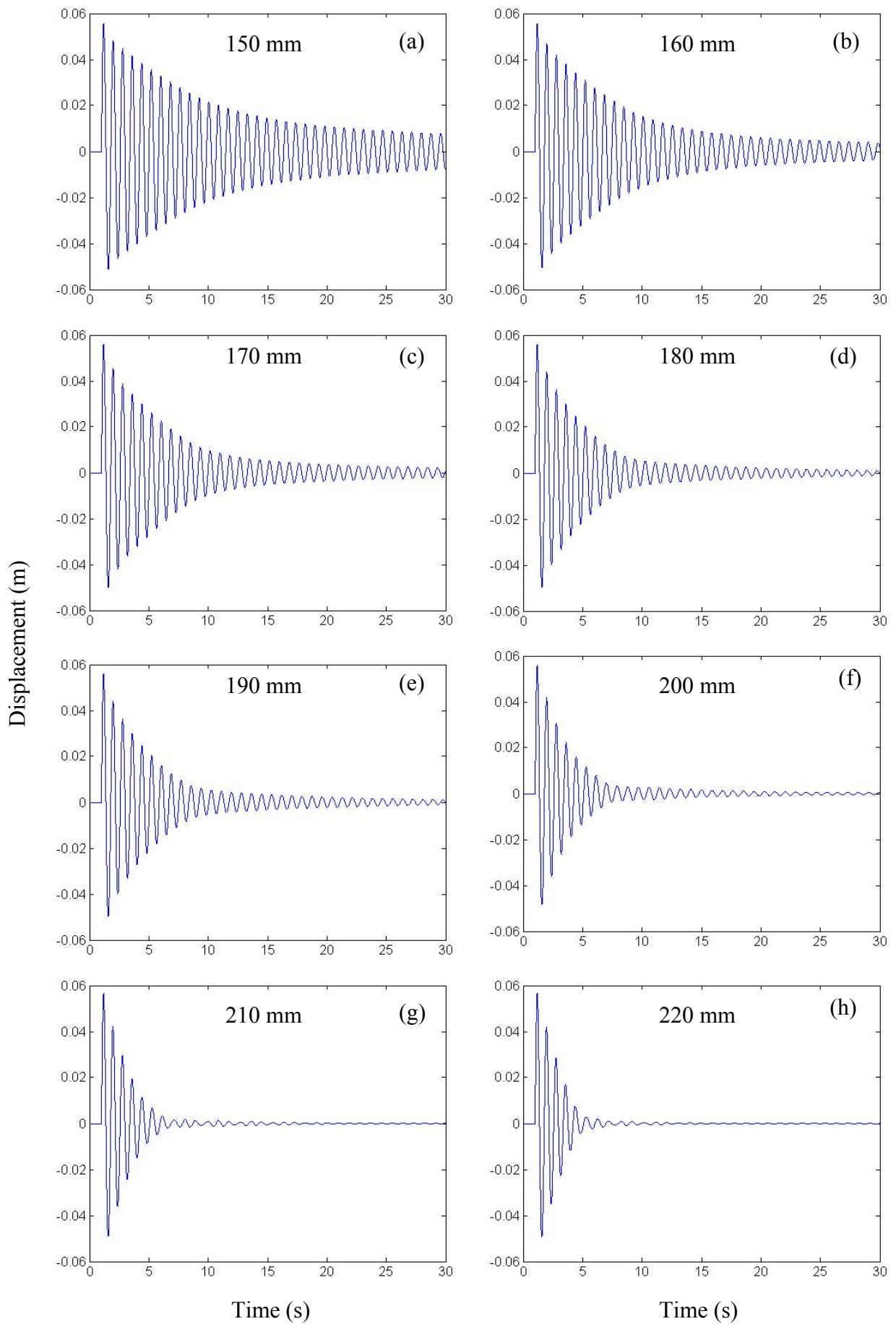


Figure 5.8. Continued over page.

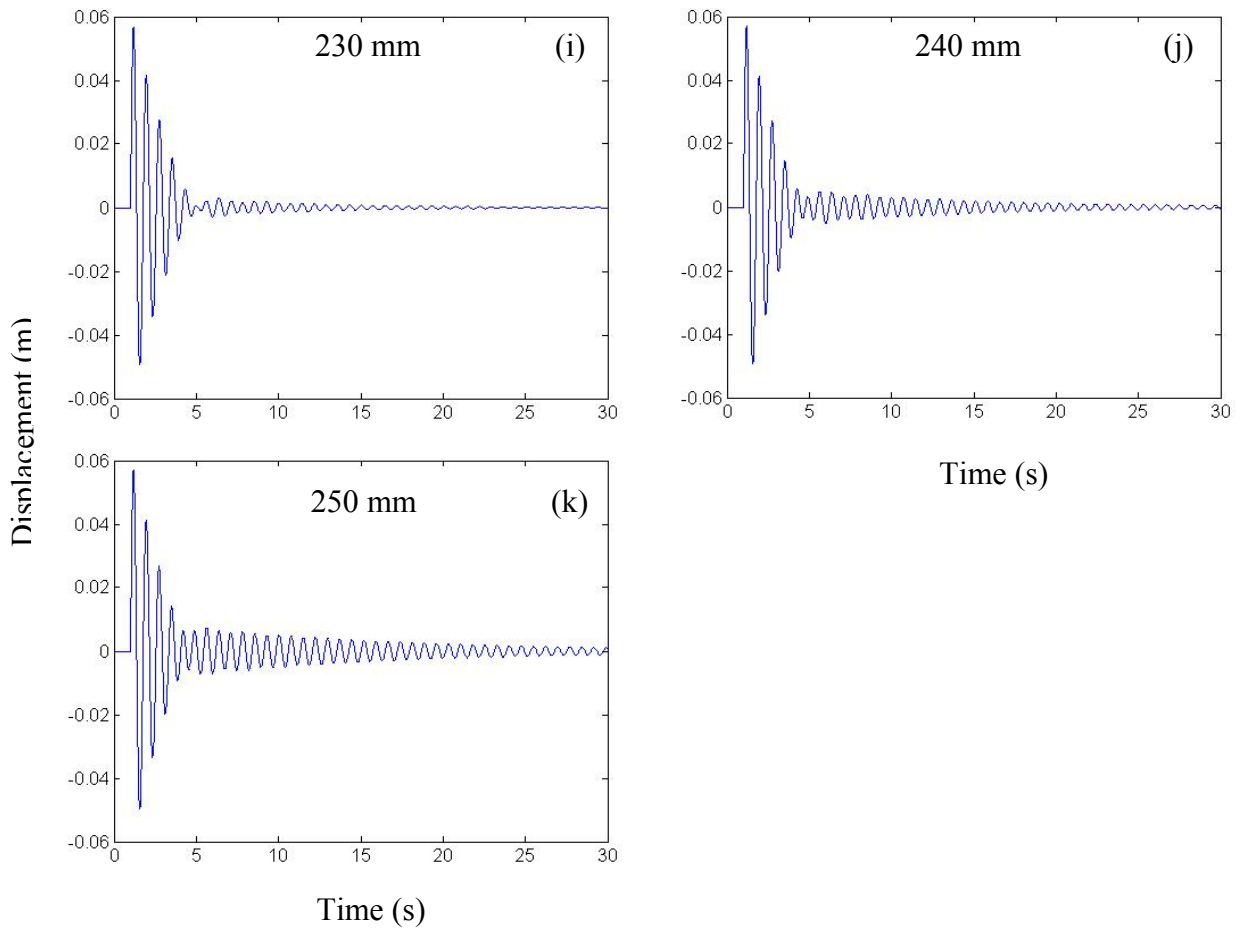


Figure 5.8. Displacement histories with a trapezoidal absorber of 30 degree converging walls and free surface length of (a) 150 mm, (b) 160 mm, (c) 170 mm, (d) 180 mm, (e) 190 mm, (f) 200 mm, (g) 210 mm, (h) 220 mm, (i) 230 mm, (j) 240 mm and (k) 250 mm.

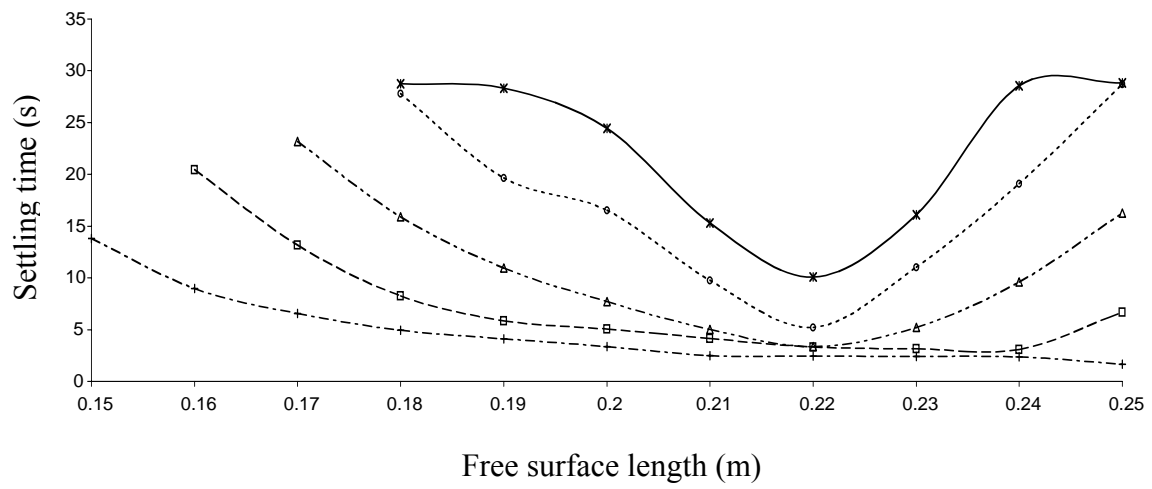


Figure 5.9. Variation of the settling time with free surface length for 30 degree converging walls. Residual levels of structural displacement as a percentage of the maximum are indicated as 1% (*), 2% (o), 5% (□), 10% (◻) and 25% (+).

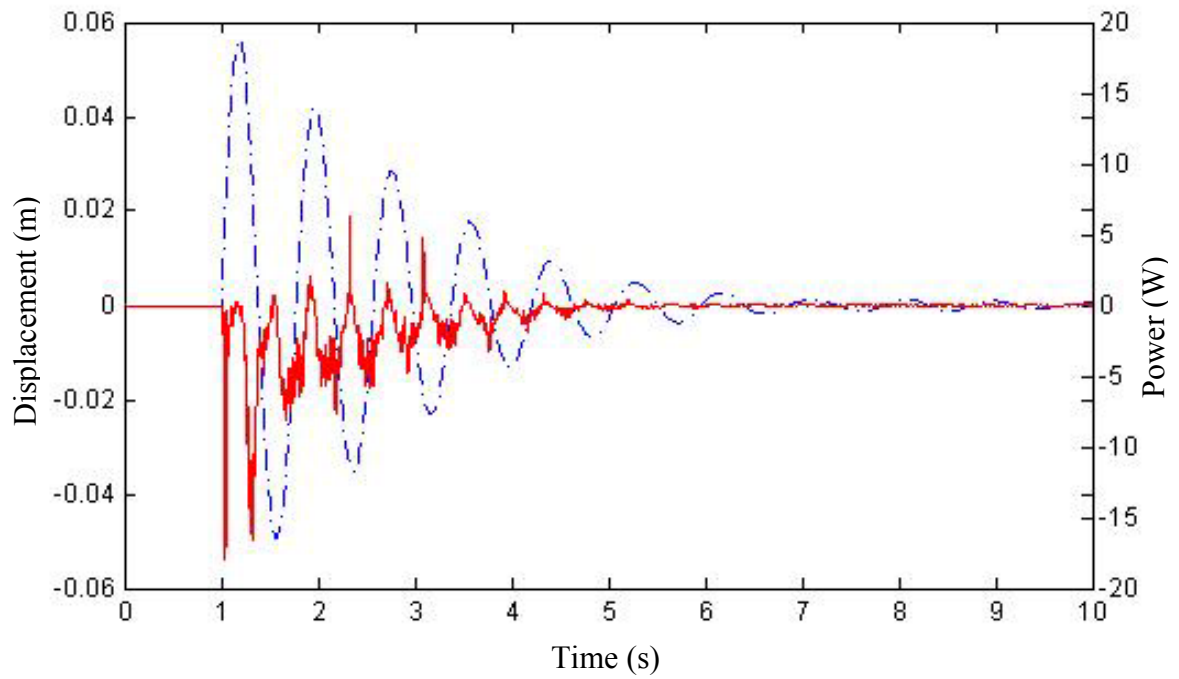


Figure 5.10. First 10 seconds of displacement and fluid power histories of the trapezoidal damper with converging walls at an angle of 30 degrees and 0.22 m free surface length.

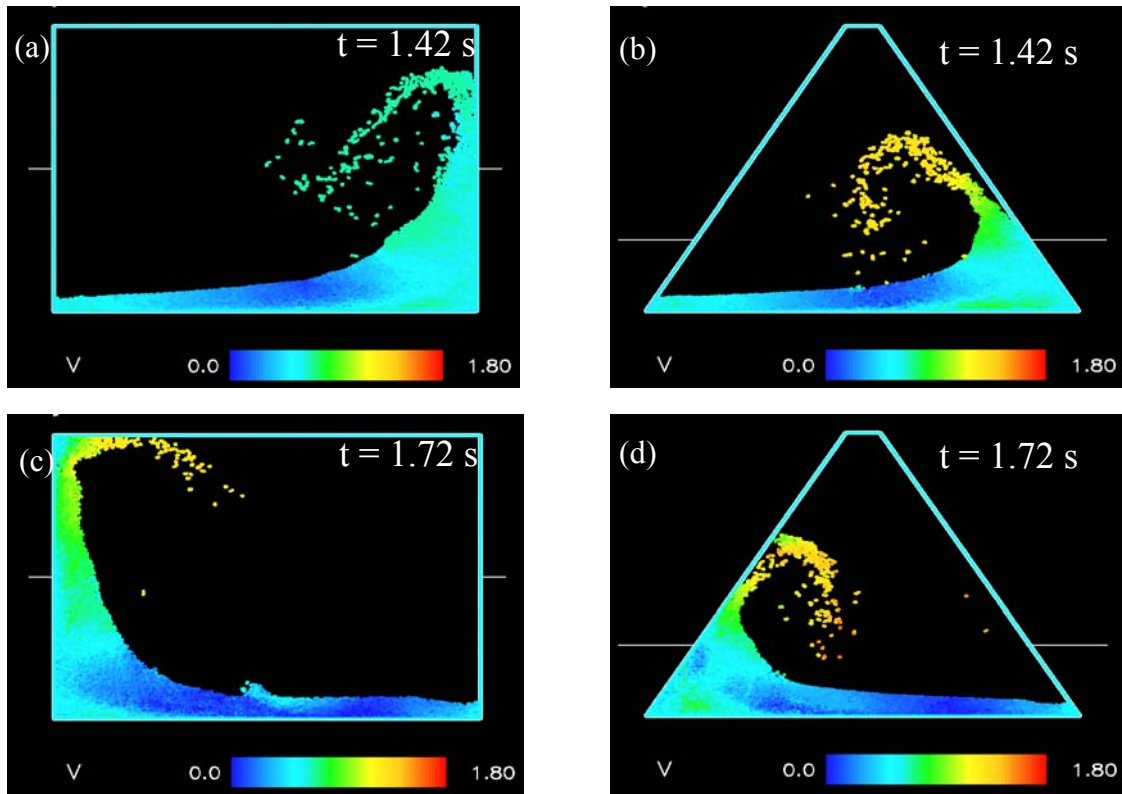


Figure 5.11. Still frames at instances of interest within the tuned rectangular absorber in the left hand column and the tuned converging trapezoid in the right hand column. Fixed colour scale represents fluid velocity (m/s).

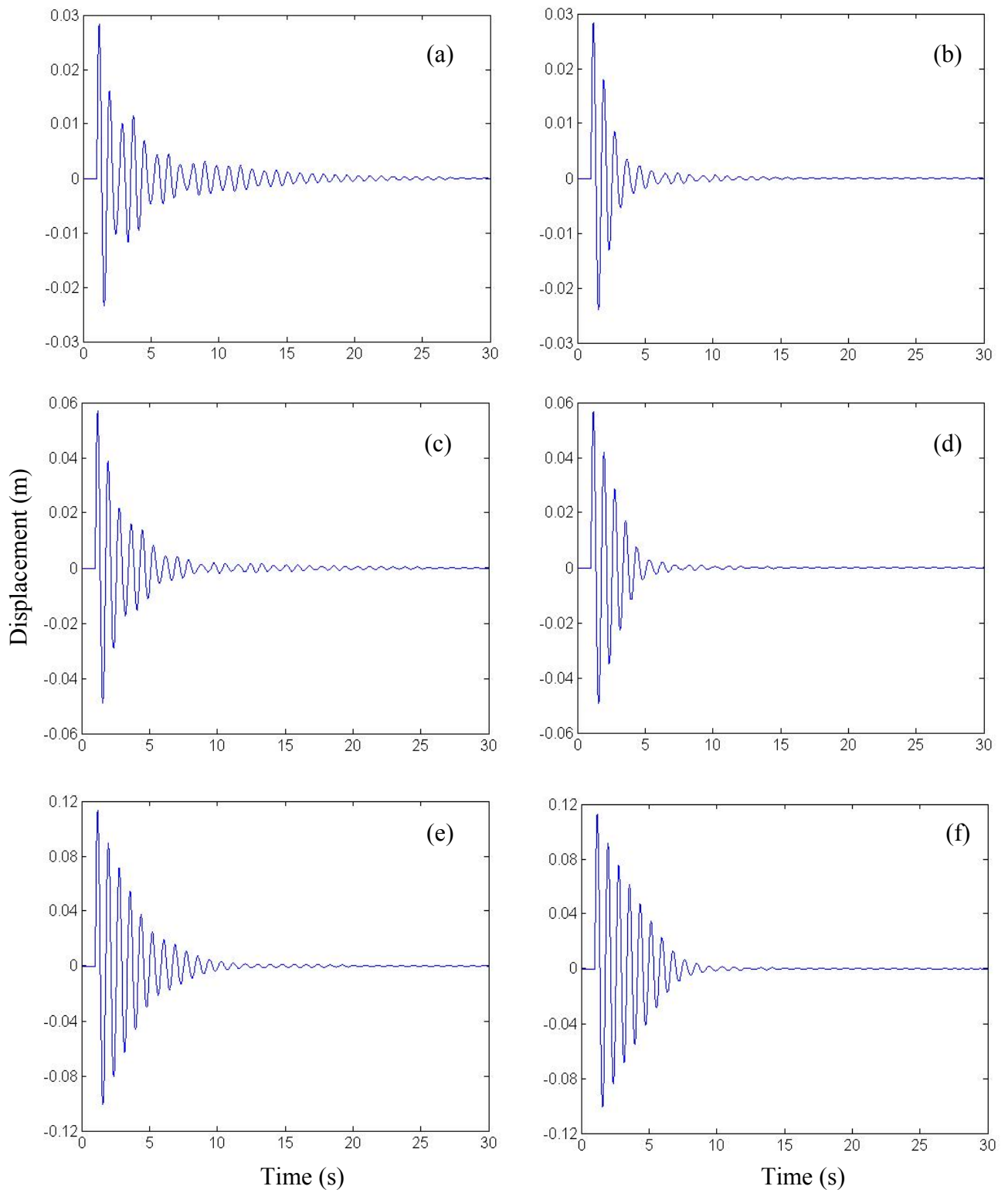


Figure 5.12. Effect of varying the excitation magnitude on the tuned rectangular absorber (left column) and the tuned converging trapezoid (right column). Initial velocity magnitudes of (a) and (b) 0.25 m/s, (c) and (d) 0.5 m/s and (e) and (f) 1.0 m/s. Y-axis scale changes down the page.

Chapter 6

A STUDY OF THE DYNAMICS OF A NATURAL SLOSHING ABSORBER : THE HEN'S EGG

6.1 Introduction

In this chapter, the novel concept of using the geometry of a hen's egg to control structural oscillations is explored. The hen's egg has evolved for the purpose of dissipating vibration energy quickly to protect its contents, the embryo. Its shape may therefore prove to be highly effective for controlling structural oscillations.

Limited studies of the effect a sloshing absorber's shape has on its control performance have been completed (Marsh at al., 2009c). For this reason, an 'ideal' geometry is still unknown. As a result, practical applications have been limited mainly to rectangular (Koh at al., 2007), cylindrical (Ikeda and Ibrahim, 2005) and toroidal shapes (Tamura at al., 1996). The lack of a comprehensive investigation on the shape of a sloshing absorber is the motivation to study the sloshing of the raw content of a hen's egg.

Energy dissipation within a hard-boiled egg is significantly poorer than that in an egg with raw content. This assertion can be easily confirmed by releasing an egg before and after boiling it from a position where its long axis is vertical, and observing how long it takes to come to rest. The results of such an observation are shown in Figure 6.1 (So and Semercigil, 2004). The hard-boiled egg takes about 10 times longer to come to rest than the case with raw content. The only significant change boiling induces, is to eliminate the sloshing of the liquid content, causing the reduction in the rate dissipation of the initially imposed potential energy.

Within a raw egg, the albumen (white) and yoke are held separate by membranes, as shown in Figure 6.2. Moreover, the yoke is suspended within the albumen with ties (chalazae). Therefore, the yolk and white are able to slosh out of phase with one another, and out of phase with the oscillations of the egg-shell. It is possible that this type of relative motion is responsible for the egg's high mechanical damping. However, it has been reported by So and Semercigil, that extracting the content, scrambling, and reintroducing it into the egg-shell somewhat improves the energy dissipative characteristics of the egg even further.

Such an observation makes the study of the liquid motion inside the egg promising. Another marginal increase in dissipation has been reported by replacing the scrambled content with water. One last significant observation in the performance of energy dissipation has been reported for different volume content of water inside the egg. Different volume fractions produce comparable stopping times of shell's oscillations. Such an insensitivity to varying liquid levels, is a desirable characteristic of a sloshing absorber from a design point of view.

The primary objective of this work is to numerically demonstrate the egg's ability to effectively dissipate energy via sloshing of its liquid content. Smoothed Particle Hydrodynamics (SPH) is used to model fluid-structure interaction between an egg-shaped cylinder (representing the hen's egg in two dimensions) and the surface on which the egg oscillates. SPH predictions are compared to observations from simple experiments to demonstrate the ability to predict such flows meaningfully. A limited case study is also presented, exploring the possibility to improve the energy dissipative qualities of an egg.

6.2 Numerical model and procedure

Smoothed Particle Hydrodynamics (SPH) is used to model fluid-structure interaction between an egg-shaped cylinder and the surface on which the egg oscillates. The same SPH code has been used here as that in chapter 2. Due to the inherent computational expense involved with 3 dimensional modelling, current prediction attempts have been limited to two dimensions. It is anticipated that ever-increasing computing capacities should soon remove such limitations.

The egg-shaped cylinder is represented by the geometry shown in Figure 6.3. The sloshing fluid within the 2D egg-shell is water with a density of 1000 kg/m^3 and dynamic viscosity of 0.001 Pa s . A particle size of $0.4 \text{ mm} \times 0.4 \text{ mm}$ is used to model the flat surface outside the shell, the shell and the water. This resolution is expected to be fine enough to capture an accurate prediction of the egg-shell motion, and fluid behaviour within. A particle size smaller than the ones presented earlier in this thesis is chosen here due to the more complicated geometry and smaller expected scales. Both the egg-shell and contact surface are represented by rigid boundaries. Time stepping is explicit. It is limited by the Courant condition modified for the presence of viscosity (Appendix1, Equation A15), and is bounded by $0.31 \mu\text{s}$, corresponding to around 3.8 million integration steps per period of egg-shell's oscillation. The total time of simulation is 25 s for all cases.

The egg-shell is put in an upright position and held for one second so that the water particles reach an initial state of rest. The egg is then released and allowed to respond dynamically, eventually coming to rest horizontally at the position of lowest potential energy. Friction between the shell and the surface is set to zero, so that energy dissipation is via the working fluid only.

6.3 SPH predictions

6.3.1 Natural egg

The predicted rotational histories of the egg-shell when filled to the volume fractions of 0.2, 0.4, 0.6, 0.8 and 1.0 are shown in Figures 6.4(a) to 6.4(e). Marginal improvement in performance is predicted with increasing volume fraction. However, egg-shell motion seems to be relatively insensitive to the amount of fluid within. This predicted behaviour agrees well with that observed experimentally (So and Semercigil, 2004).

Fluid oscillates periodically within the shell, and the nature of oscillations changes with volume fraction. At low volume fractions, large free surface deformations are predicted. Snapshots of some instants of interest with the lowest volume fraction of 0.2, are shown in Figures 6.5(a) to 6.5(d). The colour scale indicates the fluid velocity, with the maximum value of 0.4 m/s in red. Fluid behaviour is highly energetic. Travelling waves are generated easily, and their inherent steep velocity gradients are responsible for dissipating energy (Marsh et al., 2009a). This behaviour is predicted for even small surface deformations such as that shown in Figure 6.5(d) which occurs during the sixth cycle of oscillation.

In a rectangular container, the nature of fluid behaviour is highly dependent on excitation magnitude (Banjeri et al., 2000). Large excitations transfer large amounts of energy to the working fluid. Travelling waves at the free surface are generated easily. When the excitation is considered to be low, standing waves are generally seen, restricting the fluid's ability to dissipate energy. On the other hand, travelling waves are generated even with small shell displacements for the egg. At small volume fractions, the egg-shell transfers enough energy to maintain energetic free surface behaviour from the instant of release to eventually coming to rest. As a result, a high energy dissipation rate is preserved throughout. Such a quality is desirable for high rate of dissipation.

Snapshots of some instants of interest when the egg is filled to the highest volume fraction of 1.0 (an air pocket as indicated in Figure 6.2 is always maintained), are shown in Figures 6.5(e) to 6.5(h). Minimal free surface, restricts surface deformations and prevents the formation of travelling waves. There are no local areas of high fluid velocity, in contrast to the case of the 0.2 volume fraction. Instead, a relatively uniform velocity field is predicted throughout the fluid volume.

The lack of energetic free surface behaviour indicates that the egg is highly reliant on wall shear stress at the inside surface of the shell to dissipate energy. This shear stress occurs due to the existence of the no-slip condition at the walls. For the higher volume fractions, the egg clearly possesses more initial potential energy, as both the fluid mass and the centre of gravity increase at the instant of release. Therefore, coming to a stop over about same duration with those of lower volume fractions, indicates a higher rate of energy dissipation for a higher volume fraction case. Shear stress at the walls of the shell is, therefore, more important than energetic free surface behaviour for producing high mechanical damping.

6.3.2 A structural modification of the egg

Having gained some confidence on the reliability of the numerical predictions, the possibility of improving the rate of energy dissipation in an egg-shell through structural modifications, is explored next. This modification is introduced in the form of a fin, protruding from the bottom of the egg and extending along its long axis of symmetry, is shown in Figure 6.6(a). Fin height is varied from 0.2 to 0.6 of the long axis, with increments of 0.2.

The effect of a fin on the settling time of the egg, is shown in Figure 6.6(b). Settling time is defined as the time taken for the egg to come to rest from the instant of release. Hence, a short settling time indicates a fast rate of dissipation. The angular displacement histories of all cases are given in Appendix 6, for completeness.

In Figure 6.6(b), the dissipation performance of a finned profile is dependent on both volume fraction and fin length. At the low volume fraction of 0.2 (case 2, —), settling times are comparable to those of the natural shell (case 1, \diamond). An energetic free surface behaviour is observed here, similar to that of a no-fin case. Hence, the disturbance caused by the presence of the fin is minimal. However, the volume fraction increases (as the mechanism for energy dissipation changes from free surface motion to shear stress at the boundary), the presence of the fin causes fluid to stagnate in small compartments, disrupting the flow. As a result, shear stress is restricted, deteriorating the effectiveness of dissipation. The level of deterioration, seems to worsen with increasing lengths of the fin. The best performance is always observed with the natural egg.

6.3.3 Geometric scaling

The purpose of geometric scaling here is to identify how large the egg can become before its vibration characteristics change. Being the simplest scaling method, it is useful to know how meaningful the geometric scaling is, for practical applications of appreciable size. Predicted displacement histories of the scaled egg are shown in Figure 6.7. A volume fraction of 0.2 has been used.

The original 1:1 scale in Figure 6.7, corresponds to the dimensions given in Figure 6.3. At 2:1 scale, the egg's behaviour is almost exactly the same as that of the original scale, with 9 full cycles of oscillation before coming to a stop. At a 3:1 scale, however, the trend changes quite drastically. Only 4 full cycles are required to dissipate the initial potential energy, before coming to a stop. Hence, there is some significant potential to improve performance with size.

6.4 Experiments

The objective of the experiments presented in this section is to provide a comparison for the numerical predictions obtained with the two-dimensional the egg-cylinders. An end and an isometric view of the two-dimensional models built for the experiments are shown in Figure 6.8. Side walls are constructed from rigid plexiglass, these walls are connected by ordinary transparency film, the kind normally used for overhead projectors. The depth is 210 mm in z-direction. The side profile of the egg-shaped cylinder is that of the 2:1 scale of the egg, discussed in the preceding section. 2:1 scale is used to simplify construction, and to minimise the effects of manufacturing imperfections.

The egg cylinder is filled with water to a volume fraction of 0.2. It is then held in an upright position where its long axis is vertical and perpendicular to the floor, shown in Figure 6.8(a). The egg cylinder is then released, to experience transient oscillations until coming to rest at the position shown in Figure 6.8(b). The motion is recorded with a standard digital camera at 25 frames per second. Such a relatively slow frame rate is sufficient for capturing the motion of the cylinder whose natural frequency is around 1 Hz. The angle between the stationary surface and the egg cylinder's long axis, is then recorded by examining the video recording frame-by-frame. Experimentally recorded motion is accurate to within ± 0.04 s and ± 1 degree.

History of the angular displacements recorded from the experiments and predicted with the numerical model are given in Figure 6.9. Although the overall agreement is quite close, differences are observed in the peak displacements. Experimentally measured peak displacements are consistently smaller than those predicted, indicating a larger rate of energy dissipation than the model is able to predict. Higher rate of mechanical damping also manifests itself in smaller damped natural frequencies in the experiments, or longer natural periods of oscillation. This anomaly is not considered to be significant, as the numerical model was constructed to intentionally exclude the contact friction between the shell and the surface on which oscillations take place. Such a frictionless contact is not possible to obtain experimentally, although every precaution was taken to minimise the surface roughness. Along with this, the flexibility of the transparency film produces a damping effect in the fluid-structure interaction. This is not taken into consideration in the numerical model.

Although there is disagreement in the peak displacements, the predicted time taken for the egg cylinder to come to rest is comparable to that observed experimentally. Both cases come to rest at around 8 seconds. Only one additional cycle (of quite small amplitude) is predicted than those observed. The predicted frequency of oscillation of 0.85 Hz is still quite close to the experimentally observed frequency of 1 Hz. Therefore, SPH may be considered to provide a good representation of the egg cylinder's dynamic behaviour.

6.5 Conclusions

The nature's egg has evolved to protect its embryo, to dissipate oscillatory energy quickly to avoid harm in case of an external disturbance. The combination of the sloshing of the liquid content and the approximately ellipsoid shape of its shell, is responsible for this desirable performance. An egg-shaped vibration absorber holds great potential as an effective energy sink, to suppress excessive vibrations of light flexible structures.

A summary of extensive numerical case studies is presented in this paper to provide some insight into the ways in which rapid energy dissipation takes place in a raw egg. Modelling with SPH (Smoothed Particle Hydrodynamics) provides details which may be possible by experimental observations. It has been observed that the flow pattern within the egg is dependant on volume fraction of its liquid content. At low volume fractions, large free surface deformations, in the form of braking travelling waves, dissipate energy. At high volume fractions, free surface is calm. Shear stress at the shell walls, is the primary mechanism of energy dissipation. It is also observed that the transient response of the egg is relatively insensitive to its volume fraction of fill. This critical trend agrees well with earlier experimental work

Limited attempts to structurally modify the internal profile of the egg, suggest that it is quite unlikely that the natural egg profile can be improved significantly. However, there may be opportunities to increase the size of the shell, to enhance its performance. Finally, simple experiments performed within the context of the presented work, suggest that the accuracy of the numerically predicted energy dissipation is certainly acceptable.

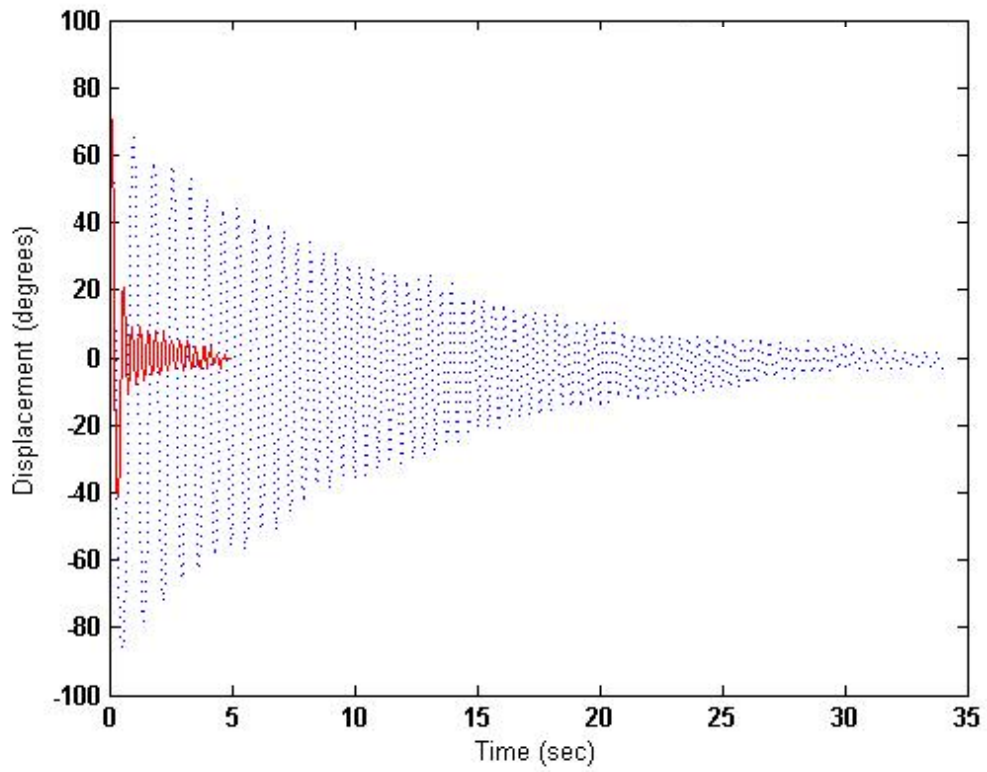


Figure 6.1. Angular displacement history of an egg after release when raw (—) and boiled (---). Results from So and Semercigil, 2004.

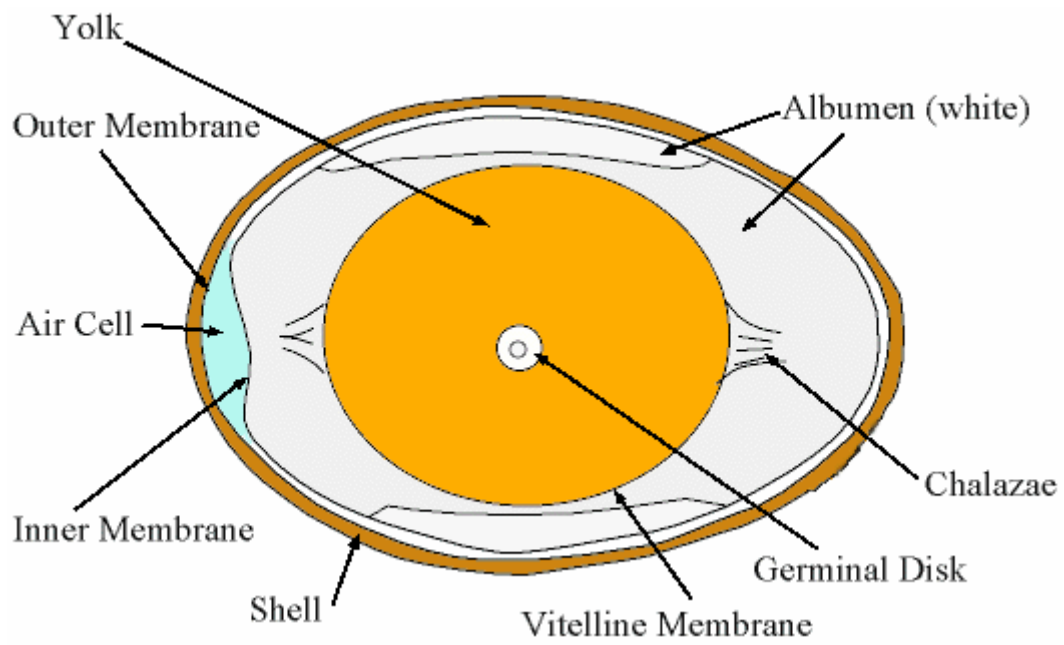


Figure 6.2. Schematic of hen's egg physiology, from Avian Sciences Net, 2009.

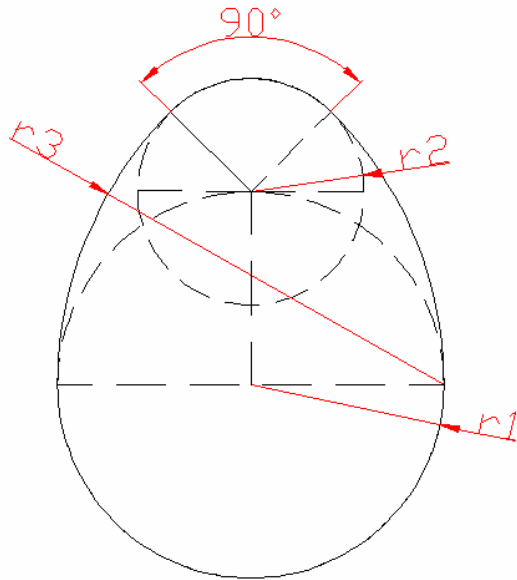


Figure 6.3. Schematic of the egg geometry from The Magic Egg, 2009. For an aspect ratio of 1.3, $r1 = 44.5$ mm, $r2 = 26$ mm and $r3 = 89$ mm.

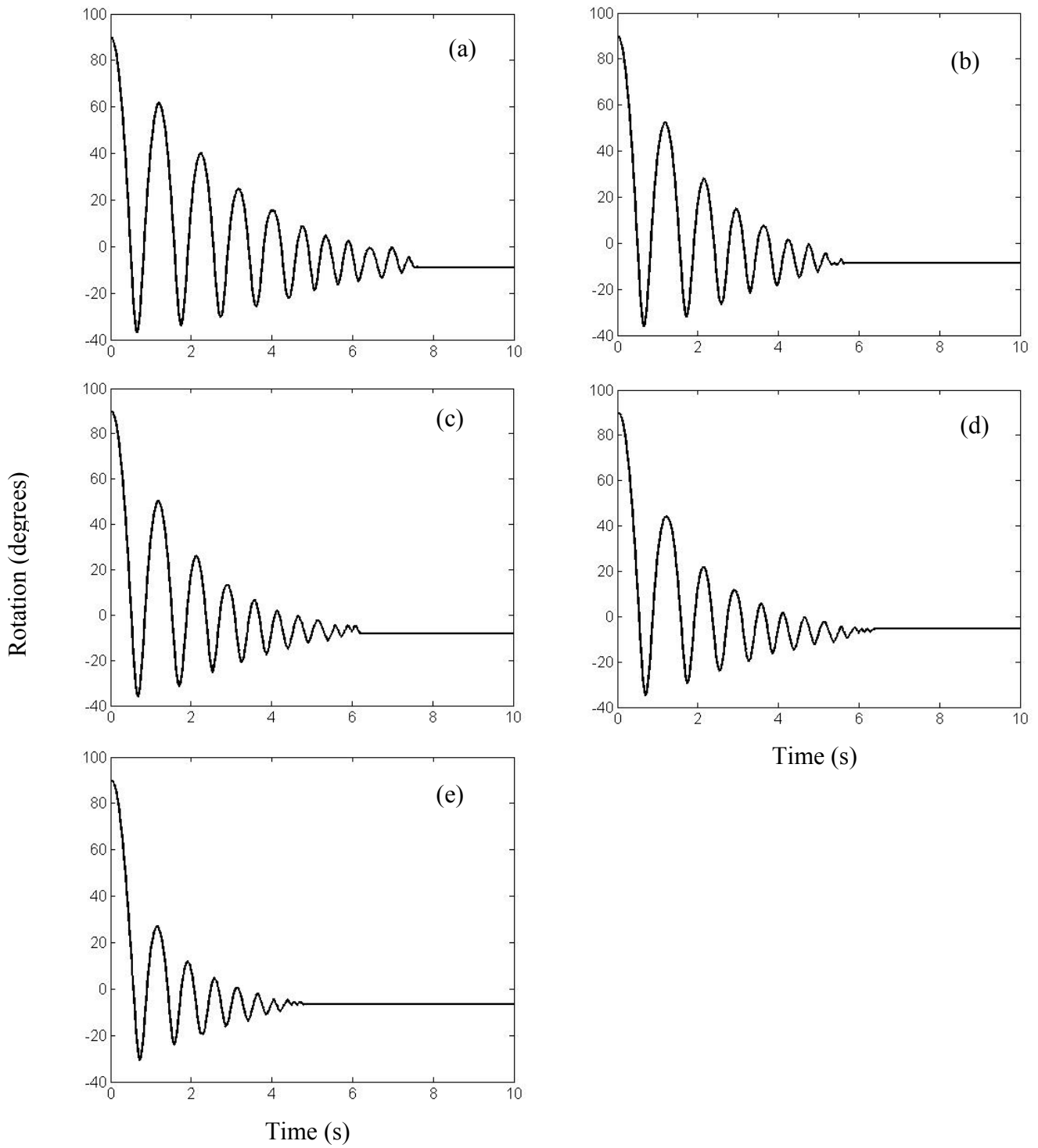


Figure 6.4. SPH prediction of the egg-shaped cylinder's motion when filled with water to volume fractions of (a) 0.2, (b) 0.4, (c) 0.6, (d) 0.8 and (e) 1.0. 1:1 scale to the hen's egg.

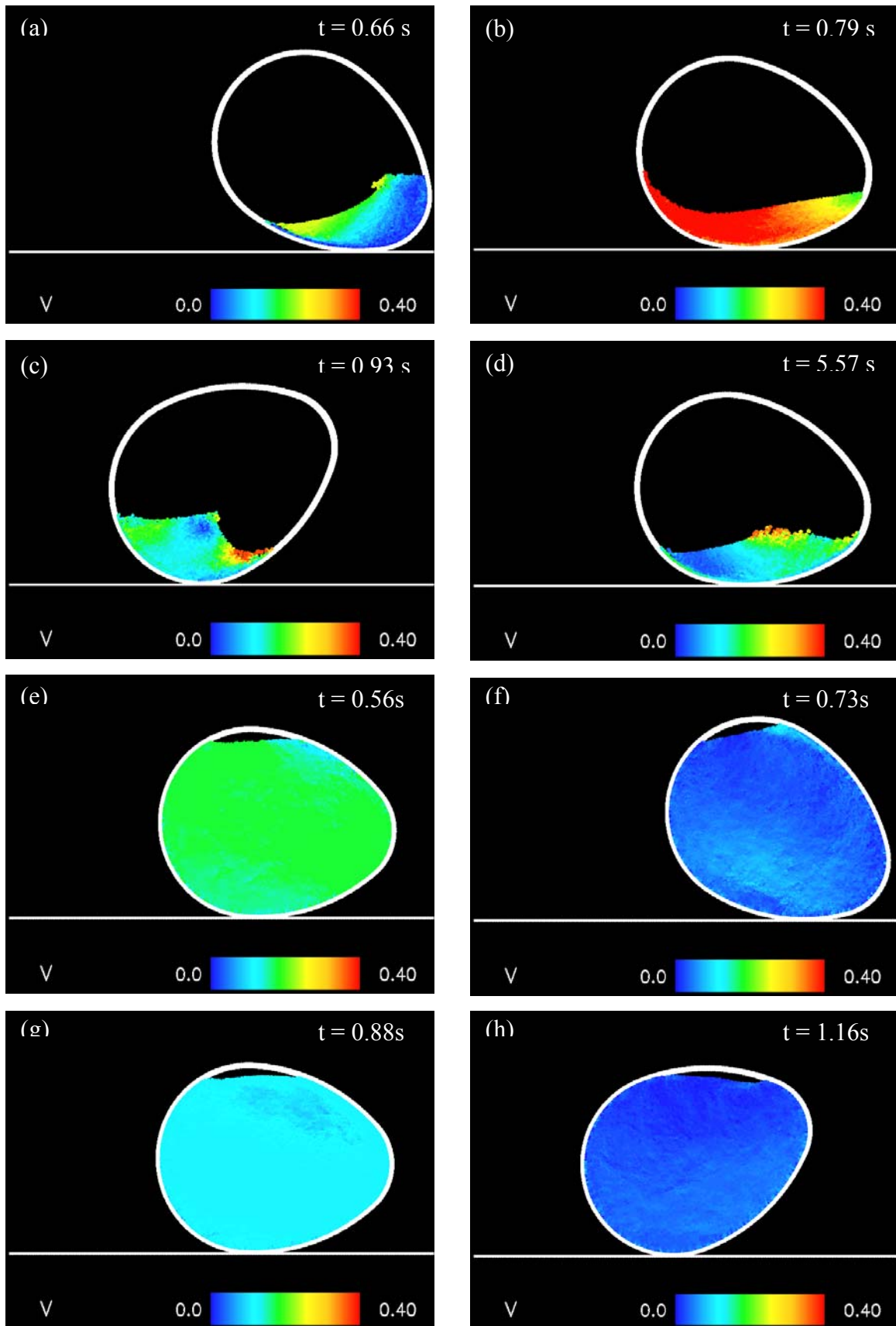


Figure 6.5. Snapshots of SPH predictions of instants of interest within the egg-shaped cylinder. (a) to (d) for volume fraction of 0.2 and (e) to (f) for volume fraction of 1.0. 1:1 scale to the hen's egg.

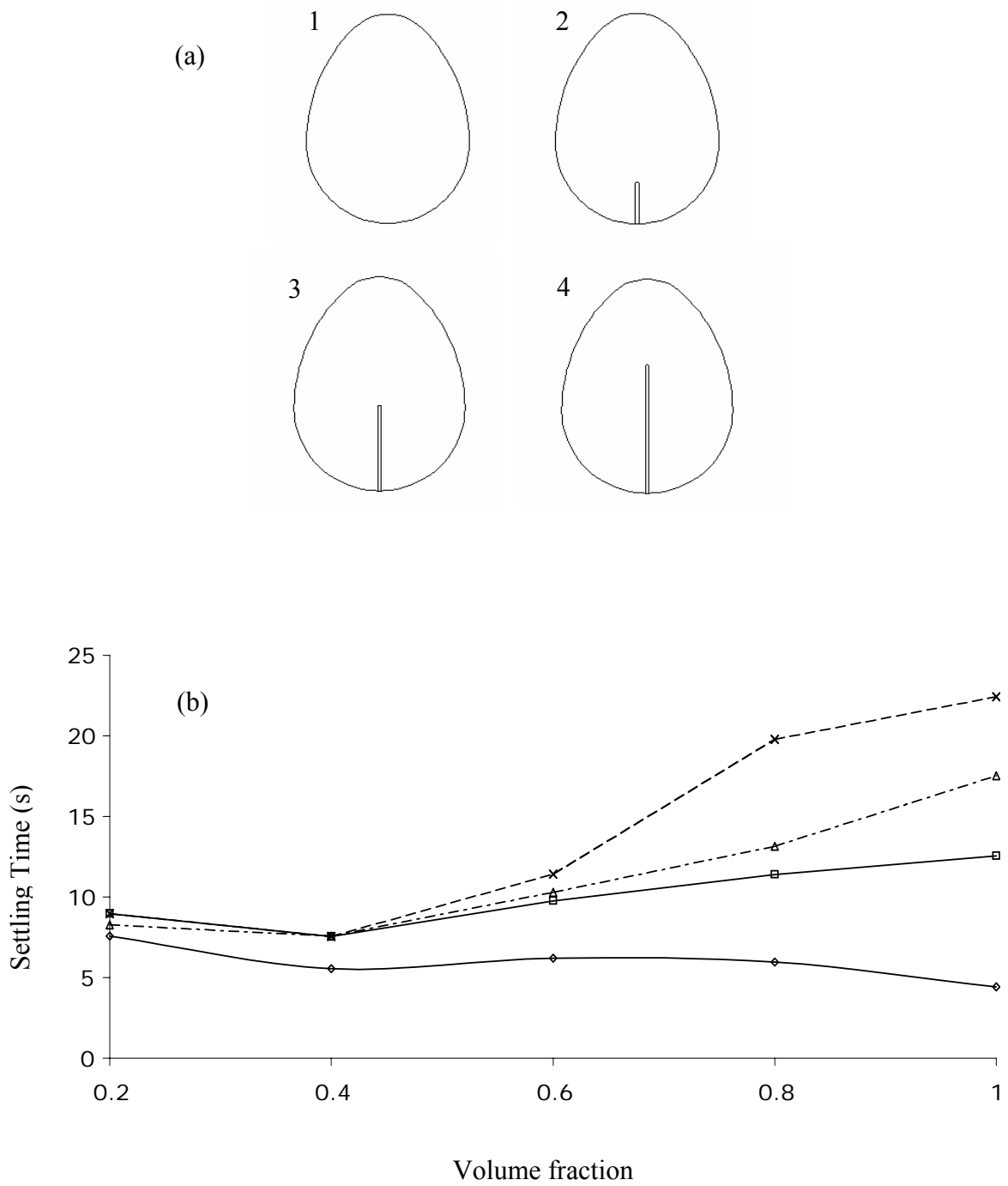


Figure 6.6. Showing (a) schematic of the fin geometries with the natural egg (1), and fin height fractions of 0.2 (2), 0.4 (3) and 0.6 (4); and (b) variation of settling time with volume fraction. Natural egg (◇), and fin height fraction of 0.2 (□), 0.4 (△) and 0.6 (×).

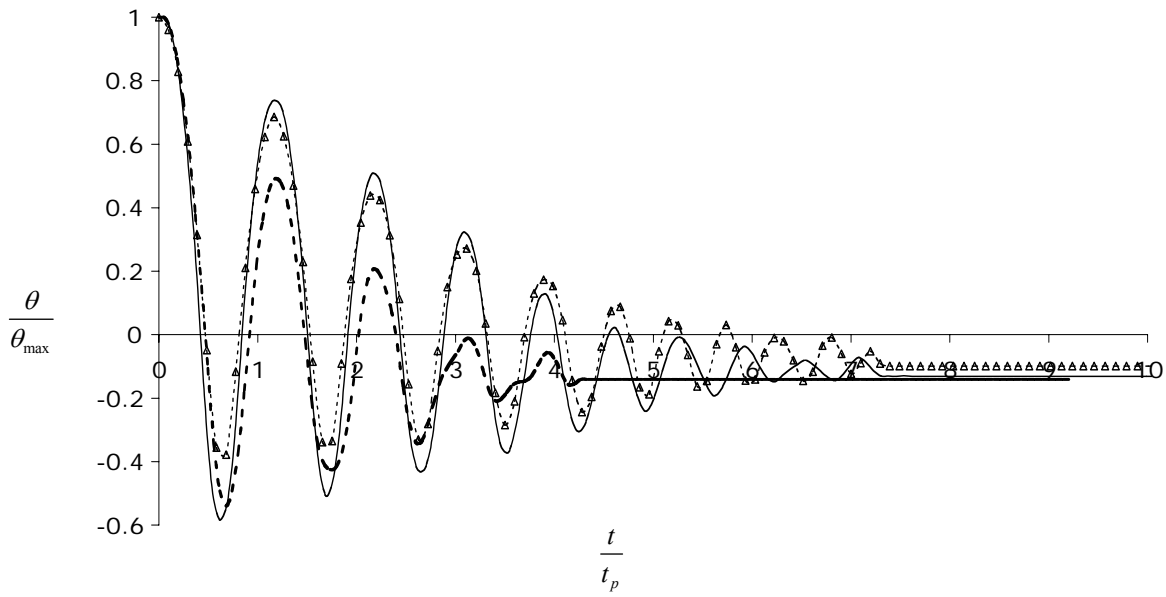


Figure 6.7. Oscillation histories for scales of 1:1 (···△···), 2:1 (—) and 3:1 (---) to that of the hen's egg. Angular displacement is normalised with initial displacement (θ_{max}), and time is normalised with natural period (t_p).

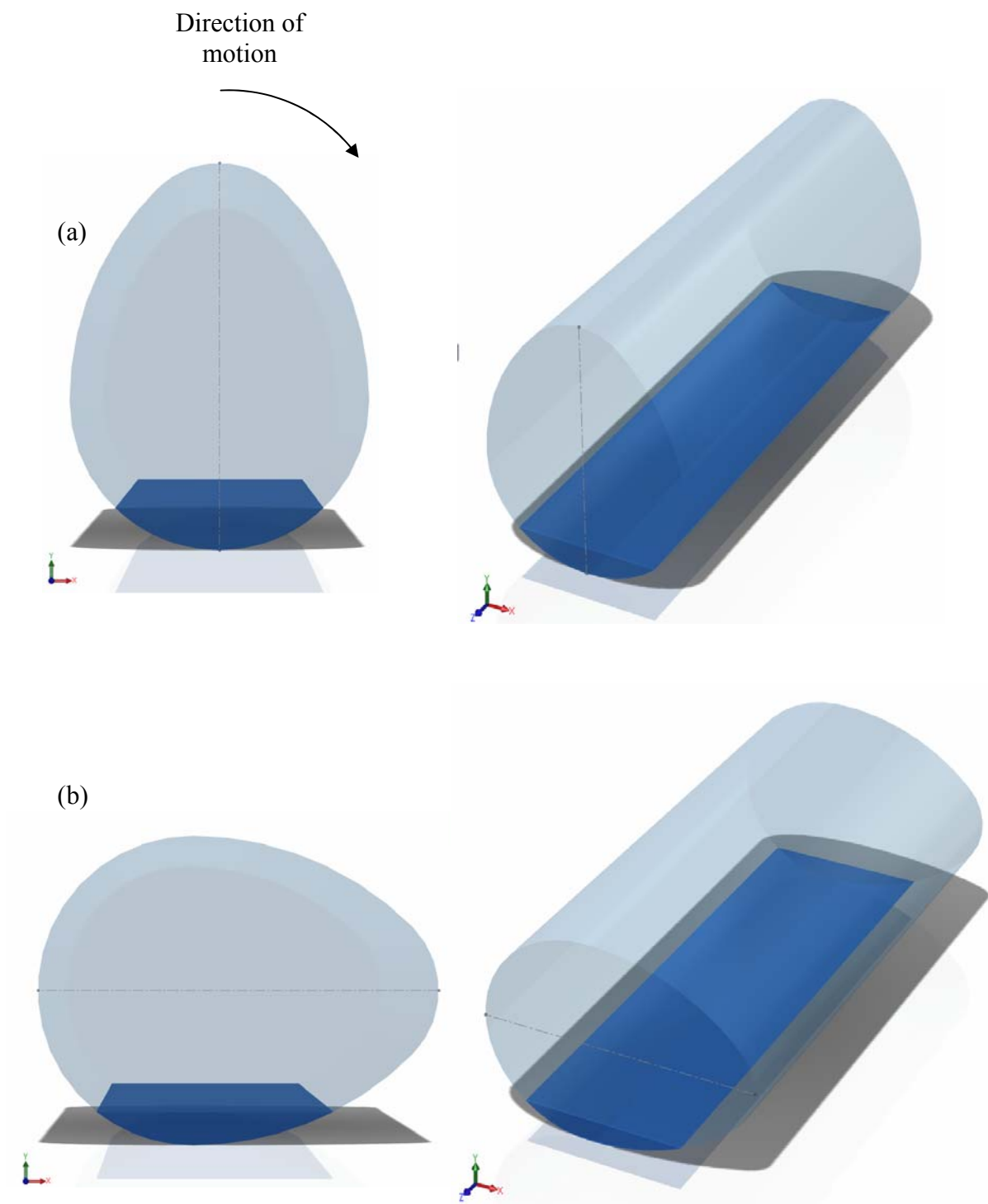


Figure 6.8. Graphical representation of (a) initial and (b) final rest positions.

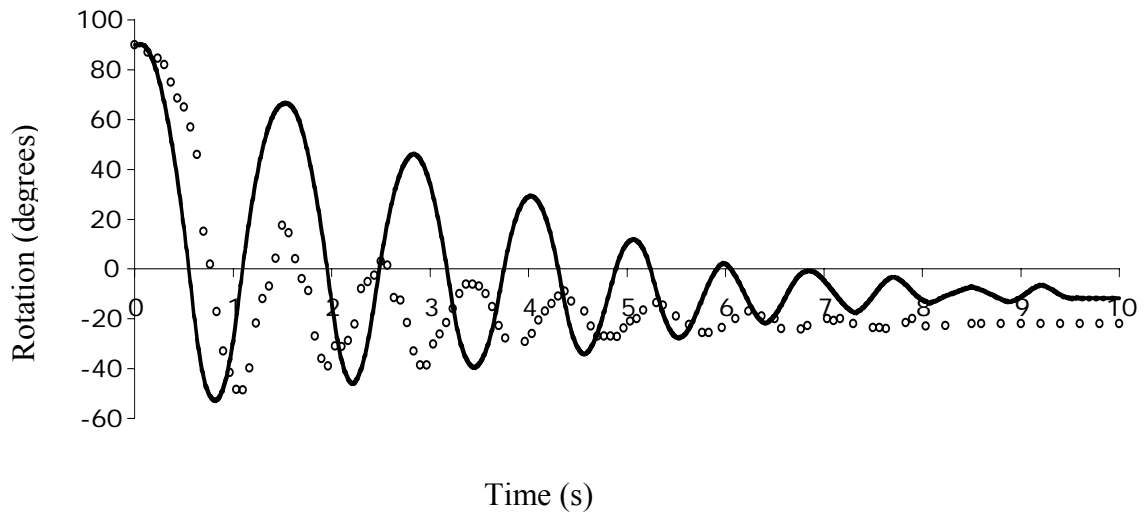


Figure 6.9. Displacement histories of experiments (o) and SPH predictions (—) of the 2:1 scale egg cylinder.

Chapter 7

CONCLUSION

The objective of the work presented in this thesis is to investigate the use of intentionally induced liquid sloshing to attenuate structural oscillations. The employment of shallow depths, as opposed to deep liquid levels, has been the focus of the work. The primary reason for this focus is the superior energy dissipation capability of travelling sloshing waves associated with shallow depths, in comparison to standing sloshing waves associated with deep liquid levels.

The numerical simulation results of the free surface behaviour of a sloshing fluid, are presented in Chapter 2. Experimentally observed displacement histories are imposed on the container of a sloshing absorber to predict the corresponding free surface kinematics using Smoothed Particle Hydrodynamics (SPH). Accurate predictions are obtained, when compared with experimental observations, for liquid depths as shallow as 5.5 mm. The accuracy of prediction increases with liquid depth. The significance of this chapter is in its establishing SPH as a promising modelling technique for predicting the physics of such free surface flows.

Case studies are presented in Chapter 3 to maximise the transfer of energy to sloshing liquid and its dissipation. The type of waveform produced within the container is primarily responsible for the energy dissipation characteristics. Travelling waves, produced in shallow depths, are effective energy dissipators. Standing waves, produced in deep liquid levels, dissipate energy at a much slower rate than travelling waves. Therefore, liquid depths should be chosen to produce travelling waves. A depth range in which this is achieved is discussed in Chapter 3. However, due to the non-linear nature of liquid sloshing, this depth range is expected to change when the nature, magnitude or frequency of the excitation varies. For a given liquid depth, an optimum energy transfer condition is reported with varying container length (also representing the wavelength of sloshing waves). The relationship between liquid depth, container length and excitation is expected to be important for achieving the maximum transfer and dissipation of energy.

In a sloshing absorber, the container of the absorber moves with the structure being controlled. In Chapter 4, SPH is demonstrated to adequately predict the inherent fluid-structure interaction forces, and the resulting dynamics of the structure to which the sloshing absorber is attached. However, in agreement with the findings of Chapter 2, the accuracy of the predicted free surface shapes depends upon the liquid depth.

The accuracy of the predicted structure motion is dependent on the nature of the fluid behaviour. Structural motion is predicted accurately when the fluid is energetic. When the fluid is calmer, excessive energy dissipation is predicted as compared to that observed experimentally. This dissipation results in a smaller predicted structural frequency, and smaller peak displacement amplitudes than those observed. Increasing the SPH smoothing length (from 1.2 to 2.4) corrects this discrepancy, without losing significant detail from the free surface. In Chapter 4, SPH is established for its broader ability of to reliably predict the full interaction between a structure and its sloshing absorber.

In Chapter 5, a series of container shapes are used to suppress oscillations of a resonant structure. The objective of this chapter is to explore potential enhancements, with some simple modifications of the shape, different than the usual rectangular container. Prior to the work reported in this chapter, a comparative study on the effect of different shapes could not be located in the literature. As expected, the control performance of a sloshing absorber is found to be highly dependent on its shape. Of the shapes analysed, two particular configurations are of most interest.

Orienting the walls of a rectangular geometry on a 30-degree inward angle (converging walls) enhances both the transfer of energy and its dissipation. In addition, the performance of a container with converging walls is relatively insensitive to variation of the magnitude of excitation which should prove to be a significant practical advantage.

Re-orienting the walls at a 30-degree outward angle (diverging walls) significantly increases the energy transfer between the structure and the fluid. However, the fluid is not capable of dissipating this energy rapidly enough, resulting in its being passed back to the structure. Due to this shape's exceptional ability to transfer energy, efforts to increase the rate of dissipation would be worthwhile for future work. Introducing roughness elements, or a porous medium at the container bottom are two possible ways of achieving such an increase.

The relatively complex geometry of a hen's egg is then considered in Chapter 6, as a container of a sloshing absorber. Sloshing within an approximately ellipsoidal cylinder, similar to a hen's egg, produces high mechanical damping. The oscillatory motion of the egg is relatively insensitive to its volume fraction of content. Yet, the flow patterns inside vary significantly depending on the amount of liquid. At low volume fractions, large free surface deformations (in the form of breaking and travelling waves) dissipate energy. At high volume fractions, the free surface is relatively calm, and the shear stress at the shell's walls, is the primary mechanism of energy dissipation.

Limited attempts to structurally modify the internal structure of the egg cylinder, suggest that it is quite unlikely that the natural egg profile can be improved significantly. These modifications disrupted the flow patterns required for energy dissipation, reducing the egg's effectiveness. Continued efforts should, therefore, be focused on employing the egg's original shape but to increase its efficiency to rapidly dissipate energy.

REFERENCES

Anderson, J.G., Semercigil, S.E., Turan, Ö.F. 2000. A Standing-Wave Type Sloshing Absorber to Control Transient Oscillations, *Journal of Sound and Vibration*, 232, 838-856.

Avian Sciences Net. 2009. <http://ag.ansc.purdue.edu/poultry/class.htm>. Accessed August 18, 2009.

Banjeri, B., Murudi, M., Shah, A.H., Poppelwell, N. 2000. Tuned Liquid Dampers for Controlling Earthquake Response of Structures, *Earthquake Engineering and Structural Dynamics*, 29, 587-602.

Batchelor, G.K. 1967. *An Introduction to Fluid Dynamics*. Cambridge University Press, Cambridge.

Bulian, G., Souto-Iglesias, A., Delorme, L., Botia-Vera, E. 2010. SPH Simulation of a tuned liquid damper with angular motion, *Journal of Hydraulic Research (SPH special issue)*.

Chanson, H. 1999. *The Hydraulics of Open Channel Flow: An Introduction*. Elsevier Butterworth-Heinemann, Oxford.

Cleary, P., Ha, J., Alguine, V., Nguyen, T. 2002. Flow modelling in casting processes, *Applied Mathematical Modelling*, 26, 171-190.

Cleary, P.W. 1998. Modelling confined multi-material heat and mass flows using SPH. *Applied Mathematical Modelling* 22, 981-993.

Cleary, P.W., Ha, J., Prakash, M., Nguyen, T. 2006. 3D SPH Flow Predictions and Validation for High Pressure Die Casting of Automotive Components, *Applied Mathematical Modelling*, 30,1406-1427.

Cleary, P.W., Prakash, M., Ha, J., Noui-Mehidi, M.N., Blackburn, H.M., Brooks, G. 2007b. Simulation of suspension of solids in a liquid in a mixing tank using SPH and comparison with physical modelling experiments, *Progress in Computational Fluid Dynamics*, 7, 91-100.

Cleary, P.W., Prakash, M., Ha, J., Stokes, N., Scott, C. 2007. Smooth Particle Hydrodynamics: status and future potential, *Progress in Computational Fluid Dynamics*, 7, 70-90.

Colagrossi, A., Palladino, F., Greco, M., Faltinsen, O.M. 2004. Experimental and Numerical investigation of 2D sloshing: scenarios near the critical filling depth. In *Proc. 19th International Workshop on Water Waves and Floating Body*, Cortona, Italy.

Colagrossi, A., Palladino, F., Greco, M., Faltinsen, O.M. 2006. Experimental and numerical investigation of 2D sloshing with slamming. In *Proc. 21st International Workshop on Water Waves and Floating Body*, Loughborough, England.

Delorme, L., Bulian, G., Mccue, L., Souto-Iglesias, A. 2006. Coupling between sloshing and ship roll motion: Comparison between nonlinear potential theory and SPH. 26th Symposium on Naval Hydrodynamics, Rome, Italy.

Faltinsen, O.M. 1993. Sea Loads on Ships and Offshore Structures, Cambridge University Press, Cambridge.

Gingold, R.A., Monaghan, J.J. 1977. Mon. Not. R. Astron. Soc., 181, 375.

Gomme, P.T., Prakash, M., Hunt, B., Stokes, N., Cleary, C., Owen, C.T., Bertolini, J. 2006. Effect of lobe pumping on human albumin: development of a lobe pump simulator using Smoothed Particle Hydrodynamics, Biotechnol. Appl. Biochem., 43, 103-111.

Gradinscak, M., Semercigil, S.E., Turan, Ö.F. 2002. Design of Flexible Containers for Sloshing Control, Proceedings of ASME FEDSM, Montreal, Quebec, Canada.

Guzel, B., Prakash, M., Semercigil, S.E., Turan, Ö.F. 2005. Energy Dissipation with Sloshing for Absorber Design, International Mechanical Engineering Congress and Exposition, IMECE2005-79838.

Ikeda, T., Ibrahim, R.A. 2005. Nonlinear random responses of a structure parametrically coupled with liquid sloshing in a cylindrical tank, Journal of Sound and Vibration, 284, 75-102.

Kaneko, S., Mizota, Y. 2000. Dynamic Modelling of Deepwater-Type Cylindrical Tuned Liquid Damper With a Submerged Net, *Journal of Pressure Vessel Technology*, 122, 96-104.

Kareem, A. 1990. Reduction of Wind Induced Motion Utilising a Tuned Sloshing Damper, *Journal of Wind Engineering and Industrial Aerodynamics*, 36, 725-737.

Koh, C.G., Mahatma, S., Wang, C.M. 2007. Theoretical and Experimental Studies on Rectangular Liquid Dampers under Arbitrary Excitations, *Earthquake Engineering and Structural Dynamics*, 23, 17-31.

Liu, G.R., Liu, M.B. 2003. *Smoothed Particle Hydrodynamics, a meshfree particle method*. World Scientific Publishing, Singapore.

Lu, M.L., Poppelwell, N., Shah, A.H., Chan, J.K. 2004. Nutation Damper Undergoing a Coupled Motion. *Journal of Vibration and Control* 10, 1313-1334.

Lucy, L.B. 1977. *Astron. J.*, 82, 1013.

Marsh, A., Prakash, M., Semercigil, S.E., Turan, Ö.F. 2009a. A Numerical Investigation of Energy Dissipation with a Shallow Depth Sloshing Absorber, *Applied Mathematical Modelling*, under review.

Marsh, A., Prakash, M., Semercigil, S.E., Turan, Ö.F. 2009c. A Study of Sloshing Absorber Geometry for Structural Control with SPH, *Earthquake Engineering and Structural Dynamics*, under review.

- Marsh, A.P., Prakash, M., Semercigil, S.E., Turan, Ö.F. 2007a. Numerical Investigation into Shallow Depth Sloshing Absorbers for Structural Control, 16th Australasian Fluid Mechanics Conference, Gold Coast, Australia.
- Milne-Thomson, L.M. 1968. Theoretical Hydrodynamics, Macmillan Press, London, 427-442.
- Modi, V.J., Munshi, S.R. 1998. An Efficient Liquid Sloshing Damper for Structural Control, *Journal of Fluids and Structures*, 12, 1055-1071.
- Modi, V.J., Welt, F., Seto, M.L. 1996. Control of Wind Induced Instabilities Through Application of Nutation Dampers: a brief overview, *Journal of Engineering and Structures*, 17, 626-638.
- Monaghan, J. J. 1992. Smoothed Particle Hydrodynamics. *Ann. Rev. Astron. Astrophys*, 30, 543-574.
- Monaghan, J.J. 1994. Simulating free surface flows in SPH, *Journal of Computational Physics*, 110, 399-406.
- Monaghan. J.J., Kos. A., Issa. N. 2003. Fluid Motion Generated by Impact, *Journal of Waterway, Port, Coastal, and Ocean Engineering*, 129, 250-259.
- Monaghan. J.J. 2005. Smoothed Particle Hydrodynamics, *Reports on Progress in Physics*, 68, 1703-1759.

- Murzyn, F., Chanson, H. 2007. Free Surface, Bubbly Flow and Turbulence Measurements in Hydraulic Jumps. Report CH63/07, Div. Of Civil Engineering, The University of Queensland, Brisbane, Australia. (IBSN 9781864998917).
- Popov, G., Sankar, S., Sankar, T. S. 1993. Dynamics of Liquid Sloshing in Baffled and Compartmented Road Containers, *Journal of Fluids and Structures*. 7, 803-821.
- Prakash, M., Cleary, P.W., Grandfield, J., Rohan, P., Nguyen, V. 2007. Optimisation of ingot casting wheel design using SPH simulations, *Progress in Computational Fluid Dynamics*, 7(2-4), Call No:2264.
- Rao, S. S. 1995. *Mechanical Vibrations (3rd Edition)*. Addison-Wesley Publishing Reading Mass.
- Reed, D.A., Yu, J., Yeh, H., Gardarsson, S. 1998. Investigation of tuned liquid dampers under large amplitude excitation, *Journal of Engineering Mechanics*, 124, 405-413.
- So, G. and Semercigil, S.E. 2004. A Note on a Natural Sloshing Absorber for Vibration Control, *Journal of Sound and Vibration*, 269, 1119-1127.
- Souto-Iglesias, A., Delorme, L., Rojas, L.P., Abril, S. 2006. Liquid moment amplitude assessment in sloshing type problems with SPH. *Ocean Engineering*, 33, 11-12.

Souto-Iglesias, A., Rojas, L.P., Rodriguez, R.Z. 2004. Simulation of anti-roll tanks and sloshing type problems with Smoothed Particle Hydrodynamics. *Ocean Engineering*, 31, 1169-1192.

Sturm, T.W. 2001. *Open Channel Hydraulics*. McGraw-Hill, New York.

Sun, L.M., Fujino, Y. 1994, A Semi-Analytical Model for Tuned Liquid Damper (TLD) with Wave Breaking. *Journal of Fluids and Structures* 8, 471-488.

Tait, M. J., El Damatty, A. A., Isyumov, N., Siddique, M. R. 2005, Numerical Flow Models to Simulate Tuned Liquid Dampers (TLD) with Slat Screens. *Journal of Fluids and Structures* 20, 1007-1023.

Tamura, Y., Kohsaka, R., Nakamura, O., Miyashita, K., Modi, V.J. 1996. Wind-induced responses of an airport tower – efficiency of a tuned liquid damper, *J. of Wind Engineering*, 65, 121-131.

The Magic Egg. 2009. <http://www.mathlove.com/new3/products/docs/PZL05.pdf>, Accessed August 18, 2009.

White, F. 2003. *Fluid Mechanics*. McGraw-Hill, New York.

Appendix 1

SMOOTHED PARTICLE HYDRODYNAMICS

In this appendix, the Smoothed Particle Hydrodynamics (SPH) method is introduced, and a brief description is given. The method was first developed by Gingold and Monaghan, 1977, and independently by Lucy, 1977.

Smoothed Particle Hydrodynamics (SPH) is a mesh-free particle method (MPM) of modelling fluid flows. The fluid being modelled is discretized into fluid elements or particles, the properties of which are attributed to their centres. SPH is a Lagrangian continuum method used for solving systems of partial differential equations. The method works by tracking particles and approximating them as moving interpolation points. These fluid particles (or moving interpolation points) have a spatial distance over which field variables such as density, velocity and energy are smoothed. This is achieved via an interpolation kernel function.

The fundamental concept of the integral representation of a function used in the SPH method comes from the identity shown in Equation (A1). The identity implies that a function of x , $f(x)$, can be represented in integral form. $\delta(x - x')$ is the dirac delta function in Equation (A1). V is the volume of the integral that contains x .

$$f(x) = \int_V f(x') \delta(x - x') dx' \quad (\text{A1})$$

The integral representation in Equation (A1) is exact, since the delta function is used, providing that $f(x)$ is defined and continuous in V (Liu and Liu, 2003). In SPH, the dirac delta function is replaced by the smoothing function $W(x-x',h)$ so that the integral representation of $f(x)$ is specified as:

$$\langle f(x) \rangle = \int_V f(x')W(x-x',h)dx' \quad (\text{A2})$$

where W is the interpolation kernel, h is the smoothing length that defines the region in which the smoothing function operates. Throughout the work presented in this thesis, a smoothing length of 1.2 times the particle separation has been used unless otherwise stated. The particle separation is equal to the particle length in one direction. A cubic smoothing kernel is used with $W(x-x',h)$, the shape of a Gaussian profile is approximated having compact support, so that $W(x-x',h)=0$ for $x-x'>h$.

The integral representation of the spatial derivative of a function in SPH is performed in the same way. $f(x)$ is substituted for $\nabla \cdot f(x)$ in Equation (A2) to produce:

$$\langle \nabla \cdot f(x) \rangle = \int_V \nabla \cdot f(x')W(x-x',h)dx' \quad (\text{A3})$$

From the identity in Equation (A4) below, Equation (A5) is obtained.

$$[\nabla \cdot f(x')]W(x-x',h) = \nabla \cdot [f(x')W(x-x',h)] - f(x') \cdot \nabla W(x-x',h) \quad (\text{A4})$$

$$\langle \nabla \cdot f(x) \rangle = \int_V [\nabla \cdot f(x')W(x-x',h)] dx' - \int_V f(x') \nabla \cdot W(x-x',h) dx' \quad (\text{A5})$$

The first integral on the right hand side of Equation (A5) is converted using the divergence theorem of Gauss to obtain Equation (A6).

$$\langle \nabla \cdot f(x) \rangle = \int_S f(x')W(x-x',h) \cdot \bar{n} dS - \int_V f(x') \nabla \cdot W(x-x',h) dx' \quad (\text{A6})$$

S is the surface of the integration domain V . \bar{n} is the unit normal to the domain surface S . When the support domain of W is located within the problem domain, the first integral on the right hand side of Equation (A6) is zero. However, when the support domain overlaps with the problem domain, W is truncated by the problem domain boundary. Hence, the surface integral is no longer zero. For all points in space whose support domain lies within the problem domain, Equation (A6) is simplified to Equation (A7).

For all other points in space, modifications need to be made to treat the boundary effects if the surface integral is to be equated to zero (Liu and Liu, 2003).

$$\langle \nabla \cdot f(x) \rangle = - \int_V f(x') \nabla \cdot W(x-x',h) dx' \quad (\text{A7})$$

Equation (A7) states that the spatial gradient of a function is determined from the values of the function and the derivative of the smoothing function, rather than the derivative of the function itself.

Discretization is performed by converting the integral representations in Equations (A2) and (A7) into summations over all the particles that lie within the support domain of W . This is achieved by replacing the infinitesimal volume dx' by the finite volume of particle j , ΔV_j . The mass of particle j (m_j) is then related to this volume by:

$$m_j = \rho_j \Delta V_j \tag{A8}$$

where ρ_j is the density of particle j . The discretized particle approximation can then be written as:

$$\langle f(x_i) \rangle = \sum_{j=1}^N \frac{m_j}{\rho_j} f(x_j) W(x_i - x_j, h) \tag{A9}$$

Equation (A9) states that the value of a function at particle i is approximated using the average of the same function at all j particles within the support domain of particle i , weighted according to the smoothing function.

The same approach is used to produce the particle approximation of the spatial derivative of a function:

$$\langle \nabla \cdot f(x_i) \rangle = - \sum_{j=1}^N \frac{m_j}{\rho_j} f(x_j) \cdot \nabla W(x_i - x_j, h) \quad (\text{A10})$$

∇W is taken with respect to particle j in Equation (A10), when taken with respect to particle i , the negative sign is removed, producing:

$$\langle \nabla \cdot f(x_i) \rangle = \sum_{j=1}^N \frac{m_j}{\rho_j} f(x_j) \cdot \nabla_i W(x_i - x_j, h) \quad (\text{A11})$$

The SPH approximations in Equations (A9) and (A11) are applied to the field variables and their derivatives within the Lagrangian equations of fluid flow. This yields the continuity (A12) and momentum (A13) equations:

$$\frac{d\rho_i}{dt} = \sum_{j=1}^N \frac{m_j}{\rho_j} v_{ij} \cdot \nabla_i W_{ij} \quad (\text{A12})$$

where $W_{ij} = W(r_{ij}, h)$ and is evaluated for the distance $|r_{ij}|$. r_{ij} is the position vector from particle 'j' to particle 'i' and is equal to $r_i - r_j$.

$$\frac{dv_i}{dt} = - \sum_{j=1}^N m_j \left[\left(\frac{P_j}{\rho_j^2} + \frac{P_i}{\rho_i^2} \right) - \frac{\zeta}{\rho_i \rho_j} \frac{4\mu_i \mu_j}{(\mu_i + \mu_j)} \frac{v_{ij} r_{ij}}{r_{ij}^2 + \eta^2} \right] \nabla_i W_{ij} + g \quad (\text{A13})$$

The first term within the square brackets is pressure. The term on the right, without ξ , is artificial viscosity. This term is used to increase the stability of the numerical algorithm (Colagrossi, 2005). ξ is a proportionality factor that relates the artificial viscosity to the real SPH viscosity, and has a theoretical value of 4, but has been modified empirically to 4.96333 (Cleary, 1998). ξ has values of between 4 and 5 for most applications. P_i and μ_i are the pressure and viscosity of particle 'i', the same applies for particle 'j'. $v_{ij} = v_i - v_j$. η is a parameter used to smooth out the singularity at $r_{ij} = 0$, and g is the body force acceleration due to gravity.

The code developed by CSIRO's Mathematical and Information Sciences Division uses a compressible method for determining the fluid pressure. It is operated near the incompressible limit by selecting a speed of sound that is much larger than the velocity scale expected in the fluid flow. Equation (A14) shows the equation of state used to govern the relationship between the particle density and fluid pressure.

$$P = P_0 \left[\left(\frac{\rho}{\rho_0} \right)^\gamma - 1 \right] \quad (\text{A14})$$

Where P is the magnitude of the pressure and ρ_0 is the reference density. For water, $\gamma = 7$ is generally used (Batchelor, 1967). P_0 is the reference pressure. The pressure the equation of state is solved for (P), is then used in the SPH momentum equation governing the particle motion.

The time stepping in this code is explicit and is limited by the Courant condition modified for the presence of viscosity (Monaghan, 1992),

$$\Delta t = \min_a \left\{ 0.5h / \left(c_s + \frac{2\zeta\mu_a}{h\rho_a} \right) \right\} \quad (\text{A15})$$

where c_s is the local speed of sound.

Boundary particles are placed along solid walls. These particles are assigned physical properties, such as mass, density and velocity. These boundary particles exert a force on the fluid particles. In the work in this thesis, this force is approximated in either one of two ways. The first, and cheapest way, is a force with a Lennard-Jones form, acting in the boundary particle's normal direction (Monaghan, 1992). Interpolation of this force at each particle produces a smoothly defined repulsive boundary force, aimed at restricting the fluid's ability to penetrate the boundary. However, this approximation produces variations in the force acting on a particle moving parallel to the boundary (Monaghan, 2005). This results in disturbances in the flow close to the boundary. A single layer of boundary particles is needed to implement the Lennard-Jones boundary approximation.

The second, and more expensive way, is to construct the boundary from 3 or more layers of boundary particles and include them in the summations for the continuity equation and pressure term in the momentum equation, and evolving their densities. This is known as the gradient of kernel boundary approximation. Where this approximation is used in Chapter 4, the boundary is constructed of 5 layers of particles in order to provide an accurate representation when smoothing length is increased to 4.8 times the particle separation.

The interaction between the fluid and the structure is calculated via boundary particle acceleration, using Equation (A13). The force is then scaled according to the particle's mass (A16).

$$F_{bp(i)} = m_{bp(i)} \frac{dv_{bp(i)}}{dt} \quad (\text{A16})$$

In Equation A16, the subscript bp(i) represents boundary particle i, m is particle mass.

The sum of force experienced by each boundary particle is then scaled in Equation A17 with the mass ratio of the structure (m_{st}) and the summation of boundary particle

mass ($\sum_{bp(i)} m_{bp(i)}$).

$$F_f = \sum_{bp(i)} F_{bp(i)} \frac{m_{st}}{\sum_{bp(i)} m_{bp(i)}} \quad (\text{A17})$$

The expression for the resulting moment acting on the boundary's centre of rotation is in Equation A18, where $r_{bp(i)}$ is the distance from boundary particle i to the centre of the boundary's rotation. This moment is then scaled in Equation A19, with the mass ratio of the structure (m_{st}) and the summation of boundary particle mass ($\sum_{bp(i)} m_{bp(i)}$).

$$\sum_{bp(i)} M_{bp(i)} = \sum_{bp(i)} F_{bp(i)} r_{bp(i)} \quad (\text{A18})$$

$$M_f = \sum_{bp(i)} M_{bp(i)} \frac{m_{st}}{\sum_{bp(i)} m_{bp(i)}} \quad (\text{A19})$$

The translational and rotational motions of the object are then updated through the temporal integration of Equations A20 and A21, respectively. Here, F_s and F_d are respectively, the spring force and the damping force. A linear damping model is used throughout this work. x is the translational displacement of the object from its static equilibrium position. I_{st} is the inertia of the structure at the centre of rotation. l is the distance from the centre of rotation to either spring support position. θ is the angular displacement of the object.

$$m_{st} \frac{d^2 x}{dt^2} = \sum F_{st} = F_f + F_s x + F_d \frac{dx}{dt} \quad (\text{A20})$$

$$I_{st} \frac{d^2 \theta}{dt^2} = \sum M_{st} = M_f + F_s l \tan(\theta) + F_d l \left(\frac{d(\tan(\theta))}{dt} \right) \quad (\text{A21})$$

APPENDIX 2

RESOLUTION STUDY

The focus of this appendix, is to establish the relationship between particle size and the accuracy of numerical predictions obtained with Smoothed Particle Hydrodynamics (SPH). Efforts are made to identify a particle size that can capture all significant fluid behaviour, without increasing computational expense unnecessarily.

It is reported in Chapter 2 that some difficulty in numerically capturing local detail at the free surface is encountered in shallow depths. For this reason, the following resolution study has been undertaken at the liquid depth of 5.5 mm. This is the shallowest depth to have been successfully modelled when the container motion is imposed. The possible use of three different resolutions is investigated, those being particles with square areas of 0.0625 mm^2 , 0.25 mm^2 and 1 mm^2 . Using these particle sizes, it takes 29920, 7480 and 1870 particles, respectively, to discretize the fluid volume.

The instances analysed are chosen either as points of reference (when the structure is in the central rest position, or at maximum angular displacement), or at points in time when fluid behaviour is particularly difficult to capture numerically. For this reason, all instances shown are during the first cycle of structural oscillation, when the fluid is most energetic. The purpose of choosing these instances is to provide a complete picture of the modelling technique's capabilities, as opposed to a biased view.

Experimental snapshots are shown in Figures A2.1(a), (e), (i), (m), (q) and (u). These snapshots correspond to times of 0.95 s, 1.30 s, 1.60 s, 1.85 s, 2.75 s and 3.70 s, as indicated at the top right hand corner of the figure frames. All other figures show numerical predictions of these snapshots. Particle size used for numerical prediction is indicated at the bottom right hand corner of each frame. The corresponding time is shown at the top right hand corner. Fluid particles are coloured by velocity magnitude, the scale of which is from 0.0 to 1.2 m/s. The fixed colour scale is shown at the bottom of the figure.

Shortly after its release, the structure passes through the central rest position at $t = 0.95$ s. Around half of the container bottom is observed to be in contact with the fluid, in Figure A2.1(a). Fluid distribution is accurately predicted by all resolutions at this instant. Shortly after, fluid makes contact with the left container wall at $t = 1.30$ s. This instant is shown in Figure A2.1(e). Predicted fluid particle velocities are seen to be dependent on resolution. At high resolution (particle size of 0.0625 mm^2), fluid velocity is high at the wavefront and free surface. The fluid crosses the container bottom quickly as a result, making contact with the container wall at the same time as that observed. As resolution decreases, fluid velocity magnitudes drop, resulting in a developing phase difference in wavefront position, between predictions and the observation. For a particle size of 1 mm, a small portion of the container bottom remains exposed at this instant, shown in Figure A2.1(h).

An energetic hydraulic jump is shown in Figure A2.1(i), occurring during wave to wall interaction. All numerical predictions of this instant show more swirling behaviour than what is observed. This is expected to be due to the rounded shape of the container and three dimensional effects, not taken into consideration in the two dimensional model. The prediction of this behaviour may therefore not be unreasonable. For a particle size of 0.0625 mm^2 , significant rotational motion is predicted at the bottom left hand corner of the container. Steep velocity gradients are predicted as a result. As particle size increases, the swirling behaviour in this area becomes less defined. Velocity gradients are not as steep as a result, evident by the more gradual particle velocity colour contrasts in Figures A2.1(k) and A2.1(l). Fluid distribution is also affected by resolution at this instant. Less of the container bottom remains covered as particle size increases.

The structure achieves maximum anti-clockwise rotation at $t = 1.85 \text{ s}$. Fluid involved in the hydraulic jump has collapsed under gravity, producing the uneven free surface shown. The predicted free surface becomes smoother and less energetic with increasing particle size. Fluid distribution is again seen to be dependent on resolution, the accuracy of which reduces with increasing particle size.

The structure is shown passing through the central rest position in Figure A2.1(q). Fluid distribution is again captured well whilst the structure is in this position, at all resolutions. Shortly after, the maximum clockwise angular displacement is achieved at $t = 3.70$ s. The observed free surface at this instant is shown in Figure A2.1(u). Around three quarters of the container bottom is covered by fluid. Particle size is again seen to effect the predicted fluid distribution during a wave-to-wall interaction, the accuracy of which increases with resolution. Free surface shape is also affected, significant local detail is lost at the particle size of 1 mm^2 .

At most instances in time, fluid behaviour is captured accurately with a particle size of 1 mm^2 . However, insufficient detail is captured during energetic wave-to-wall interactions, making some fluid behaviour difficult to identify. Modelling with higher resolution provides an advantage during such interactions and when liquid depth is extremely shallow. The level of captured detail increases with resolution.

When the fluid is extremely shallow, particle size affects the fluid's ability to spread across the container surface. As a result, predicted fluid distribution and travelling wavefront positions differ from those observed at low resolution. Therefore, in terms of the accuracy of prediction, a particle size of 0.0625 mm^2 is desirable. Although this is the case, the computational expense involved with such high resolution modelling is large, and it is therefore not always feasible. Although the advantages of using a particle size of 0.0625 mm^2 over that of 0.25 mm^2 are identifiable, they are relatively small, and do not warrant the four fold increase in the computational expense. For these reasons, the particle size of 0.25 mm^2 provides an acceptable balance between the accuracy of prediction and computational expense. It is therefore used for all modelling in Chapter 2.

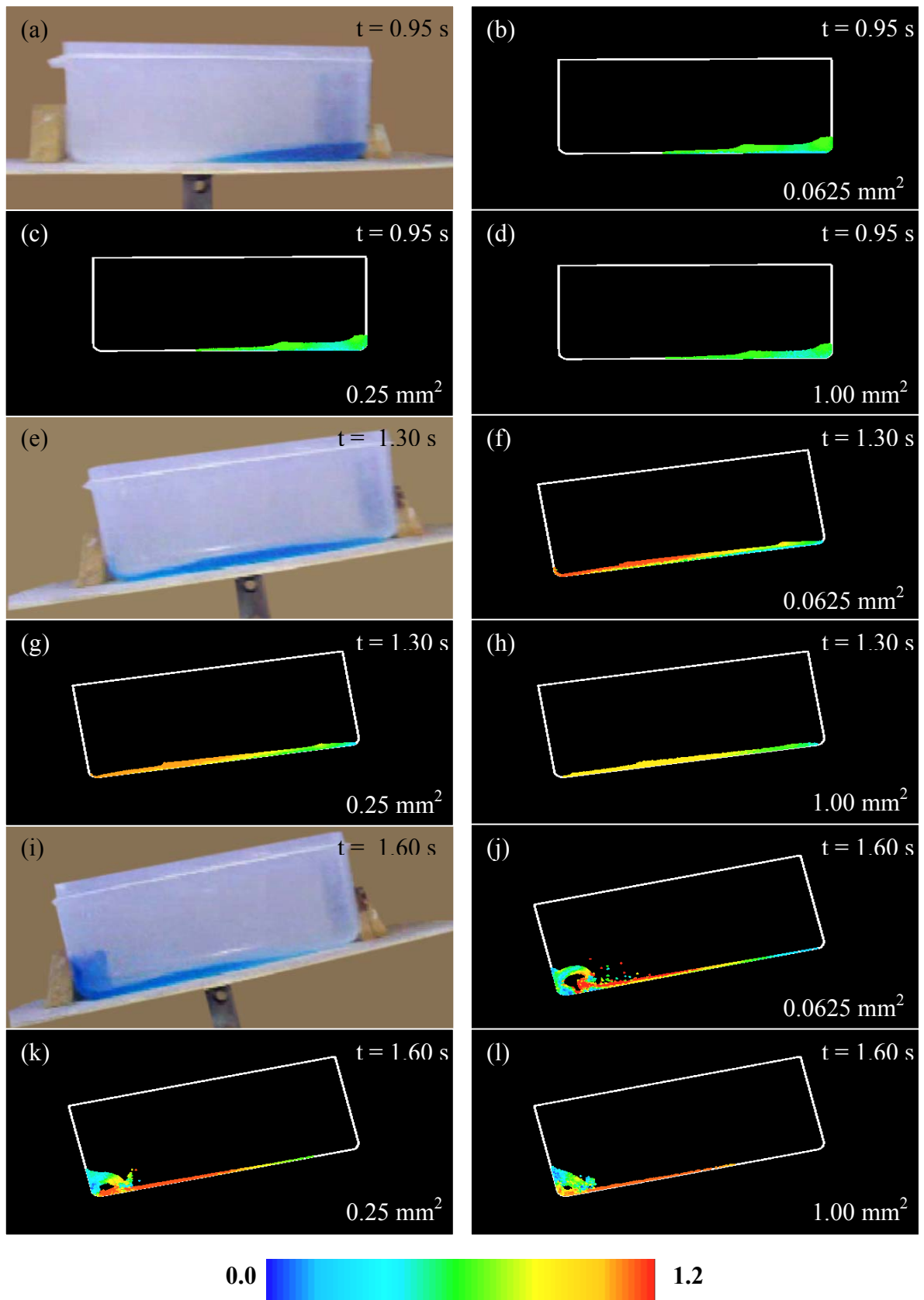


Figure A2.1. Continued over page.

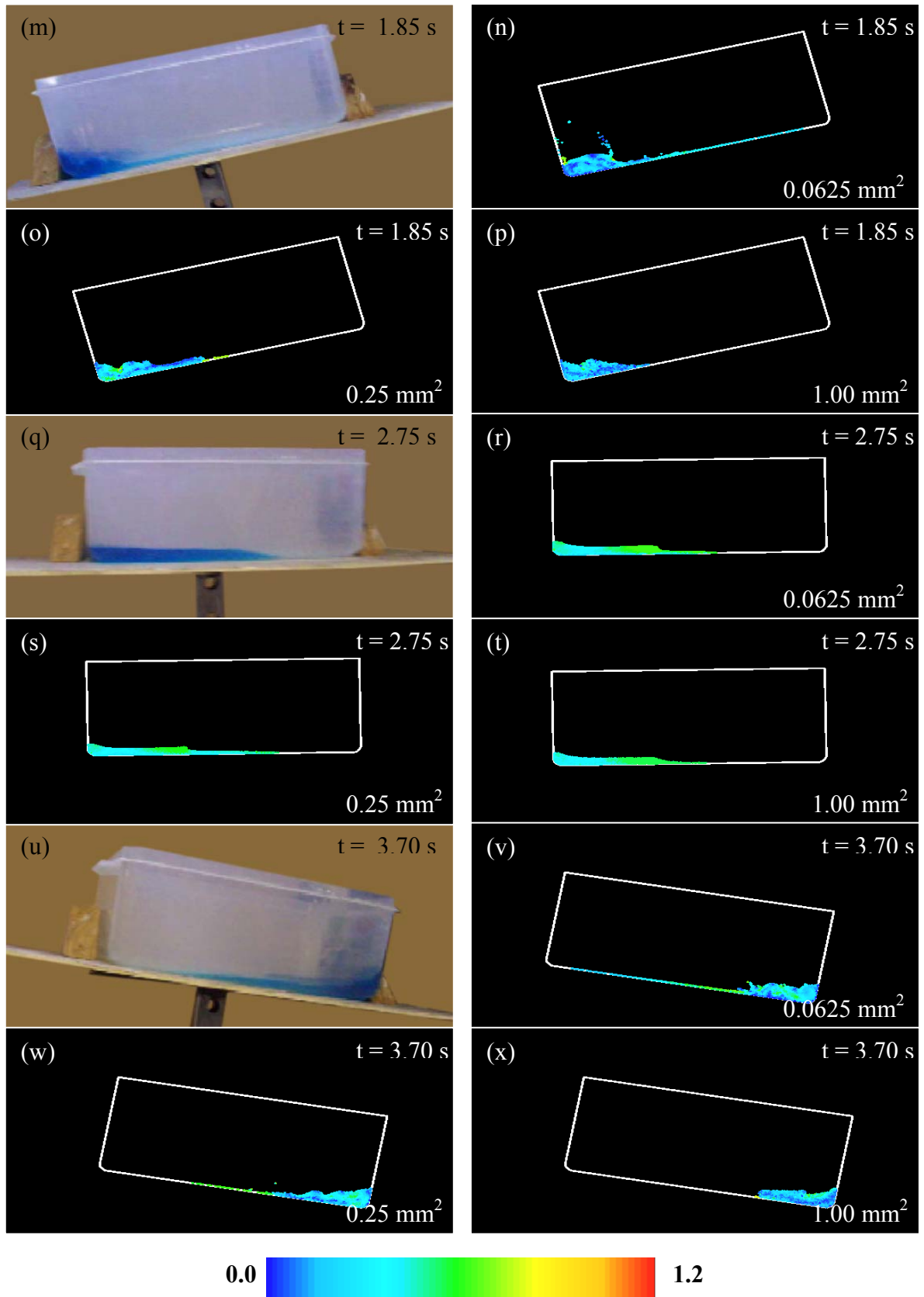


Figure A2.1. Free surface comparisons between experimental observations, and numerical predictions obtained with particle sizes of 0.0625 mm^2 , 0.25 mm^2 and 1.00 mm^2 . Particle size is marked at bottom right corner of frames. Fixed colour scale represents fluid velocity in m/s.

APPENDIX 3

KINEMATIC FREE SURFACE COMPARISONS

In Chapter 2, the fluid behaviour within a sloshing absorber, experiencing an imposed motion, is modelled with SPH. The predicted free surface shapes were compared to those seen experimentally, for liquid depths of 5.5 mm and 22 mm. Free surface comparisons at the depths of 8.25 mm and 11 mm are presented in this appendix for completeness. Such a study was undertaken to identify the effect that liquid depth has on the accuracy of prediction.

In shallow depths, some local free surface detail is not captured numerically. This is particularly evident during energetic wave-to-wall interactions. During such events, hydraulic jumps are seen, a phenomenon known for producing turbulence. Even though this is the case, fluid distribution is captured soundly at shallow liquid levels. The accuracy of prediction increases with depth. Less energetic fluid behaviour is seen due to the added fluid mass, and resulting lower structure frequency of oscillation. Hydraulic jumps are therefore less violent and captured easily with SPH. This trend is also seen for the liquid depths of 8.25 mm and 11 mm, as shown in Figures A3.1 and A3.2 respectively.

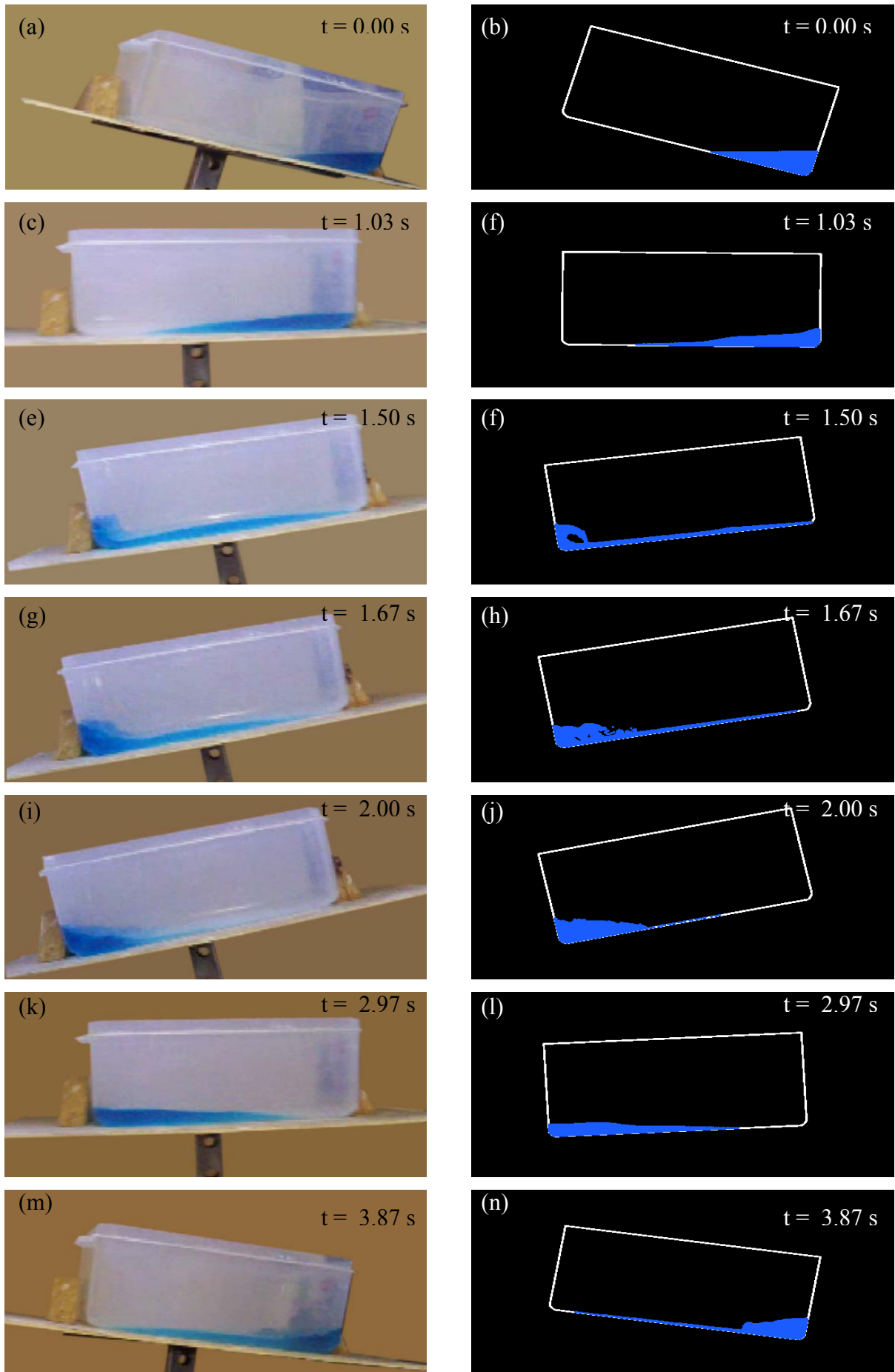


Figure A3.1. Kinematic free surface comparison for 8.25 mm depth.

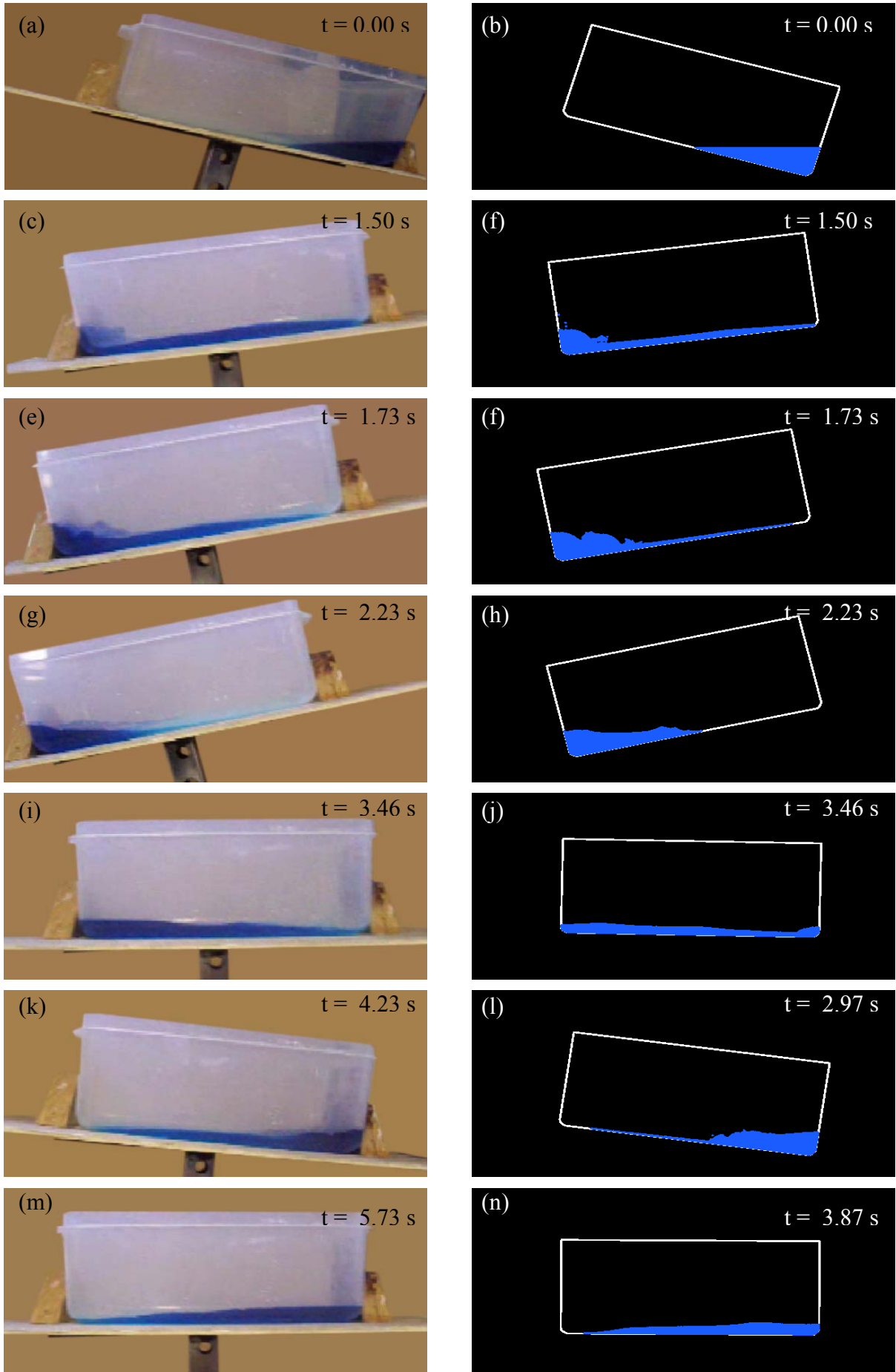


Figure A3.2. Kinematic free surface comparison for 11 mm depth.

APPENDIX 4

KINETIC ENERGY DISSIPATION HISTORIES

In Chapter 3, kinetic energy histories are presented for varying liquid depth in a 400 mm wide container. The same analysis is presented here for containers of 200 mm and 600 mm width, in Figures A4.1 and A4.2, respectively. Similar behaviour is observed in all container widths. A distinct change in energy dissipation behaviour is caused by the transition in waveform from travelling to standing. The liquid depth range at which this transition occurs increases with container width. In containers of width 200 mm, 400 mm and 600 mm, this transition occurs at the liquid depth ranges of 20 mm to 40 mm, 20 mm to 60 mm, and 20 mm to 80 mm, respectively.

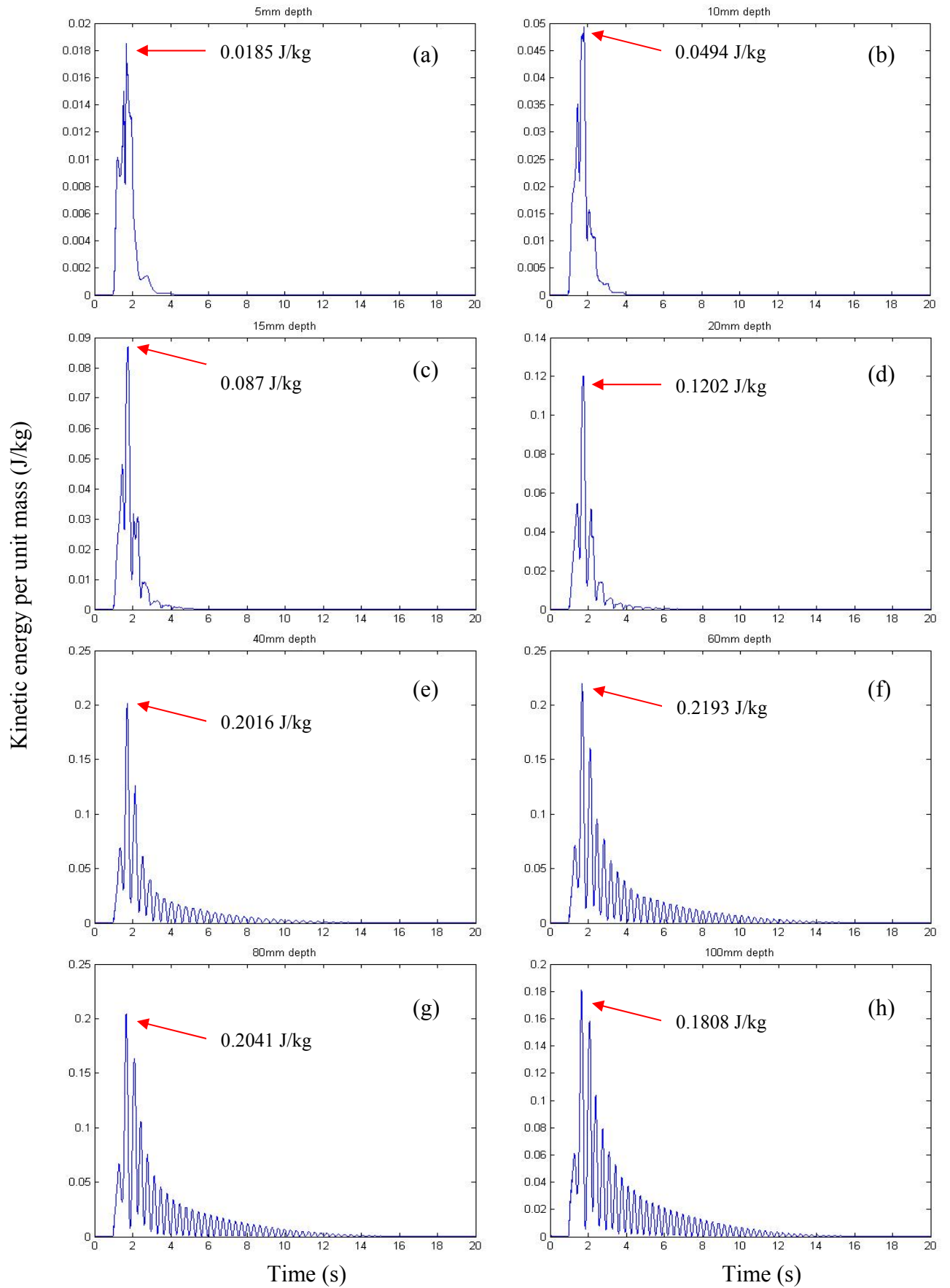


Figure A4.1 Kinetic energy dissipation histories for different water depths of (a) 5 mm, (b) 10 mm, (c) 15 mm, (d) 20 mm, (e) 40 mm, (f) 60 mm, (g) 80 mm and (h) 100 mm. Constant container width of 200 mm. The y-axis amplitude values vary significantly.

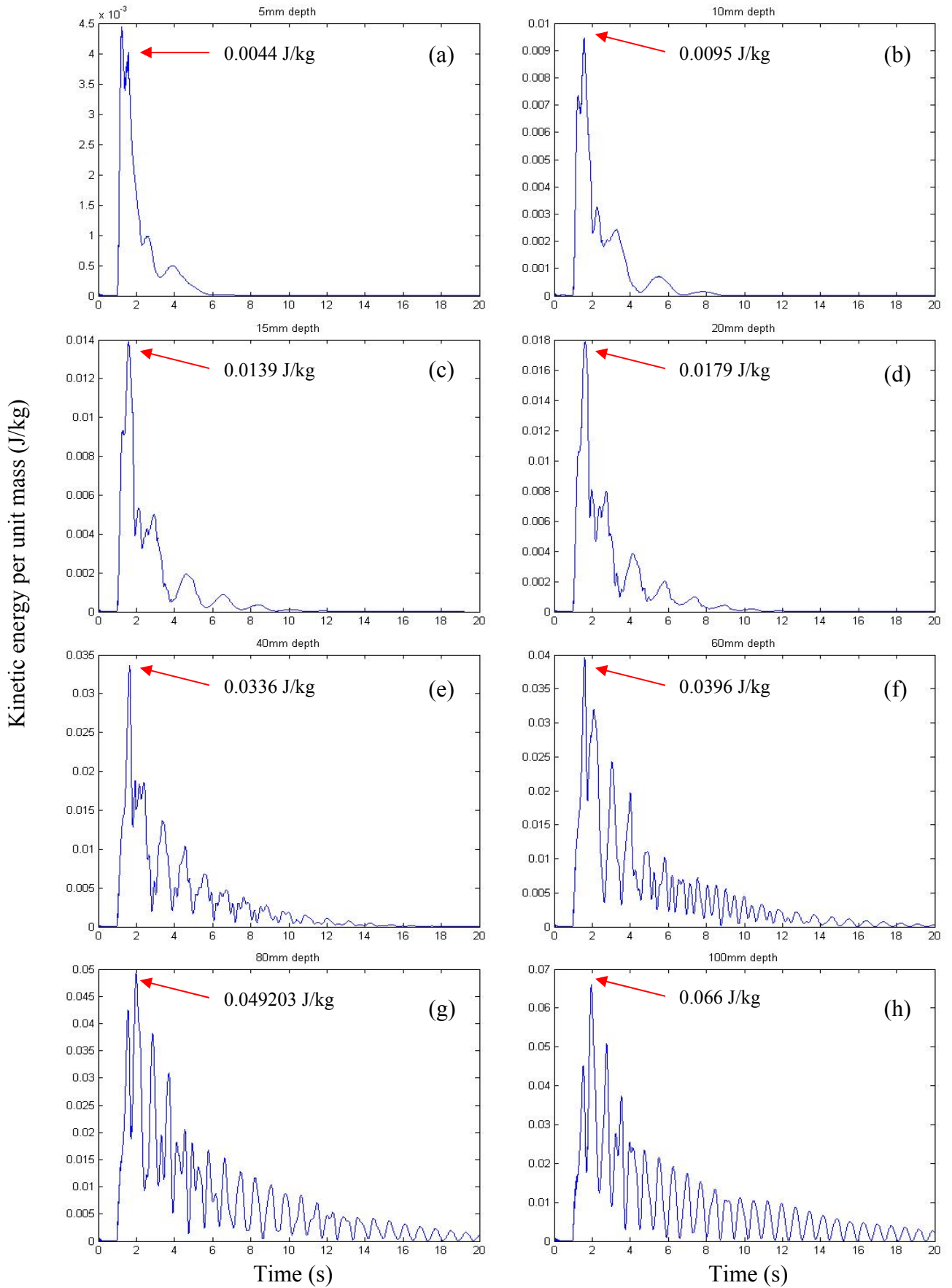


Figure A4.2 Kinetic energy dissipation histories for different water depths of (a) 5 mm, (b) 10 mm, (c) 15 mm, (d) 20 mm, (e) 40 mm, (f) 60 mm, (g) 80 mm and (h) 100 mm. Constant container width of 600 mm. The y-axis amplitude values vary significantly.

APPENDIX 5

DYNAMIC FREE SURFACE COMPARISONS

In Chapter 4, fluid-structure interaction of a structure/sloshing absorber system is modelled with Smoothed Particle Hydrodynamics (SPH). Free surface comparisons at the depth of 2.75 mm are presented. This depth is the shallowest, and therefore, the most difficult to obtain an accurate prediction of the free surface. For this reason, it is chosen as a representative case, to illustrate the ability of SPH to capture the detail of the free surface.

In this appendix, free surface comparisons for the liquid depths of 5.5 mm, 8.25 mm, 11 mm and 22 mm are presented in Figures A5.1, A5.2, A5.3 and A5.4 respectively. These comparisons are presented here for the sake of completeness, and they are not included in the main text due to providing little additional understanding for the reader. As stated in Chapter 4, the accuracy of the free surface improves with liquid depth. However, the excessive energy dissipation within the fluid makes providing a fair free surface comparison difficult. This is due to the developing phase difference between observed and predicted structure position, for liquid depths of and above 8.25 mm.

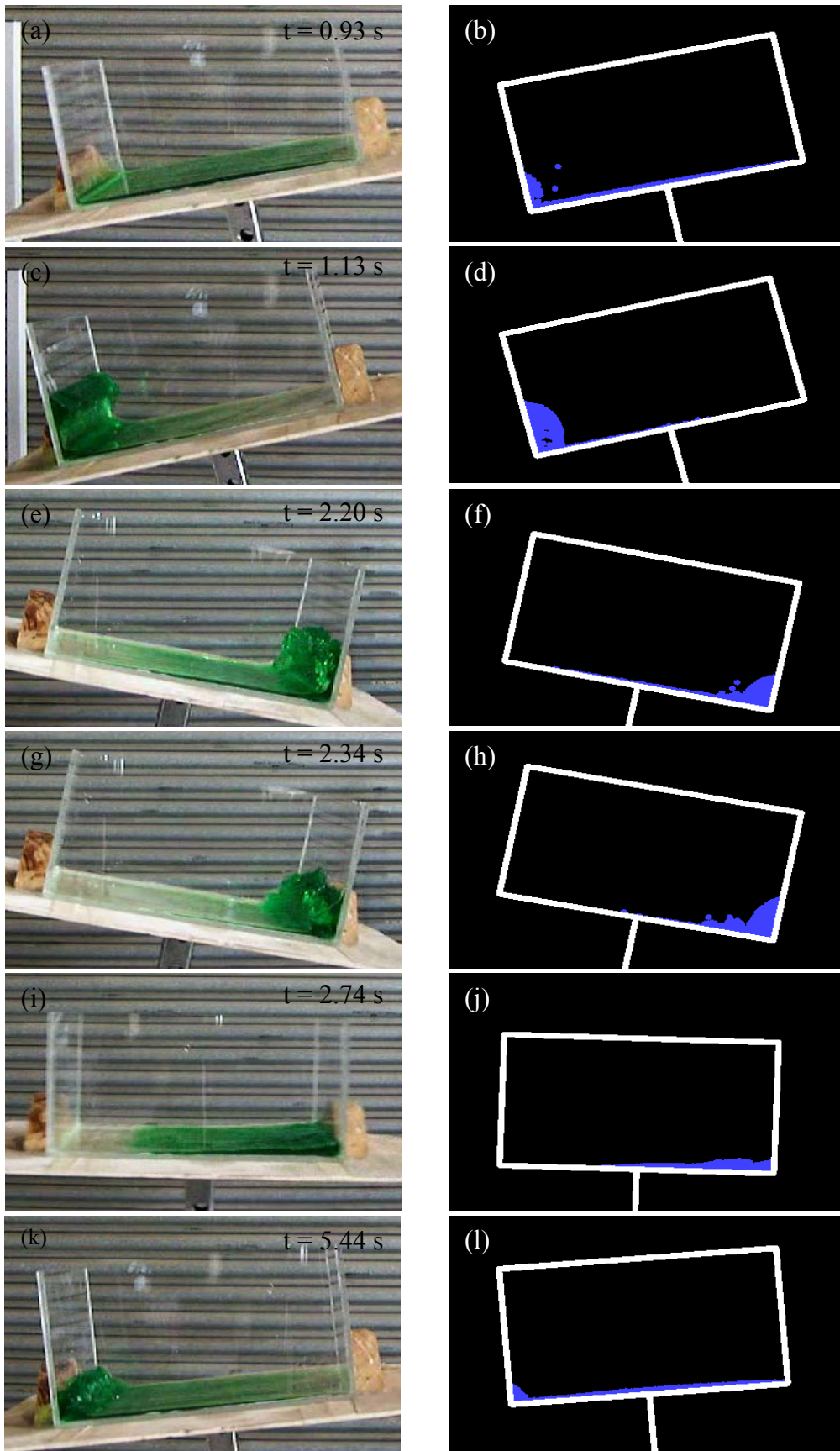


Figure A5.1. Dynamic free surface comparison for 5.5 mm liquid depth.

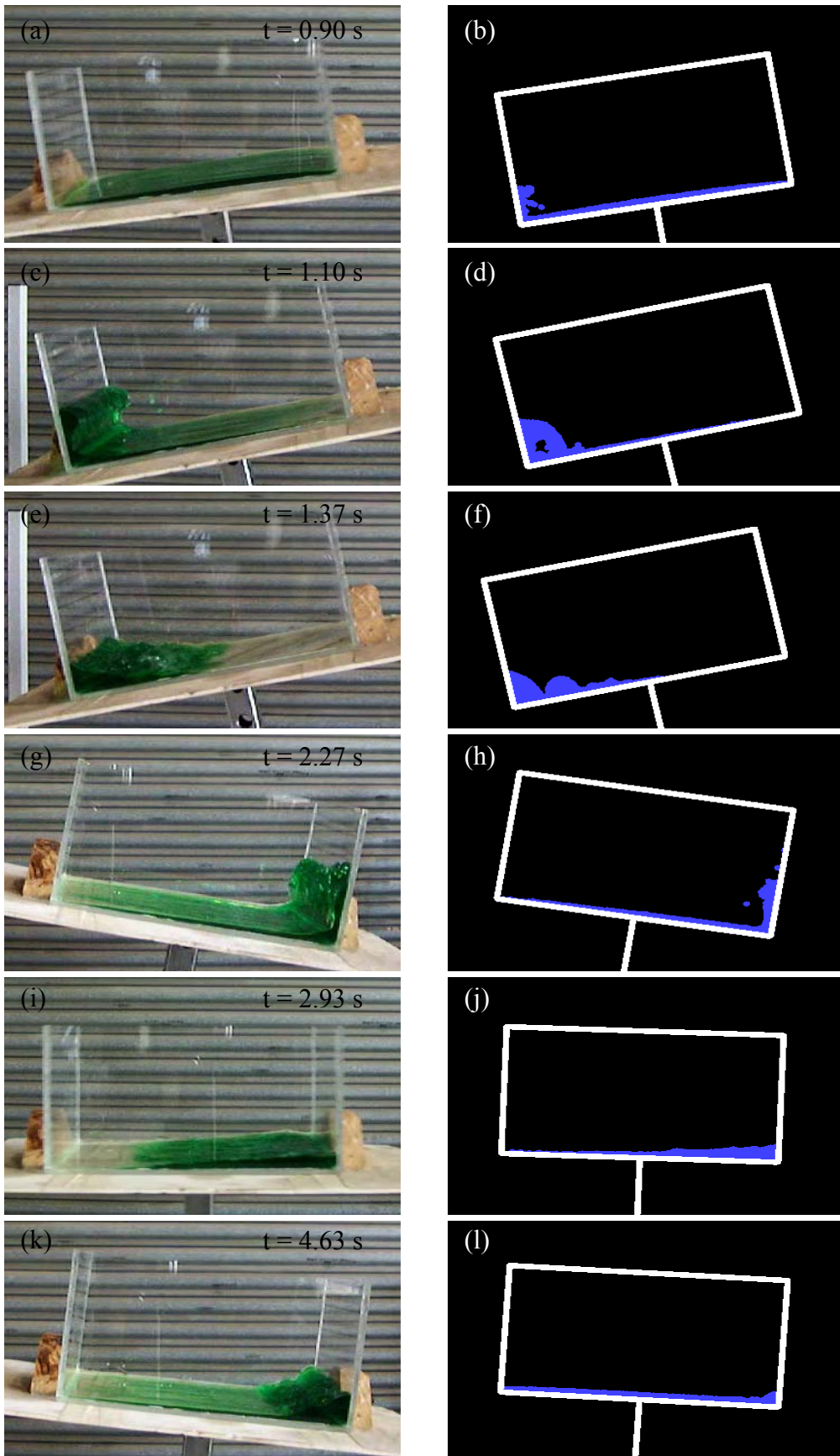


Figure A5.2. Dynamic free surface comparison for 8.25 mm liquid depth.

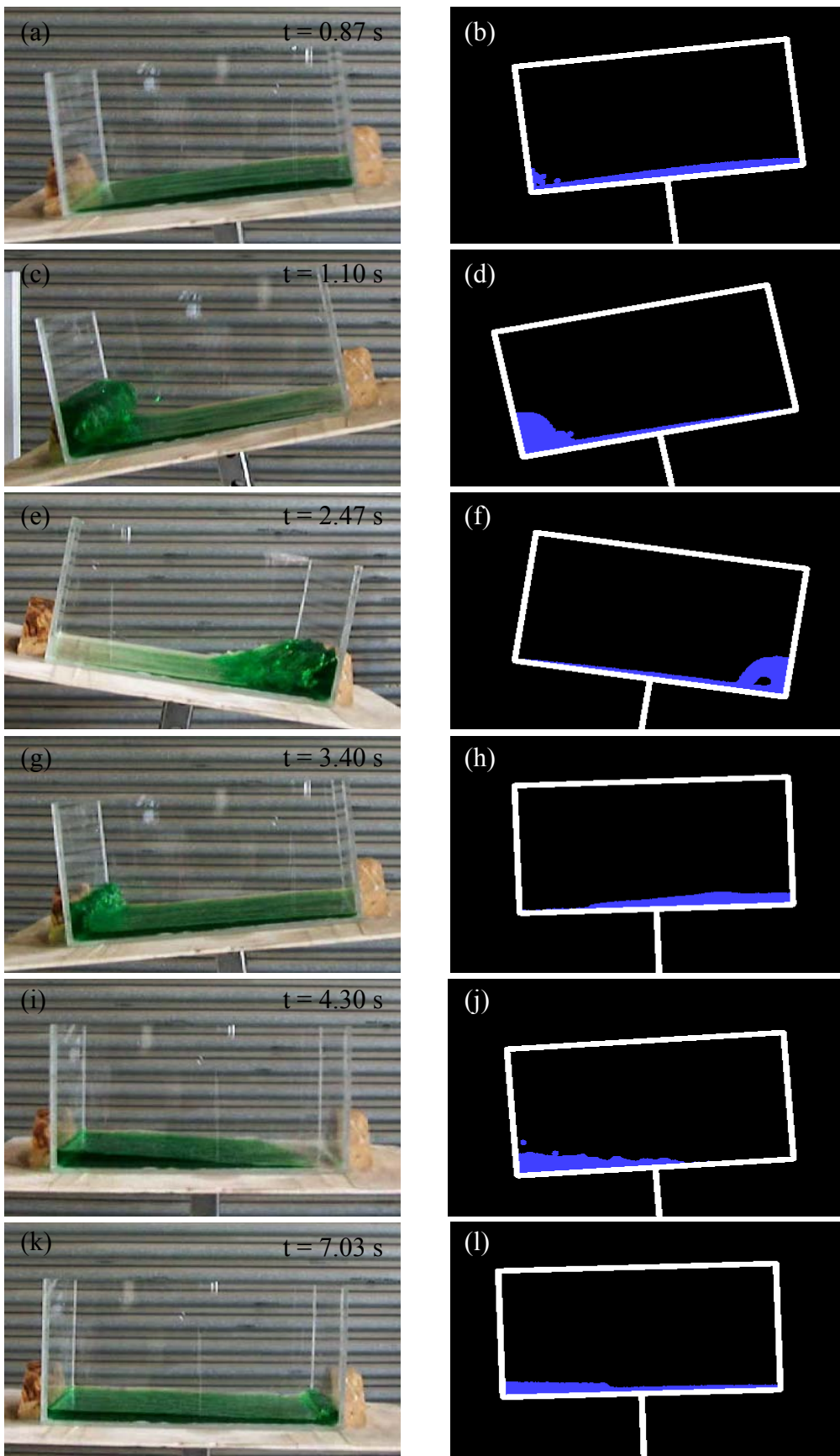


Figure A5.3. Dynamic free surface comparison for 11 mm liquid depth.

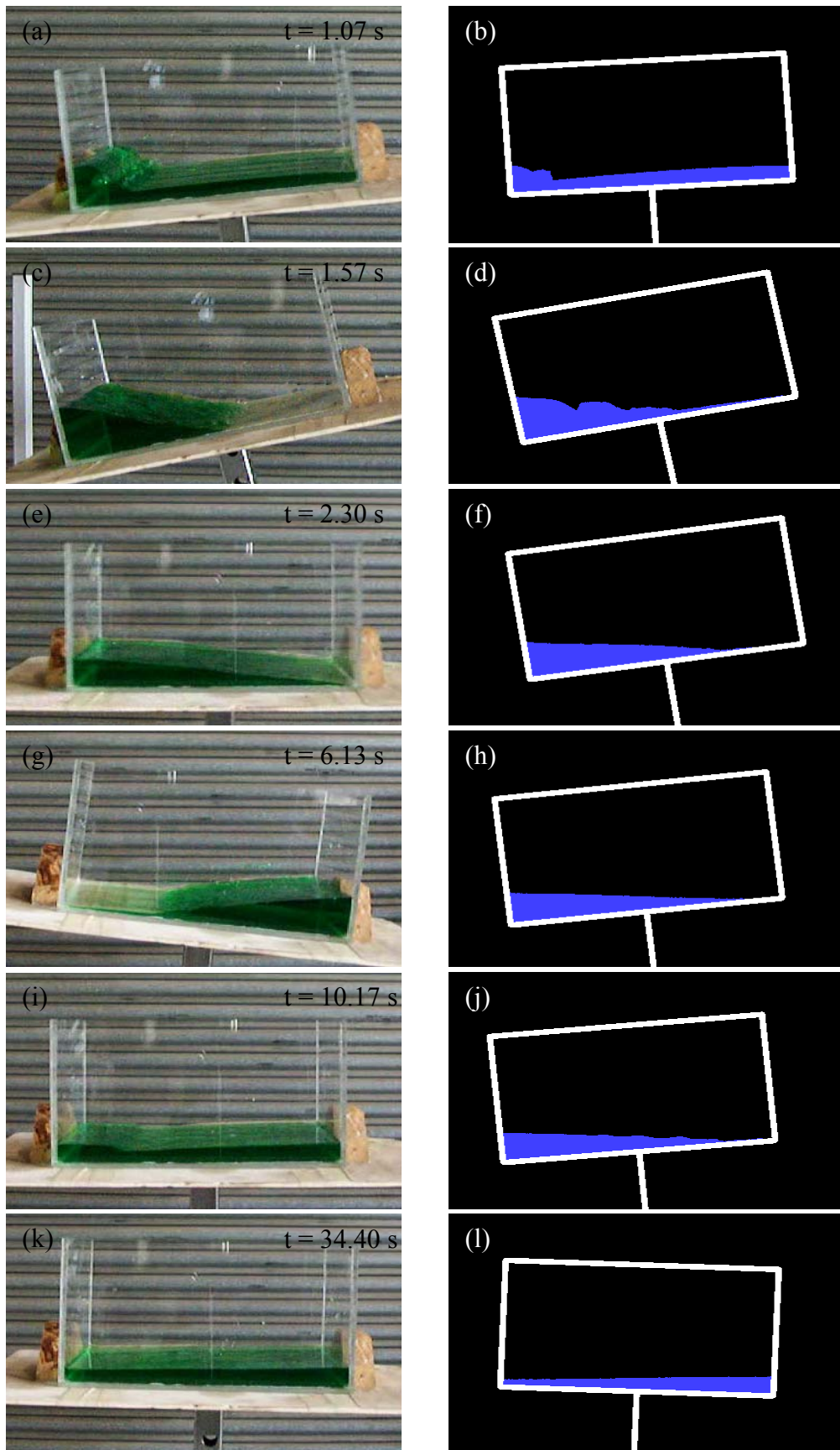


Figure A5.4. Dynamic free surface comparison for 22 mm liquid depth.

APPENDIX 6

OSCILLATORY HISTORIES OF MODIFIED EGG PROFILE

In this appendix, oscillatory histories of the structurally modified egg-shell are presented, to accompany the work in Chapter 5. This modification is introduced in the form of a fin, protruding from the bottom of the egg and extending along its axis of symmetry. The egg-shell has a fin introduced, of height 0.2, 0.4 and 0.6 times the length of the long axis of the egg, in Figures A6.1, A6.2, and A6.3, respectively. In these figures, (a) is a graphical representation of the egg-shell profile. Oscillatory histories of the egg-shell when filled to the volume fractions of 0.2, 0.4, 0.6, 0.8 and 1.0, are shown in (b), (c), (d), (e) and (f), respectively.

For all fin lengths, control performance is seen to be largely dependent on volume fraction. This is a trend not seen in the unmodified egg-shell profile. The fin disturbs the natural flow behaviour, disrupting energy dissipation patterns. In the natural egg-shell with large volume fractions, energy is dissipated at the boundary due to shear stress produced by the rotational nature of the flow. The fin disrupts the rotation, dramatically reducing the shear stress. The amount of flow disruption increases with fin length. This results in the egg-shell experiencing more oscillations and taking a longer period of time to come to rest.

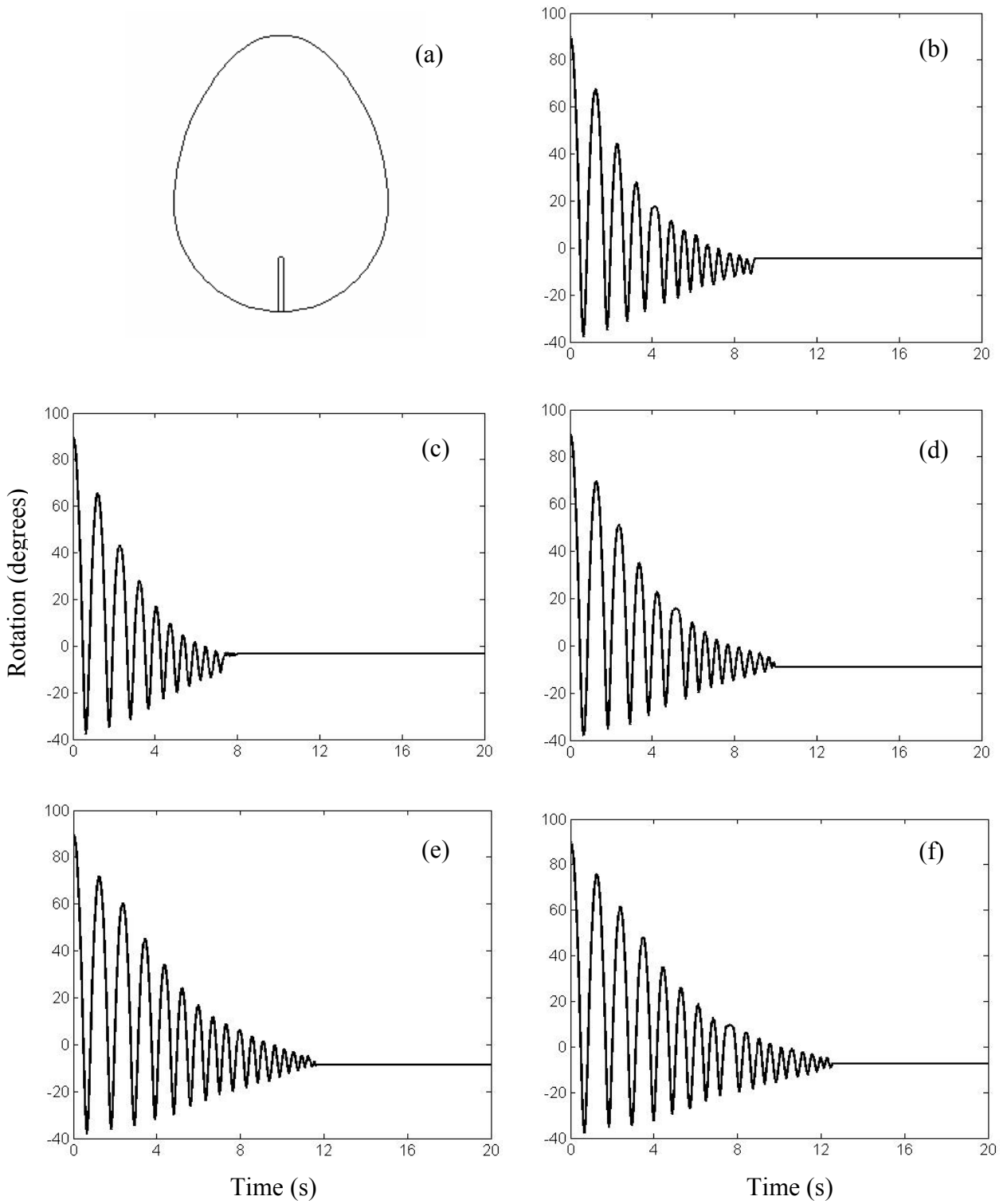


Figure A6.1. Showing (a) the schematic of the fin height ratio of 0.2, and displacement histories with a volume fraction of (b) 0.2, (c) 0.4, (d) 0.6, (e) 0.8 and (f) 1.0.

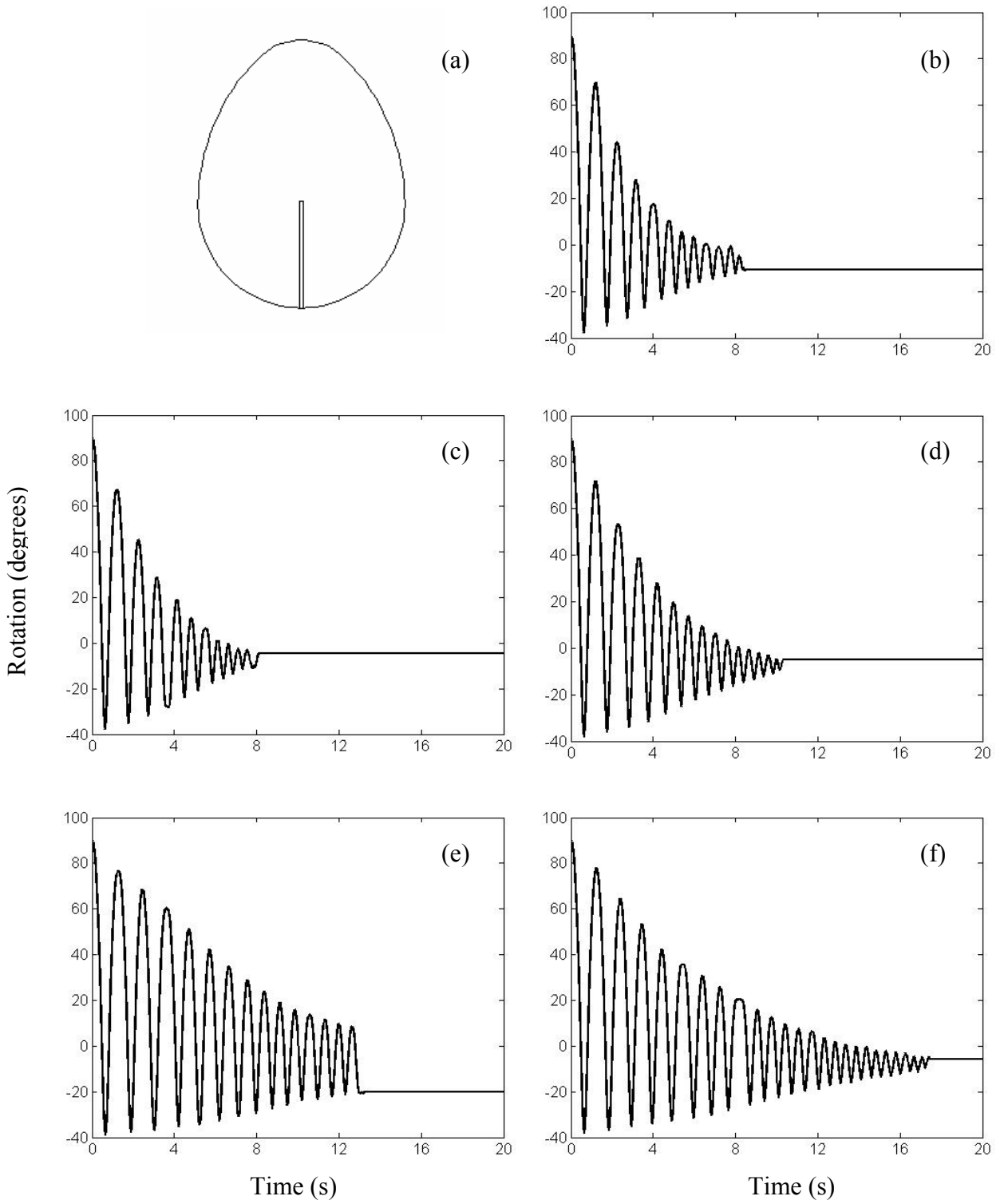


Figure A6.2. Same as in Figure A6.1., but with a fin height ratio of 0.4.

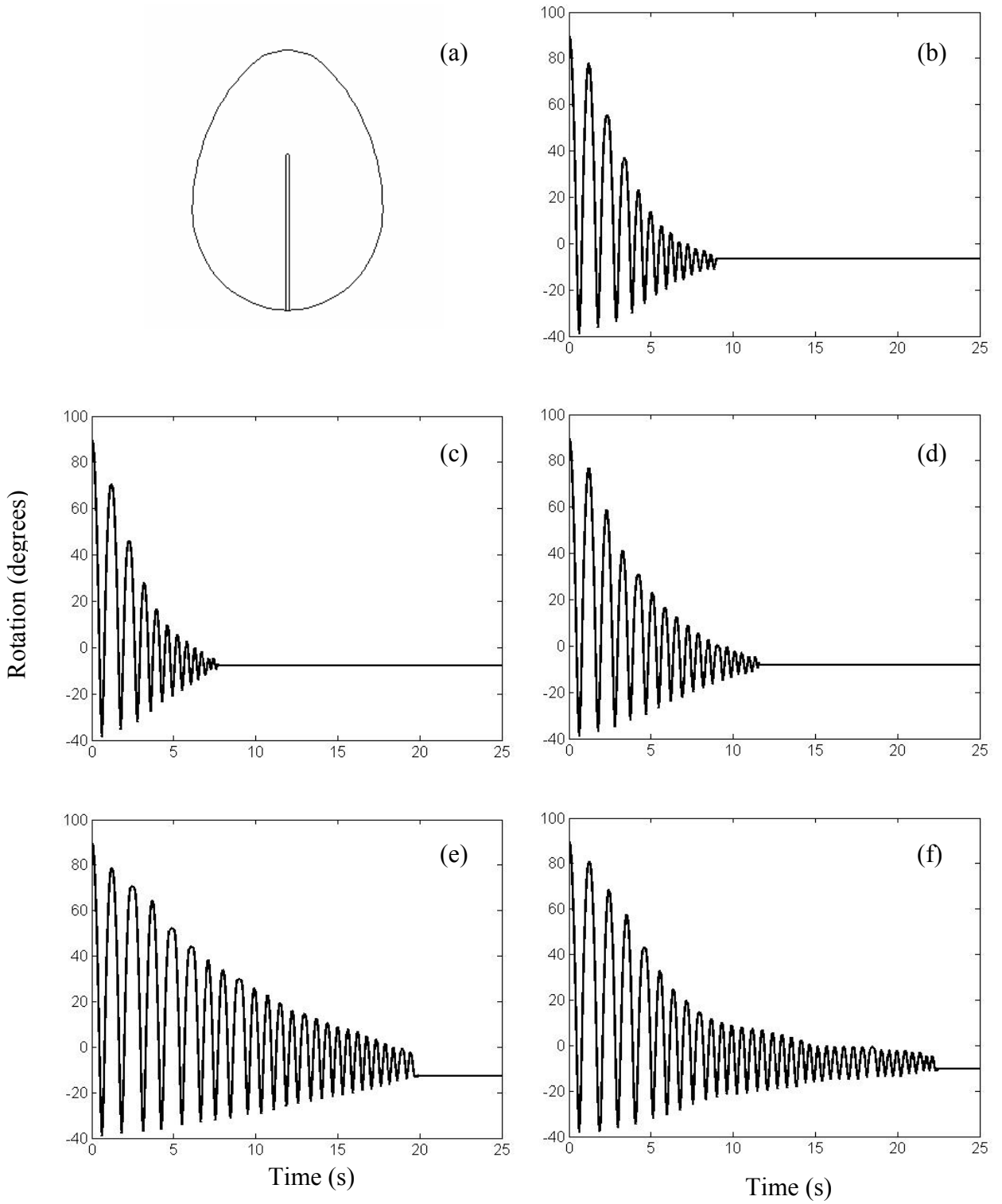


Figure A6.3. Same as in Figure A6.1, but with a fin height ratio of 0.6.